Photon and π^0 Production in ^{197}Au+^{197}Au Collisions at $\sqrt{s_{\mathrm{NN}}} = 130$ GeV

Ian J. Johnson
Nuclear Science Division

September 2002
Ph.D. Thesis

Photon and π^0 Production in ^{197}Au+^{197}Au Collisions at $\sqrt{s_{\rm NN}} = 130$ GeV

Ian Jeffrey Johnson

Ph.D. Dissertation

Department of Physics
University of California, Davis
Davis, CA 95616

and

Nuclear Science Division
Lawrence Berkeley National Laboratory
University of California
Berkeley, CA 94720

September 2002

Photon and π^0 Production in ^{197}Au+^{197}Au Collisions at $\sqrt{s_{\rm NN}} = 130$ GeV

Abstract

Inclusive transverse momentum spectra of photons and π^0s at mid–rapidity are studied as a function of collision centrality for ^{197}Au+^{197}Au collisions at $\sqrt{s_{\rm NN}} = 130$ GeV. Photon pair conversions have been reconstructed from charged tracks measured by the main Time Projection Chamber of the STAR experiment at the RHIC heavy ion facility. The transverse momentum resolution of photons with this method is estimated to be $\Delta p_t/p_t = 2\%$ at 0.125 GeV/c and 5% at 2.5 GeV/c. Photon spectra were measured up to a transverse momentum of 2.4 GeV/c between ± 0.5 units of rapidity. The dominant photon production mechanism, the $\pi^0 \rightarrow \gamma\gamma$ decay, was measured between 0.25–2.5 GeV/c and ± 1 units of rapidity. Spectra are reported for the top 11%, 11–34% and 34–85% centrality classes. It was observed that in mid–central and central collisions the relative contribution of the $\pi^0 \rightarrow \gamma\gamma$ decay to the inclusive photon spectrum decreases above a transverse momentum of 1.65 GeV/c. In central collisions the magnitude of the decrease from $p_t = 1.65$ GeV/c to 2.4 GeV/c is 20%. It is unlikely that contributions from other π^0 decay channels and other particle decays fully explain this decrease. The centrality dependence on the shapes of the π^0 spectra was analyzed with Boltzmann and Bose–Einstein functions. In the transverse momentum windows of the spectra, the extracted temperatures are near 0.295 GeV. These temperatures are substantially higher than those extracted from $\pi^{\pm}$ spectra in a lower range of transverse momentum. This is an indication that the shapes of the pion spectra deviate from purely exponential shapes.

Contents

List of Figures

List of Tables

Acknowledgments

The work presented in this dissertation is a reflection of the combined efforts of many people. I would like to thank my collaborators, STAR, for making the experimental environment stimulating and enjoyable. Among these people, I would like to recognize the brilliant engineers and scientists for designing and assembling such a remarkable TPC. In addition, the staff at the National Energy Research Computing facility, especially Dr. Iwona Sakrejda and Dr. Eric Hjort, has my appreciation for creating and maintaining such a stable computing environment that was easy to work within. I thank the members of the Relativistic Nuclear Collisions group at Lawrence Berkeley National Laboratory for creating a stimulating research environment. I have also enjoyed working with Nuclear Group at the University of California at Davis. I am grateful for the financial support that both of these groups have provided.

At a more personal level, I would like to thank Dr. Kai Schweda, Dr. James Symons, Prof. Daniel Cebra, and Dr. Eugene Yamamoto for giving me the privilege to work with them. Along with endless hours of discussion and impelling motivation; Kai has not only been an educator but also a good friend. I thank Dr. James Symons for providing me with his ideas and advice throughout this degree. I thank Prof. Daniel Cebra for his support and encouragement. It is also nice to have a friend like Geno, whom knows both physics and how to enjoy life. I thank them all for carefully reading and revising this dissertation.

Throughout the challenges that I encountered during this education, I thank all my friends for the good times, laughs, and inspiration that helped me stay happy and positive. I am especially grateful for the support that my loving family has provided.

Chapter 1

Introduction

1.1 Overview

One goal of nuclear physics is to study the properties of matter under extreme conditions, such as those that nature has the power to produce. Microseconds after the Big–Bang, before the formation of nucleons, temperatures are believed to have reached $\sim 2\times10^{12}$ K. And presently at the center of neutron stars densities far beyond that of normal matter exist. Studying the former is difficult, since it no longer exists, while astronomical distances complicate the investigation of the latter. Here on earth, experimental efforts are directed towards creating and studying similar systems in the laboratory. The only known opportunity for producing such extreme systems is with relativistic nucleus–nucleus collisions. Investigating the properties of matter under these extreme conditions is of special interest, because theoretical models and calculations have predicted that an undiscovered state of matter exists.

The fundamental theory of strongly interacting matter, Quantum Chromodynamics (QCD), describes partonic interactions through the exchange of gluons. In this theory, a strong coupling constant, $\alpha_s(q^2)$ where q is the transferred momentum, confines color charged objects –quarks and gluons– to colorless hadrons in quark pairs (mesons), quark triplets (baryons), or possibly pure gluonic configurations (glueballs). At large momentum transfers (or short distances), α_s decreases logarithmically and the binding between quarks becomes weak. At some point, quarks and gluons behave like unbound particles (the limit of asymptotic freedom). In a many body system, the color screening from interactions with neighboring gluons would allow quarks and gluons to freely roam within a large globally color neutral system, not isolating them to specific hadrons. Lattice QCD supports this hypothesis and predicts a phase transition, from hadronic matter into a state of deconfined quarks and gluons, in environments of extreme temperatures ($\sim$172 MeV or 2×10^{12} K Lattice QCD [Kar02]), energy densities (>1 GeV/fm^3), and/or baryon densities (a few times that of normal matter).

At facilities, like the Relativistic Heavy Ion Collider (RHIC) at Brookhaven National Laboratory, enormous energy densities (>1 GeV/fm^3) are created when nuclei, traveling at relativistic velocities (v $\approx 0.9999c$), pass through each other and partons within the opposing nuclei interact. These interactions may possibly produce a system of the theoretically proposed state of deconfined quarks and gluons. As this system expands, the temperature and density will drop below critical values and hadronization will occur. Under the assumption of a first order phase transition, a mixed phase might exist where hadrons would sporadically emerge and co–exist with unbound partons. Ultimately, the system condenses into a gas of interacting hadrons. As the hadronic system expands and

dilutes, *inelastic* interactions become more and more scarce. At the point these *inelastic* interactions stop, the system reaches chemical freeze–out. Finally, *elastic* interactions cease and the momentum distribution of particles are frozen at thermal freeze–out.

1.2 Probing Heavy Ion Collisions with Photons

For more than 20 years, photons have been considered one of the most valuable probes of the dynamics and properties of the matter formed in heavy ion collisions [Shu78, A$^+$00, PT02]. In contrast to hadronic particles that have large interaction cross sections in dense matter, photons interact only electromagnetically and have a long mean free path. This path length is typically much larger than the transverse size of the hot dense matter created in nuclear collisions [KLS91]. Therefore, with high probability, photons will escape from the system undisturbed and preserve the history of their birth. Photons that radiate from and escape a deconfined system will provide information about the conditions under which they were created. However, separating these photons from other more copious production mechanisms currently poses as an experimental challenge.

Photons are produced in all stages of heavy ion collisions, from the instant quarks and gluons of the opposing nuclei interact through to hadron decays. Photons emitted in the initial hard partonic scattering are called "prompt photons". In the quark model, production mechanisms include quark–antiquark annihilation $q\bar{q}\rightarrow g\gamma$ or $q\bar{q} \rightarrow \gamma\gamma$, quark–gluon Compton scattering $qg\rightarrow q\gamma$ or $\bar{q}g \rightarrow \bar{q}\gamma$, and electromagnetic bremsstrahlung $q\rightarrow q\gamma$ or $\bar{q} \rightarrow \bar{q}\gamma$ [SG98, KW99]. In a deconfined state, photons are radiated from the same partonic interactions that are accountable for the prompt photons [Shu78]. After the system cools into a hadronic gas, photons will be produced in hadron–hadron scatterings [KLS91]. Among the main hadronic processes are the Compton process $\pi\rho \rightarrow \pi\gamma$, annihilation $\pi\pi \rightarrow \rho\gamma$, and the production and decay of the a_1 axial vector meson resonance $\pi\rho \rightarrow a_1 \rightarrow \pi\gamma$ [XSB92]. Finally, after all interactions have stopped, long–lived electromagnetic decays continue to create photons. The most abundant photon contributors of these decays include: the $\pi^0 \rightarrow \gamma\gamma$, $\pi^0 \rightarrow e^+e^-\gamma$, $\eta \rightarrow \gamma\gamma$, $\eta \rightarrow e^+e^-\gamma$, $\omega \rightarrow \pi^0\gamma$, $\eta' \rightarrow \rho\gamma$, $\Sigma^0 \rightarrow \Lambda\gamma$.

Extensive theoretical efforts have calculated photon production rates based on a variety of initial conditions and scenarios. It has been demonstrated that the emission rates of the hadron gas state are comparable to those expected to arise from quark–gluon Compton and annihilation processes in a deconfined state [KLS91]. However, it should be noted that a net baryon free deconfined system was assumed in these calculations. Even at RHIC energies, measurements have demonstrated that the systems created are not baryon free at mid–rapidity [A$^+$01d, B$^+$01a, I$^+$01]. Furthermore, recent calculations reveal that two–loop calculations, which include the bremsstrahlung process, exceed rates computed with former one–loop calculations of the Compton and annihilation processes [AGZ98, Sri99]. These more recent calculations indicate "that the emissions from quark matter can outshine those from the hadronic matter" [Sri99].

Prompt photons created via the bremsstrahlung mechanism are also of special interest, because they are emitted as the fractionally charged quarks in the colliding nuclei decelerate. These photons not only reveal the amount of deceleration, but also the finer details of the space time evolution of the charges [KW99, SG98]. Theoretical calculations have shown that this mechanism will be the dominant mechanism of early photon production and create a flash of prompt photons [SG98].

Of all the production mechanisms, the late electromagnetic decays are the dominant sources of photons. At CERN SPS energies (see Table 2.1), photons from π^0 and η decays composed $\sim$97% of the inclusive photon spectrum [A$^+$00]. Their abundances were measured and their contributions to the single photon spectrum were calculated, as discussed in [A$^+$00, A$^+$01f]. Thermal models that describe hadron production must be used to estimate the particle yields of the other less significant decays (ω, η', Σ^0), since their production rates have not yet been measured in heavy ion collisions.

With the photon reconstruction technique described later in this thesis, measurements of the $\eta' \rightarrow \rho\gamma$ and $\Sigma^0 \rightarrow \Lambda\gamma$ are quite promising. With estimated or measured yields, the contribution to the single photon spectrum from these decays can be calculated. Thus, most of this enormous background in the single photon spectrum from electromagnetic decays can be determined.

1.3 Experimental Measurements

Measurements of prompt photons from p–p, p–$\bar{p}$ and p–nucleus collisions have experimentally justified the accuracy of QCD calculations at high transverse momentum (p_t>3 GeV/c) [VW97]. Experimentally, it has been an ongoing challenge to extract direct photons in heavy ion collisions. The most recent measurements of photons in heavy ion collisions were made by WA98. Their results illustrate the p_t dependence on the fraction of measured photons to background photons from π^0 and η decays for both peripheral and central event samples [A$^+$00, A$^+$01f]. This publication also provides the first measurement of direct photons in heavy ion collisions. The paper concludes with one of the most spectacular experimental observations in heavy ion physics: "The comparison suggests excess direct photon production in central ^{208}Pb+^{208}Pb collisions beyond that expected from proton–induced reactions" [A$^+$00]. This thesis provides the first measurements of photon spectra in heavy ion collisions at RHIC energies.

In this thesis, inclusive spectra of photons and π^0s in ^{197}Au+^{197}Au collisions at $\sqrt{s_{\rm NN}} = 130$ GeV are presented and discussed. These measurements are used to estimate the $\pi^0 \rightarrow \gamma\gamma$ contribution in the single photon spectrum. The remainder of this thesis is organized as follows: In Chapter 2, the heavy ion facility at Brookhaven National Laboratory and the experimental setup of the STAR detector system are described. Chapter 3 starts with the development and technical details of the method used to detect photons via pair conversion, $\gamma Z \rightarrow e^- e^+ Z$, and ends with the inclusive spectra of photons and π^0s measured through the $\pi^0 \rightarrow \gamma\gamma$ decay channel. In Chapter 4, the resolution of kinematic parameters and efficiency corrections are presented. In Chapter 5, the spectra and the relative contribution of the $\pi^0 \rightarrow \gamma\gamma$ decay in the single photon spectra are discussed. A conclusion and outlook are given in Chapter 6.

Chapter 2

Experimental Apparatus

The results presented in this thesis were obtained from data collected by the STAR experiment during the year 2000, the first year of running at the Relativistic Heavy Ion Collider (RHIC). RHIC is a new accelerator facility at the Brookhaven National Laboratory (BNL) which produces head on collisions of nuclei at very high energies, and STAR is one of four complementary detectors that have been built to measure the particles emitted from these collisions.

The four current heavy ion experiments at RHIC are named BRAHMS, PHOBOS, PHENIX and STAR. Each of these experiments is optimized to measure a different aspect of the final state particle spectrum, but there are also overlaps in their capabilities so that consistency checks can be made between them. STAR's particular advantage is that it has a complete 2π azimuthal acceptance for charged particles close to mid–rapidity.

2.1 The Heavy Ion Facility at BNL

With the addition of RHIC, the center of mass energy available in nuclear collisions at the heavy ion facility at BNL exceeds that of all previous heavy ion facilities by an order of magnitude. RHIC has surpassed earlier facilities by providing ^{197}Au+^{197}Au collisions at $\sqrt{s_{\rm NN}} = 200$ GeV. With the exception of a very limited program at the CERN ISR, all previous heavy ion experiments used a design where one beam was incident on a fixed target. The total energy for fixed target experiments is penalized by the Lorentz transformation required to boost from the laboratory to the center of momentum frame. At ultra–relativistic beam energies, the fixed target center of momentum energy can be approximated as $\sqrt{2M_{beam}E_{beam}}$, or the square root of the energy available in two colliding beams of the same energy. A comparison of typical heavy ion facilities is given in Table 2.1.

The Heavy ion facility at BNL uses a combination of transfer, storage and accelerating systems to supply the RHIC rings with beams for the final stage of acceleration. The complete path that the ions travel is shown in Figure 2.1. Negative ^{197}Au ions stream from a Pulsed Sputter Ion Source into a Tandem Van de Graaff accelerator. In this accelerator, the negative ions are attracted by a large positive potential, $\sim$15 MV. At the center, they encounter a foil that strips electrons from the 15 MeV negative ions. ^{197}Au^{+14} ions are then selected from the residual spectrum of ions and repelled by the positive potential. The resulting ions have a total kinetic energy of 225 MeV. These ions are transferred to the Booster synchrotron via the Heavy Ion Transfer Line and the Heavy Ion Bypass Line. The Booster ring is filled with three bunches of about 10^9 particles in each. The bunches are accelerated using radio frequency synchrotron acceleration to a energy of 72 MeV per nucleon. The filling of the Booster ring and subsequent acceleration takes about 1.2 s. From here the

Year	Facility	Laboratory	Species	E_{beam}	E_{CM}	Total E_{CM}
1974 – 1991	BEVALAC	LBNL	^{197}Au+^{197}Au	2 GeV	2 GeV	0.4 TeV
1994 – present	AGS	BNL	^{197}Au+^{197}Au	11 GeV	5 GeV	0.9 TeV
1994 – present	SPS	CERN	^{208}Pb+^{208}Pb	158 GeV	17 GeV	3.6 TeV
2000 – present	RHIC	BNL	^{197}Au+^{197}Au	100 GeV	200 GeV	39.4 TeV

Table 2.1: Some beam species and collision energies for various heavy ion accelerators. The facilities are given by a facility acronym and location. Beam energies correspond to the top per nucleon beam energy achievable by the facility. The E_{CM} and Total E_{CM} columns give the per nucleon and total energy of the system in the center of momentum frame, respectively.

ions are injected into the Alternate Gradient Synchrotron (AGS). The AGS accelerates the beam to 10.8 GeV per nucleon. Ions in the beam are fully stripped of their electrons in the transfer line from the AGS to the RHIC rings. In about two minutes, both RHIC rings are loaded with 57 bunches in boxcar fashion, each bunch containing $\sim 10^9$ ^{197}Au^{+79} ions. The final acceleration is performed in the two independent opposing acceleration rings. The two rings are commonly known as the yellow and blue ring. These rings are 3.8 km in circumference or ∼610 m in radius. Once the collision energy is reached the beams are synchronized to cross in the six interaction regions. The tuning of the two beam crossing points is known as beam cogging. In the interaction regions, the cogged beams are focused and steered for collisions by quadrupole magnets. At top energy, 100 GeV, RHIC has achieved ^{197}Au+^{197}Au luminosities of $\sim 10^{26}$ cm^{-2}s^{-1}.

The capabilities of RHIC are not limited to the ^{197}Au+^{197}Au systems at one particular energy. The facility can accelerate and collide ions ranging from H (protons) to ^{197}Au over a wide range of energies. The energy range can be defined for various species through a per nucleon $\beta\gamma$ factor. At RHIC, the per nucleon $\beta\gamma$ range is from $18.1\frac{Z_{beam}}{M_{beam}}$ GeV, at the injection energy, to $250\frac{Z_{beam}}{M_{beam}}$ GeV, where the magnets of the rings pose the upper limit. RHIC can also collide and accelerate non–symmetric systems and polarized protons. To help distinguish nuclear and partonic effects, RHIC's long range plan includes species scans and deuteron–nucleus collisions.

2.2 The Design of the STAR Detector

The Solenoidal Tracker at RHIC (STAR) is an ensemble of detectors optimized to measure the final state hadrons from heavy ion collisions. The year 2000 configuration of STAR focused on the detection of charged particles about mid–rapidity and the reconstruction of particle decays, such as the $K^0_S \to \pi\pi$ and $\Lambda \to p\pi$.

During the data run of the 2000, the STAR detector system, shown in Figure 2.2, consisted of a large Solenoidal Magnet, Central Time Projection Chamber (TPC), Central Trigger Barrel (CTB), two Zero Degree Calorimeters (ZDC) and a Ring Imaging Čerenkov detector (RICH). The CTB and the two ZDCs were used for event triggering and for the determination of event centrality. The large TPC, with the aid of the 0.25 T Solenoidal Magnet, acted as the main tracking unit. The RICH extended STAR's particle identification to higher momentum. In year 2001, the capabilities and acceptance of STAR were enhanced by an increased 0.5 T tracking field, the addition of two Forward TPCs, slats of the Barrel Calorimeter, a Silicon Vertex Tracker (SVT) and a patch of the Time of Flight (TOF).

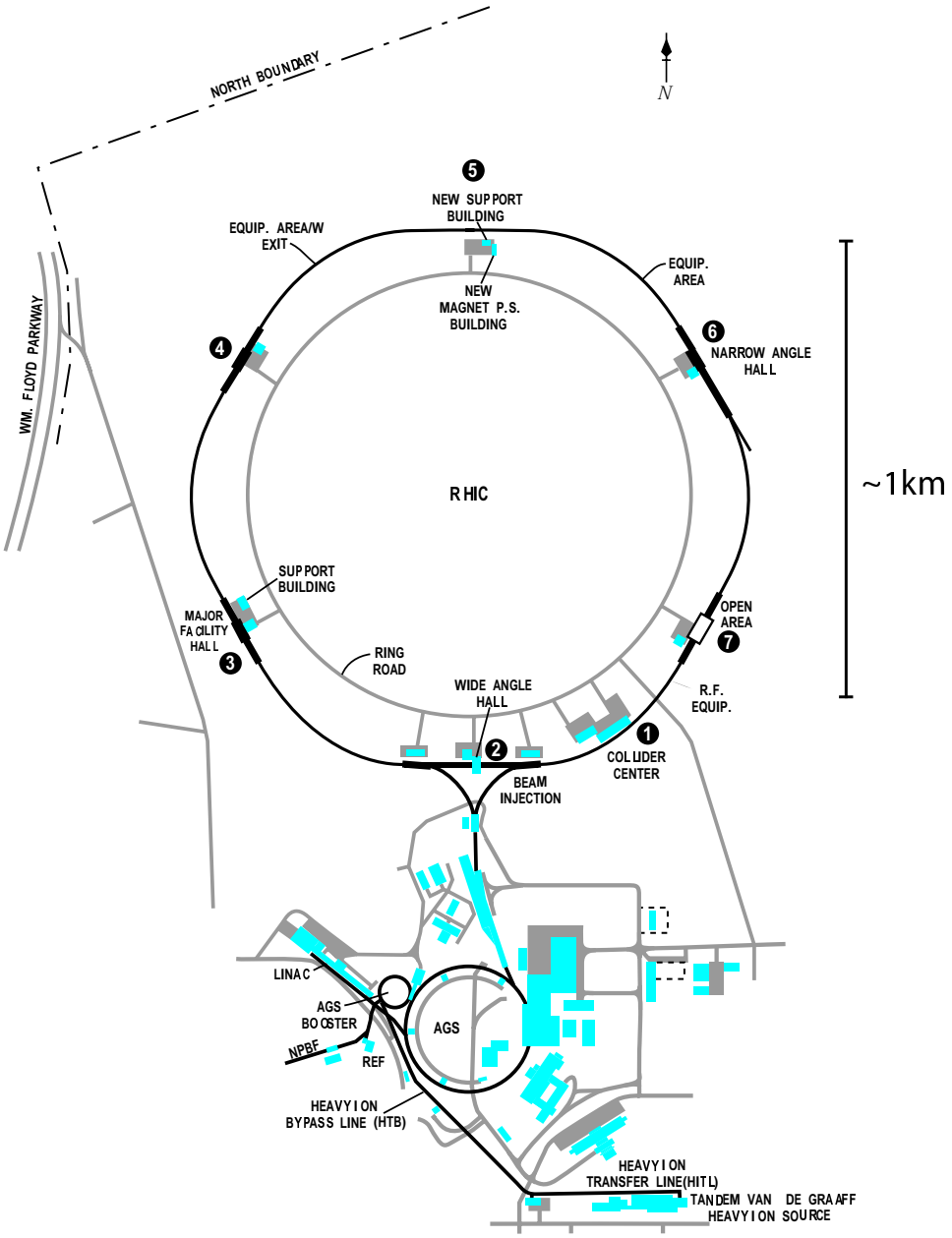

Figure 2.1: Top view of the Heavy Ion Facility at Brookhaven National Laboratory. The ^{197}Au acceleration starts in a Tandem Van de Graaff at the bottom right. The ions are transferred to the small Booster ring via the Heavy Ion Transfer and Bypass Lines. After the Booster the ions are moved into the AGS, medium ring, and then onto RHIC, large ring. RHIC supplies BRAMHS (6), PHOBOS (4), PHENIX (3) and STAR (2) with ultra–relativistic heavy ion collisions. The figure has been taken from [Pro94].

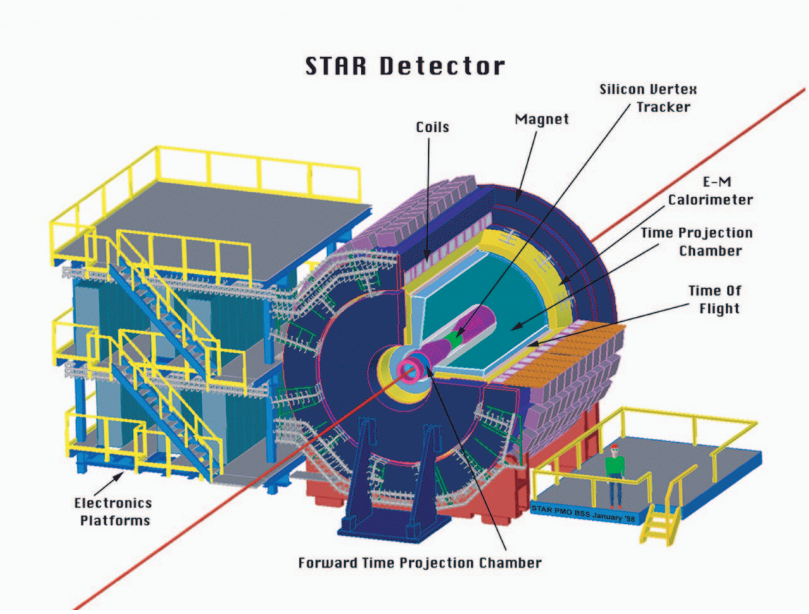

Figure 2.2: The STAR detector system. The figure displays the size and cylindrical geometry of the STAR detector system. The RHIC beams collide along the line drawn through the axis of the cylinder. This figure has been taken from [Col92].

2.2.1 The STAR TPC

The typical TPC is a large gas filled detector that measures three–dimensional space–points along charged particle trajectories. TPCs are designed to make many space–point measurements along a particle's path with minimal disturbance to the original trajectory. In comparison to silicon detectors, modern TPCs have coarser position resolutions, but make multiple measurements over larger volumes. Due to high costs and multiple scattering issues, the use of silicon detectors is typically limited to situations where fine position resolution is essential, such as in thin detectors close to the collision vertex.

The cylindrical geometry of the STAR TPC extends 4.2 m in length and 2 m in radius, as shown in Figure 2.3. The ionization region or active volume of the TPC is more than 45 m^3. This volume is kept slightly above atmospheric pressure (2 mbar) and filled with 10% CH_4 and 90% Ar gas (P10). Signals originate from electrons that are freed when moving charged particles ionize the gas. The positive ions and free electrons move apart under the influence of a 147 V/cm electric field between the central membrane and end caps of the TPC. The positive ions are carried to the cathode at the central membrane and the electron clouds drift towards the ends of the detector. Positive ions are neutralized when they reach the cathode plane and the electron clouds are amplified in a Multi–wire Proportional Chambers (MWPC) close to the end caps. Since the drift velocity of the electrons is known, one coordinate (z) of the starting point can be deduced from the time taken for the electrons to drift to the MWPC. The other two coordinates are found through the projection of the signal onto a pad plane mounted below the MWPC. The pad plane lies perpendicular to the beam axis and is segmented into 136,608 pads. The electronics are capable of recording 512 time bins from each pad, of these, about 348 are read out between the central membrane and the MWPC. In total,

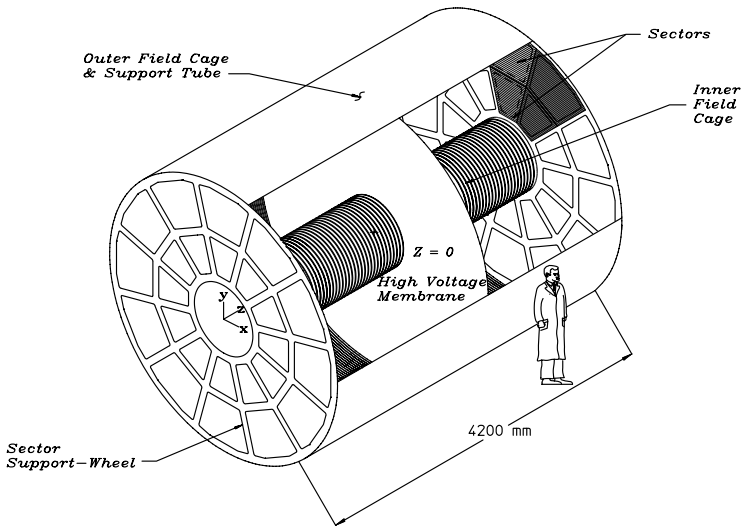

Figure 2.3: Cylindrical geometry of the STAR TPC's gas volume and the sector layout on the endcaps. This figure has been taken from [A$^+$].

the volume is effectively divided up into more than 47 million space–points.

The three wire planes of MWPC are shown in Figure 2.4. The anode wires are closest to the pad plane and are 20 μm in width. The inner sector anode wires are set to 1170 V and the outer to 1390 V. The combination of the fine width and high voltage on the anode wires produce a strong radial field near the surface of the wires. Drift electrons create ionization avalanches as they accelerate towards the positive anode wires. Positive ions created in these avalanches produce image charges on the pad plane.

The shield grid is the middle plane of wires that separates the drift volume from the amplification region. The shield grid has three main functions: to provide a ground plane for the drift field, to shield the pad plane from the gated grid and to capture some of the positive ions created near the anode wires. The drift field is established between the 31 kV central membrane and grounded shield plane. The shield grid significantly reduces the signals induced on the pads when the gated grid opens. This prevents these induced signals from compromising the resolution of ionization signals at the beginning of the drift period. A large fraction of the slowly drifting positive ions created near the anode wires are neutralized on the wires of the shield grid. Positive ions that drift into the active volume, leakage current, cause distortions in the drift field.

The gated grid is furthest from the pad plane. The main purpose of the gated grid is to stop non–triggered ionization from reaching the amplification region and stop positive ions created in the amplification region that leak past the shield grid from reaching the active volume. Stopping non–triggered electrons extends the life of the TPC by preventing unnecessary ionization from occurring in the amplification region. More importantly, the time that the gated grid is open is much less than the time needed for a positive ion to drift past the gated grid so this last wire plane neutralizes the positive ions that leak past the shield grid. The electric field lines for both the open and closed

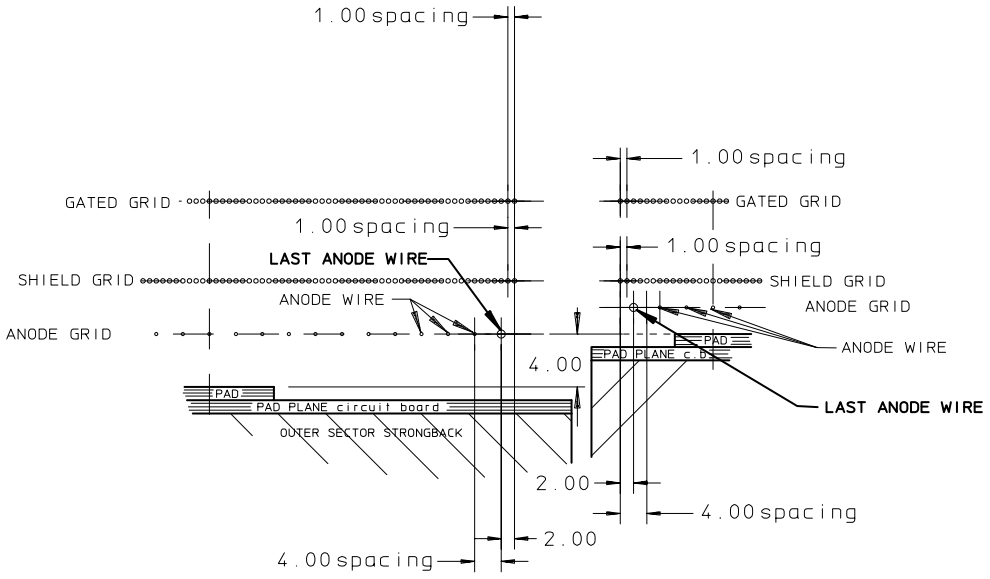

Figure 2.4: The three wire planes of the Multi–Wire Proportional Chamber of the STAR TPC. The outer and inner sector geometries are shown on the left and right, respectively. This figure has been taken from [HS99].

gated grid states are shown in Figure 2.5. In the closed state, adjacent gated grid wires alternate from positive to negative potentials. These potential differences set up electric fields between the wires that are perpendicular to the drift direction. The fields capture the non–triggered electrons and positive ions. In the opened state, the voltage on the gated grid wires is set to the corresponding equipotential surface of the drift field. In this state the gated grid is transparent to the drift electrons.

The TPC pads are laid out in sectors that cover 30° in azimuth, as shown in 2.3. There are 24 identical sectors mounted on the east and west ends of the TPC. Each sector has 13 inner and 32 outer pad rows, as shown in Figure 2.6. Effectively, the pads are plate capacitors. Local electric field changes are created on the surface of the pads by the slowly drifting positive ions created in avalanches near the anode wires. These local field changes induce currents on the pads and subsequently in the TPC electronics.

2.2.2 TPC Electronics

The TPC readout electronics boards are mounted on the back of each sector. Each sector has 181 analog Front End Electronics boards (FEE) and six digital readout (RDO) boards. The circuitry on each FEE is separated into two parallel 16 channel circuits and is capable of covering up to 32 pads. The analog signals on the TPC pads are amplified, shaped, stored and digitized in two chips on the FEE. The Pre–Amp/Shaper–Amp (SAS) amplifies and shapes the signal. The SAS feeds the 512 slot switch capacitor array (SCA). This chip is an analog storage unit that also contains an analog to digital converter. The chip allows fast, low–noise sampling of the signal with minimal power consumption. It also permits digitization and readout of data at a reduced rate. Upon request the SCA chip digitizes the stored voltages on the capacitors and passes them onto a multi–plexer on the RDO board. The multi–plexer communicates via fiber optic links with the data acquisition (DAQ)

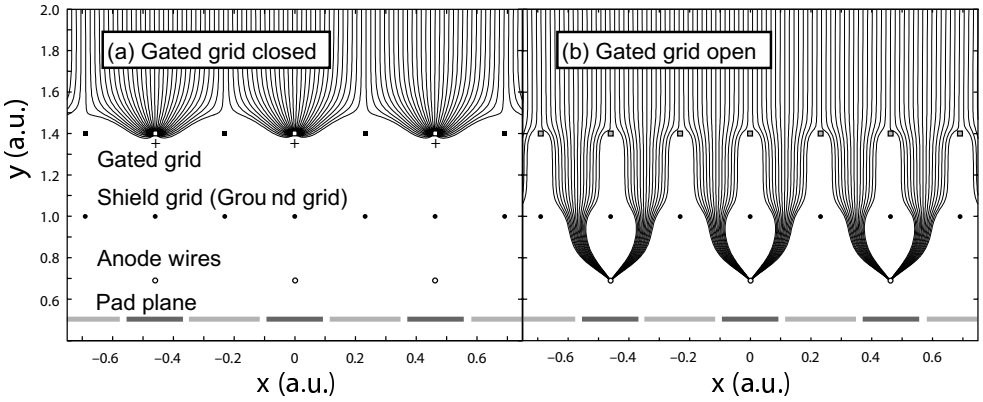

Figure 2.5: The closed (a) and open (b) states of the a gated grid. The electric field lines of the two configurations are indicated. In the closed state electrons drift to and terminate on the gated grid wires. In the open state the wires are transparent to drifting electrons. This figure has been taken from [Gro00].

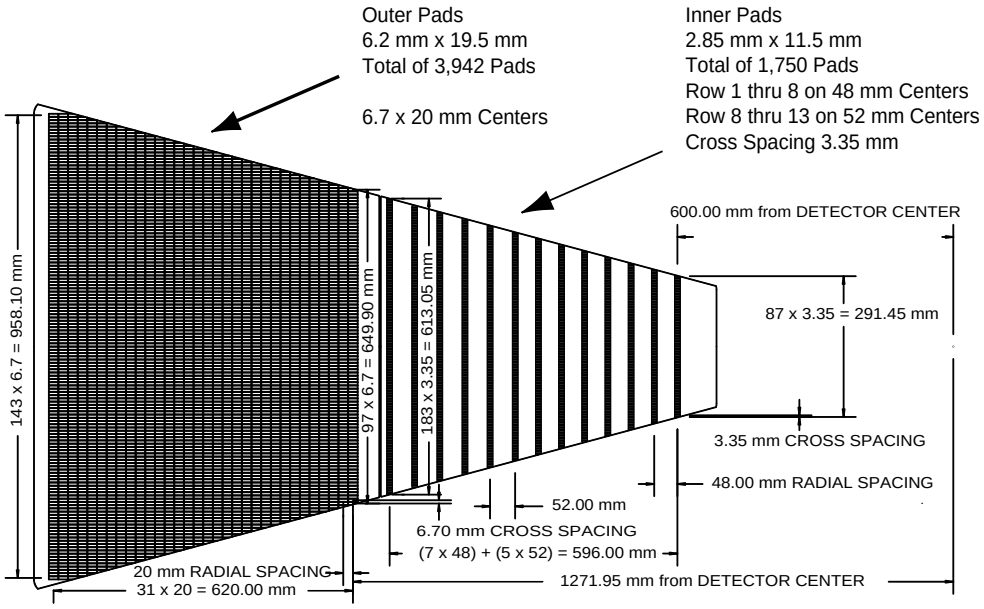

Figure 2.6: Pad plane of one TPC sector. Each sector contains 5692 pads. The inner and outer pad geometries differ to compensate for the radially decreasing hit density. This figure has been taken from [A$^+$].

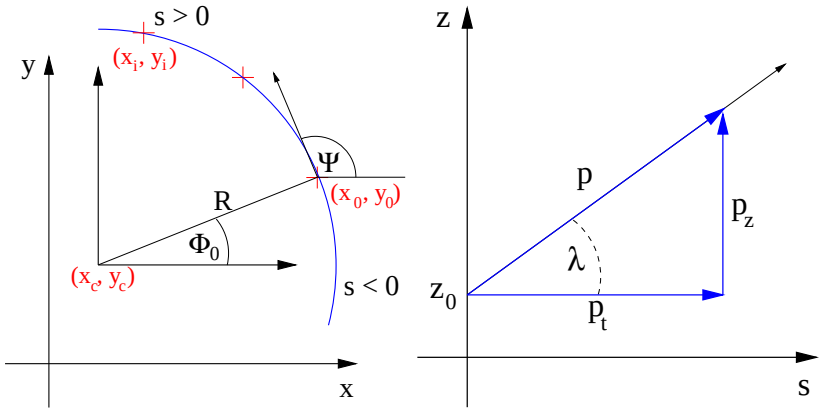

Figure 2.7: Geometric definitions of some commonly used track parameters. This figure has been taken from [NU02].

crates. These crates are responsible for packing the data into DAQ files and shipping them to a High Performance Storage System (HPSS). The data is later retrieved from HPSS for offline analysis.

2.3 TPC Hit and Track Finding

Electron–cluster finding along the TPC time dimension (z) is preformed in the DAQ crates, before the data is shipped to HPSS. The remaining hit reconstruction is accomplished off–line by scanning along rows for adjacent pad signals. Each pad row is treated separately and hits are not reconstructed across different pad rows. The DAQ files are processed through a chain of algorithms that construct hits from the distribution of the digitized signals on the pads. The requirements of a hit are defined by a set of parameters, called ASIC parameters. The ASIC parameters specify the number and threshold of adjacent signals that are necessary for a hit. Tracks are found from the array of hits in an event. The track–finding routine starts in the outermost pad rows where the density of hits is the least. It searches for groups of three hits that lie close in physical space. These groups are the initial "roots" of tracks. Track segments are formed from roots through linear extrapolations to adjacent pad rows and clusters in z. Since the STAR magnetic field guides charged tracks into helical trajectories, segments are extended inward and outward with helical extrapolations. After these extensions, a minimum number of 5 hits is required on each track so that the five parameters of the track's helix model are uniquely defined. If this requirement is not met, then the "fit flag" of the track is set to -10. Tracks are fit in two independent projections of the helix. A circular projection is fit in the plane perpendicular to the magnetic field, the xy-plane. A line is fit in the sz-plane, where s is the length along a track's circumference [MS94]. Kinematic variables of a track are calculated from the parameterization of the helix; found via the circular and linear fits, and the direction and magnitude of the magnetic field. The definitions of some track parameters are given in Figure 2.7, while a more complete list of commonly used track parameters and their definitions can be found in Appendix A. Final track parameters are obtained with a refit that uses a Kalman filter, which compensates for multiple scattering and energy loss in the TPC gas.

Symbols	Definition	Units or Value
m_e	electron mass	0.510999 MeV/c^2
r_e	classical electron radius	2.81794092 fm
N_A	Avogadro's number	6.0221367×10^{-23} mol^{-1}
K	$4\pi N_A {r_e}^2 c^2$	0.307075 MeVg^{-1}cm^2
q	charge of the particle	
Z	Atomic number of the medium	
A	Atomic mass of the medium	
I	Mean excitation energy	MeV
T_{max}	maximum kinetic energy that can be imparted to a free electron in a single collision	
δ	Bethe–Bloch density effect correction factor	

Table 2.2: Physical constants [Gro00] used in the Bethe–Bloch function, Equation (2.1).

2.4 dE/dx Particle Identification with the TPC

Charged particles lose energy while traversing matter. The main process contributing to this energy loss is Coulomb scattering with electrons in atomic orbits. The pulse heights of the pads that comprise a hit provide a measure of this energy loss in the TPC gas. These pulse heights are summed and divided by the track's crossing length over the pad row in order to obtain the energy loss per unit length for each hit. The distribution of the energy loss samples for hits along a track has a Landau–like shape. An estimate of the mean of this distribution is calculated by computing the average of the bottom 70%. This results in a measure of the energy loss per unit distance along a track, dE/dx, in the TPC gas. The STAR TPC is optimized to measure tracks of p_t from 0.1 GeV/c to 10 GeV/c. At these momenta, the dE/dx of particles with $m \gg m_e$ is characterized by a particle's charge (q), velocity (β) and the properties of the medium that is traversed. This average energy loss is described by the Bethe–Bloch function [Gro00], Equation (2.1). The TPC measures the average energy loss, but does not directly measure a particle's velocity. Particle identification instead relies on a particle's rigidity –momentum divided by the charge– which is directly measured (see Appendix A). With this information, particle identification is accessible and obtained from the correlation between a particle's mass and charge.

$$-dE/dx = Kq^2 \frac{Z}{A} \frac{1}{\beta^2} \left(\frac{1}{2} ln \frac{2m_e c^2 \beta^2 \gamma^2 T_{max}}{I^2} - \beta^2 - \frac{\delta}{2} \right), \tag{2.1}$$

constants and variables are defined in Table 2.2.

"Ionization loss by electrons and positrons differs from loss by heavy particles because of the kinematics, spin, and the identity of the incident electron with the electrons which it ionizes" [Gro00]. Above a few hundred MeV/c of momentum, the dE/dx of electrons remains essentially constant with increasing momentum. The electron band is sharply crossed by other particle bands as they approach their minimum ionizing value, as illustrated in Figure 2.8. With a high level of confidence particles can be identified in regions where the dE/dx bands are not overlapping. In regions where bands are partially merged, simultaneous Gaussian fits to the bands in momentum slices are used to extract the probability that a track is of a given particle species. With the tracking field at .25 T, the STAR TPC has a one sigma dE/dx resolution of about 8.2% of the dE/dx value. This value for sigma was determined with a clean sample of electrons and positrons from photon conversions. The knowledge of both a predicted dE/dx value (Bethe–Bloch function) and the resolution of dE/dx is

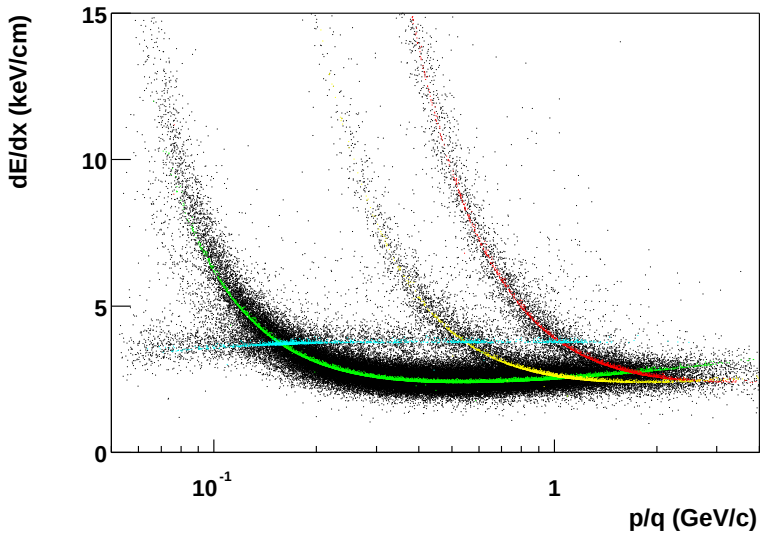

Figure 2.8: Ionization energy loss of charged particles in the TPC gas, 10% CH_4 and 90% Ar. The lines indicate the predicted dE/dx bands of the Bethe–Bloch function for e (blue), π (green), K (yellow) and p (red) candidates.

very powerful. With both, a known fraction of a certain particle band can be sacrificed in order to eliminate other particles. This is accomplished by requiring the dE/dx of all particles to fall within so many sigma of a predicted band (dE/dx deviant).

2.5 Event Triggering

Triggers are essential to optimize the quality and quantity of the data. In STAR, triggers are especially important because the data taking rate is limited by the transfer speed to HPSS. The RHIC strobe, ZDCs and Central Trigger Barrel scintillators provide the information for the trigger logic. The RHIC strobe is a pulse edge that indicates the time when bunches cross in the interaction region. The ZDCs and CTB are two fast detectors that provide event characteristics on a nanosecond time scale. The ZDCs are located along the beam axis on both sides of STAR and detect the number of unbound neutrons at beam rapidity. The charged particle multiplicity around mid–rapidity is supplied by the CTB. During the year 2000 data run, there were two trigger logics that focused on obtaining an unbiased data set and high–multiplicity data set. In 2001, the arrival time of neutrons in the ZDCs was also used to select events with z vertex positions near the center of the TPC.

The minimum bias trigger was the simplest and least biased trigger. It was designed to avoid triggering on empty events, but was optimized to cover more than 80% of the hadronic cross section of ^{197}Au+^{197}Au collisions at $\sqrt{s_{\rm NN}} = 130$ GeV [A$^+$01a]. The trigger was based on the RHIC strobe and coincident ZDC signals. If both of the ZDCs, east and west, returned a signal above a threshold in sync with a pulse from the RHIC strobe; then the event was recorded and written to HPSS.

The central trigger was designed to capture collisions which result in high multiplicity events. Along with a pulse from the RHIC strobe, the trigger relied on information from the ZDCs and CTB.

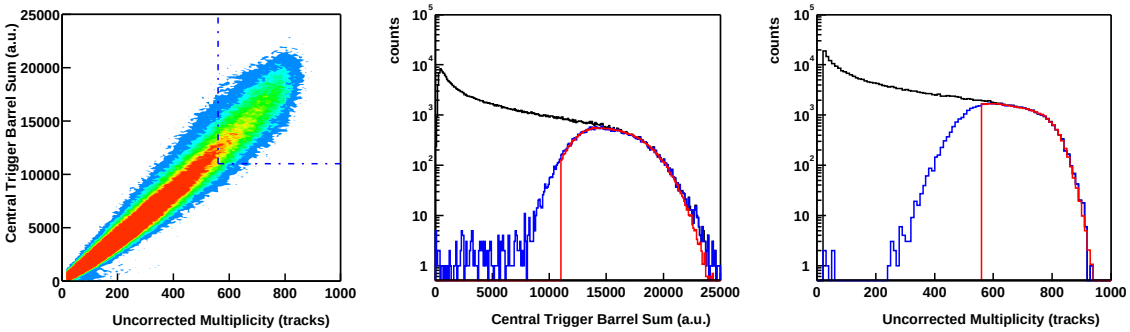

Figure 2.9: CTB sum and uncorrected multiplicity distributions of the minimum bias and central trigger data. Left: The correlation between the CTB sum and the uncorrected multiplicity for data taken with the minimum bias trigger. The dashed lines indicate the CTB threshold of the central trigger (11000 a.u.) and the lower edge of top 11% centrality cut on the uncorrected multiplicity (560 tracks), horizontal and vertical respectively. Center: The CTB sum distributions for data taken with the minimum bias trigger (black), the minimum bias trigger with the top 11% of the hadronic cross section cut on the uncorrected multiplicity (blue) and the central trigger with the top 11% of the hadronic cross section cut on the uncorrected multiplicity (red). Right: The uncorrected multiplicity distributions for data taken with the minimum bias trigger (black), the minimum bias trigger with the central trigger CTB sum cut (blue) and the central trigger with the top 11% of the hadronic cross section cut on the uncorrected multiplicity (red).

The central trigger required a ZDC coincidence signal and high occupancy in the CTB. This trigger captured more than 96% of the top 11% of the hadronic cross section when determined through the uncorrected multiplicity. This small, less than 4%, bias was measured by calculating the fraction of events that do not pass the central trigger CTB requirement in a minimum bias data sample with the top 11% centrality cut on the uncorrected multiplicity. The correlation between the CTB sum and uncorrected multiplicity, CTB sum distribution and uncorrected multiplicity distribution are shown in Figure 2.9.

Chapter 3

Data Analysis

Photons were measured by reconstructing photon pair conversions, $\gamma Z \rightarrow e^- e^+ Z$, with electrons and positrons detected by the STAR TPC. The invariant mass of pairs of photon was used to extract the yield of π^0s. Spectra of both photons and π^0s were produced for various event centrality classes.

3.1 Event Selection and Centrality Definitions

In this analysis, events were required to have a primary vertex position less than 150 cm from the geometric center of the TPC along the beam axis. About 87% of the events in the minimum bias trigger data set passed this cut. This primary vertex range also increased the average photon conversion probability between the primary vertex and the TPC by utilizing conversions in the SVT support cone material. This additional material substantially aids the analysis, since the design of the STAR detector system kept material to a minimum "To minimize multiple scattering and photon conversion after π^0decay" [Col92]. A wider vertex cut was not chosen to prevent the introduction of acceptance effects near the edges of the TPC. The vertex position was also required to be within 4 cm of the beam axis to eliminate events with stray vertex positions outside of the beam pipe. Under these conditions, the vertex finding efficiency is approximately 90% for events with 30 tracks and plateaus at 99.9% for events with more than 50 tracks. The centrality of events was determined through the number of reconstructed primary tracks in the pseudo–rapidity range $|\eta|<0.75$. This uncorrected multiplicity was mapped on to the fraction of the hadronic cross section, as illustrated in Fig. 3.1. The mapping accounted for the loss of low multiplicity events that arose from the vertex finding inefficiency. These centrality definitions are referred to in both the photon and π^0 analyses.

3.2 Reconstruction of Photon Pair Conversions $\gamma Z \rightarrow e^- e^+ Z$

The dominant interaction process for photons with a total energy above 10 MeV is pair conversion, $\gamma Z \rightarrow e^- e^+ Z$. Photon pair conversion occurs in the electric field of a nucleus or an orbiting electron. The pair conversion cross section in the field of the nucleus, Equation 3.1, depends only on the atomic number (Z) of the atom.

$$\sigma_{pair} = 4Z^2 \alpha r_e^2 \left[\frac{7}{9} ln \frac{183}{Z^{1/3}} - \frac{1}{54} \right], \tag{3.1}$$

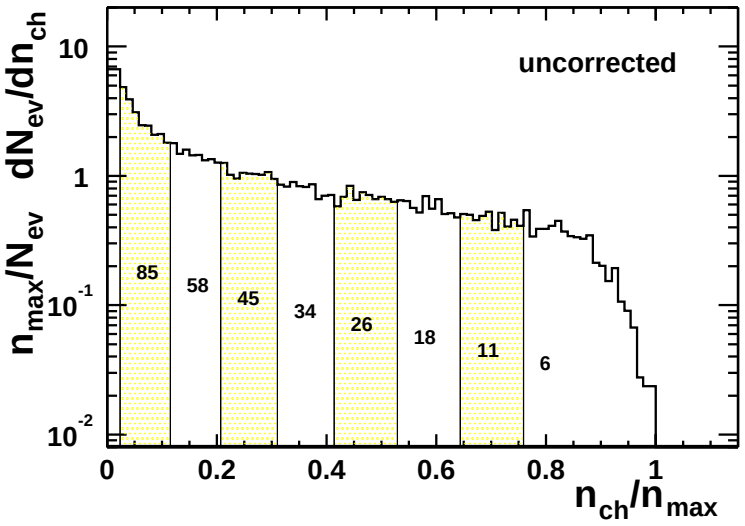

Figure 3.1: Measured uncorrected multiplicity, the number of primary TPC tracks within -0.75< η <0.75, distribution for ^{197}Au+^{197}Au collisions at $\sqrt{s_{\rm NN}}$ = 130 GeV. Table 3.1 links the labeled bins in the uncorrected multiplicity distribution to the fraction of the hadronic cross section. This plot was taken from [A$^+$01a].

Centrality Bin	Uncorrected Multiplicity	Fraction of the Cross Section
1	20–100	58–85%
2	100–180	45–58%
3	180–270	34–45%
4	270–360	26–34%
5	360–460	18–26%
6	460–560	11–18%
7	560–660	6–11%
8	>660	top 6%

Table 3.1: Centrality bins as defined with the uncorrected multiplicity and linked to the "Fraction of the Cross Section", for ^{197}Au+^{197}Au collisions at $\sqrt{s_{\rm NN}}$ = 130 GeV. These numbers were taken from [A$^+$01a]

where α and r_e are the fine structure constant and the classical electron radius. This equation was taken from [Per86]

In the case where the pair conversion occurs in the electric field of the nucleus, a negligible amount of momentum is transferred to the recoiling nucleus and the outgoing pair carries most of the initial energy of the photon. Even though there are Z electrons orbiting a nucleus, to first order the probability of conversion in the field of an orbiting electron is suppressed by a factor of $1/Z$ relative to conversion in the field of the nucleus, because of the Z^2 dependence in the photon conversion cross section. Conversion in the field of an orbiting electron poses as a background for pair conversion reconstruction. The recoiling electron can carry a substantial fraction of the incident photon's energy, leaving the detected pair with only a portion of the energy.

In this analysis, the STAR TPC was used as a pair spectrometer to reconstruct photons that convert in the detector material. The conversion probability depends on the cross section or Z of the atoms, and density (ρ) of the local medium. The average conversion probability for a photon to convert before or in the TPC gas was about 1% in the year 2000 data and 5% in 2001 data with the addition of the SVT silicon ladders. The low conversion probability before or in the TPC is compensated by the large acceptance of STAR and its excellent energy resolution. Calorimeters with high efficiencies are typically used to detect photons in heavy ion experiments, though their acceptance is commonly limited structurally and by costs. In comparison to the use of calorimeters, this method can detect lower energy photons, 0.1 GeV, and has better energy resolution $\Delta E/E \approx$ 2% at 0.5 GeV.

Photon candidates were found by searching for track pairs with pair conversion characteristics. The selection criteria were based on the topology of pair conversion and charged particle identification via dE/dx. A combination of track and pair cuts were used to select photon candidates and reduce false photon candidates. The three stages in the photon finding routine were track selection, pair selection and primary photon selection. At the track level, electron and positron candidates were found. Track cuts were used to select well defined tracks and remove improbable conversion daughters. In the pair selection step, oppositely charged tracks were paired and passed through a geometric filter. This filter constrained the pairs to have the conversion topology. The last step reduced secondary photons by requiring photon candidates to point back to the primary vertex.

3.2.1 Topological Signature

The small opening angle between the electron and positron of a photon conversion gives it a unique topological signature. The topology can be summarized as two tracks of opposite charge, with electron energy loss characteristics, emerging from a secondary vertex with a small opening angle. The opening angle for a photon conversion is on average $\sim 2m_e c^2/E_\gamma$ radians [Per86] or 0.01 radians for a photon with 0.1 GeV of energy. As the electron and positron leave the secondary vertex they are separated by the STAR magnetic field, as shown in Figure 3.2.

3.2.2 Electron and Positron Track Selection

The algorithm for selecting electrons and positrons was designed to choose well defined tracks and reduce the number of track pair combinations. Track quality cuts essentially eliminated the double counting of split tracks. The number of track pair combinations was reduced by removing tracks that did not contain the track level characteristics of conversion products, and through the binning of negative and positive tracks.

Three variables were used to defined a track's quality: the "fit flag", the number of hits included in a track's fit (nhitf) and the ratio of nhitf to possible hits. The helical fit to a track was checked

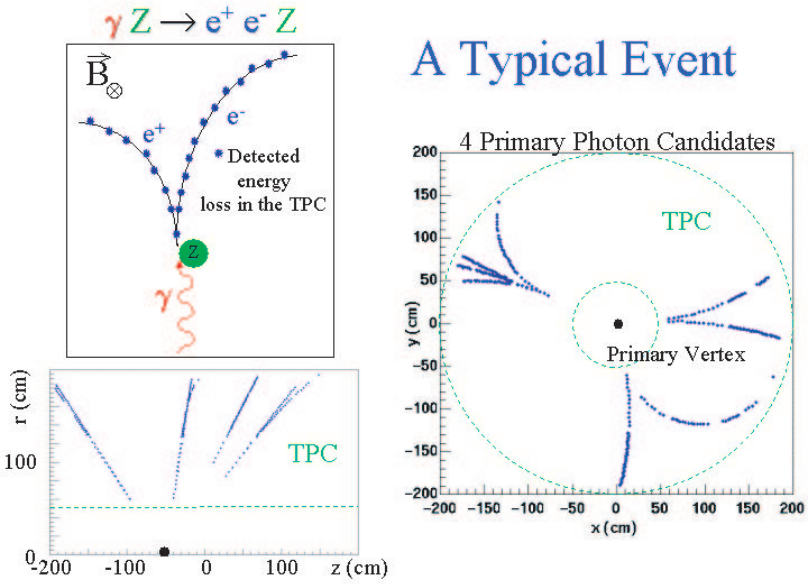

Figure 3.2: Top Left: A Schematic diagram of the topology of a photon conversion in the electric field of a nucleus and the ionization trails of the electron and positron tracks in the TPC gas. The external magnetic field bends the two tracks of opposite charge apart. Right: An xy-plane projection of TPC hits from the tracks of four photon candidates in a real event. All other hits were removed. Bottom Left: The rz-plane projection of TPC hits from the same four candidates. Notice that the hits of tracks within the pairs lay on top of each other. This results from the small opening angle of the pair and the lack of a magnetic field perpendicular in this plane to separate the tracks.

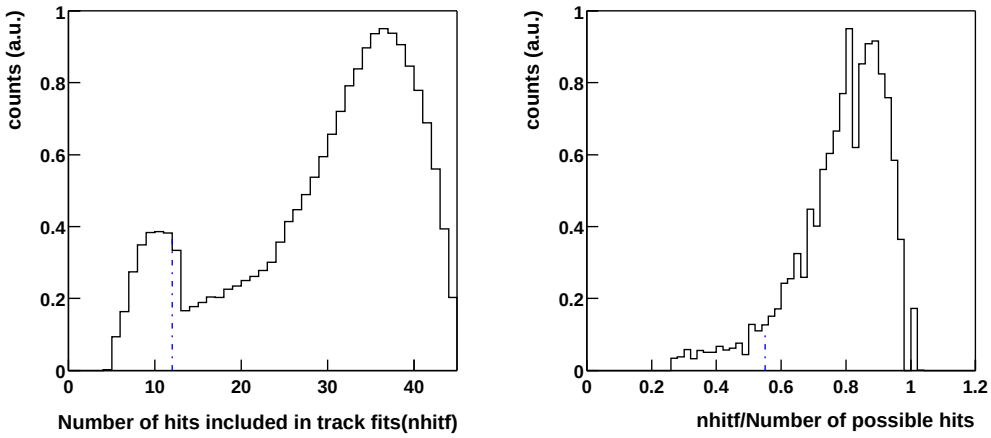

Figure 3.3: Distributions of the number of hits included in track fits (nhitf) and the ratio of nhitf to the number of possible hits, left and right respectively, for electron and positron candidates from photon conversion candidates from a minimum bias event sample. The dashed lines indicate where the cuts were placed in the photon finding algorithm. The sharp drop at 13 in the nhitf distribution aroses from the tracks that split between the inner and outer sectors. For the pad row geometry on sectors refer to Figure 2.6.

by requiring the "fit flag" to be positive, as described in Section 2.3. A track's fit was also required to use more than 12 hits (nhitf>12). This requirement assured that the five parameters of the track's helix were well constrained and reduced the impact that possible ghost hits had on the helix parameterization. The distribution of nhitf is shown in Figure 3.3. Split tracks were removed by requiring the ratio of nhitf to the number of possible hits on tracks to be greater than 55%. Hits were not shared between tracks so only one segment of a split track could have a ratio greater than 55%. The number of possible hits was calculated by extrapolating a track's geometry over the pad plane. The calculation incorporated both the detector geometry and features of the track finding routine. This calculation also correctly handled daughters from photon conversions that occurred within the tracking volume of the TPC. The distribution of the ratio of nhitf to the number of possible hits is shown in Figure 3.3.

A topological cut, dE/dx particle identification and track binning were used to reduce unnecessary combinations of track pairs. The topological cut was based on the signed distance of closest approach to the primary vertex (sdca) in the xy-plane, Equation 3.2.

$$\text{sdca} = \sqrt{(x_c - x_p)^2 + (y_c - y_p)^2} - r, \tag{3.2}$$

where (x_c,y_c) is the helix center, r is the radius of the helix and (x_p,y_p) is the primary vertex position.

Neglecting resolution effects, the very small opening angle and the conversion distance force the sdca to be positive for both the electron and positron of a primary photon conversion, as illustrated in Figure 3.4. The sdca was required to be positive for tracks with transverse momentum less than 0.3 GeV/c. In this transverse momentum region, the electron and positron dE/dx particle identification is limited and the track geometry is well defined. This cut eliminated about 30% of the

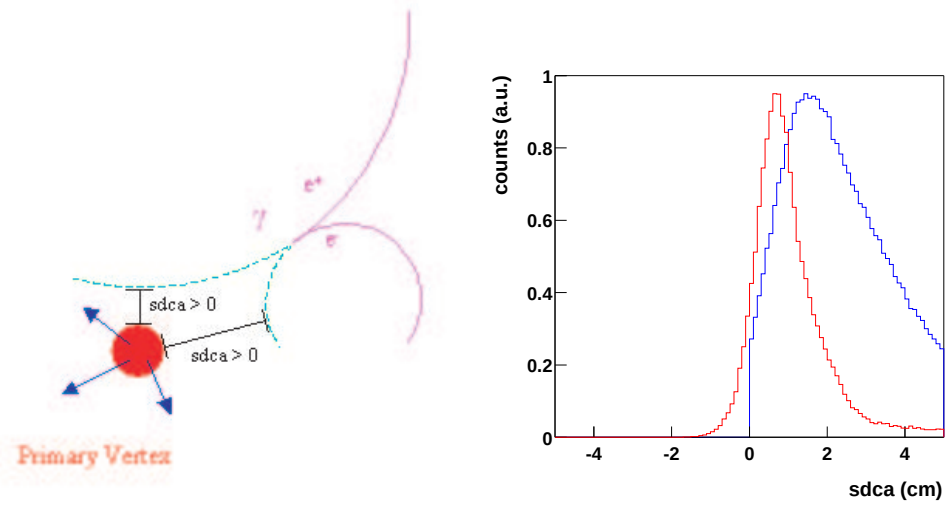

Figure 3.4: Signed distance of closest approach (sdca) diagram and distribution. The circular extrapolations in the xy-plane of the electron and positron from a primary photon conversion do not enclose the primary vertex, so both daughters have a positive sdca. The right plot contains sdca distributions for electron and positron candidates from a minimum bias event sample. The blue line is for tracks with p_t<0.3 GeV/c, where the sdca was required to be greater than 0. The red line is for tracks with 0.3<p_t<0.4 GeV/c, in this p_t region the sdca cut was not applied to the data.

random track pool, since approximately half the measured tracks have a transverse momentum less than 0.3 GeV/c and the sdca distribution for primary tracks is symmetric about zero. This reduced the number of track pairs by about 50% and in turn the probability of false photon candidates. Above a transverse momentum of 0.3 GeV/c, the value of a track's sdca becomes comparable to the sdca resolution. The benefit of the cut also decreases with increasing transverse momentum, since the inclusive particle yields are dropping and particle identification is improving for electrons and positrons.

Particle identification effectively removed pions, kaons and protons from the track pool above 0.2 GeV/c. 97.7% of the electron and positron candidates were retained by requiring the dE/dx deviant given the electron hypothesis to be between -2 and 4 sigma, as shown in Figure 3.5. The cut was chosen to be asymmetric and tighter on the negative side to eliminate the pion, kaon and proton contamination in regions where the dE/dx bands are below and run parallel to the electron band, Figure 2.8. A tight cut on the upper side of the electron dE/dx does not remove much contamination, because the other bands sharply cross the electron band from above. Applying a tight cut on the upper side of the dE/dx band would have introduced systematic uncertainties in the fraction that was removed. These uncertainties would be caused by the long non–Gaussian tail on the upper side of the dE/dx bands.

Electron and positron candidates were binned to reduce the number of track pair combinations. The binning utilized a measure of the opening angle in the non-bending plane, the dip angle difference, which is independent of the location of the secondary vertex. The electron and positron bins were 0.126 radians wide and offset from each other by 0.063 radians. The dip angle difference of electrons and positrons in nonadjacent bins was greater than a rough estimate of the largest accepted

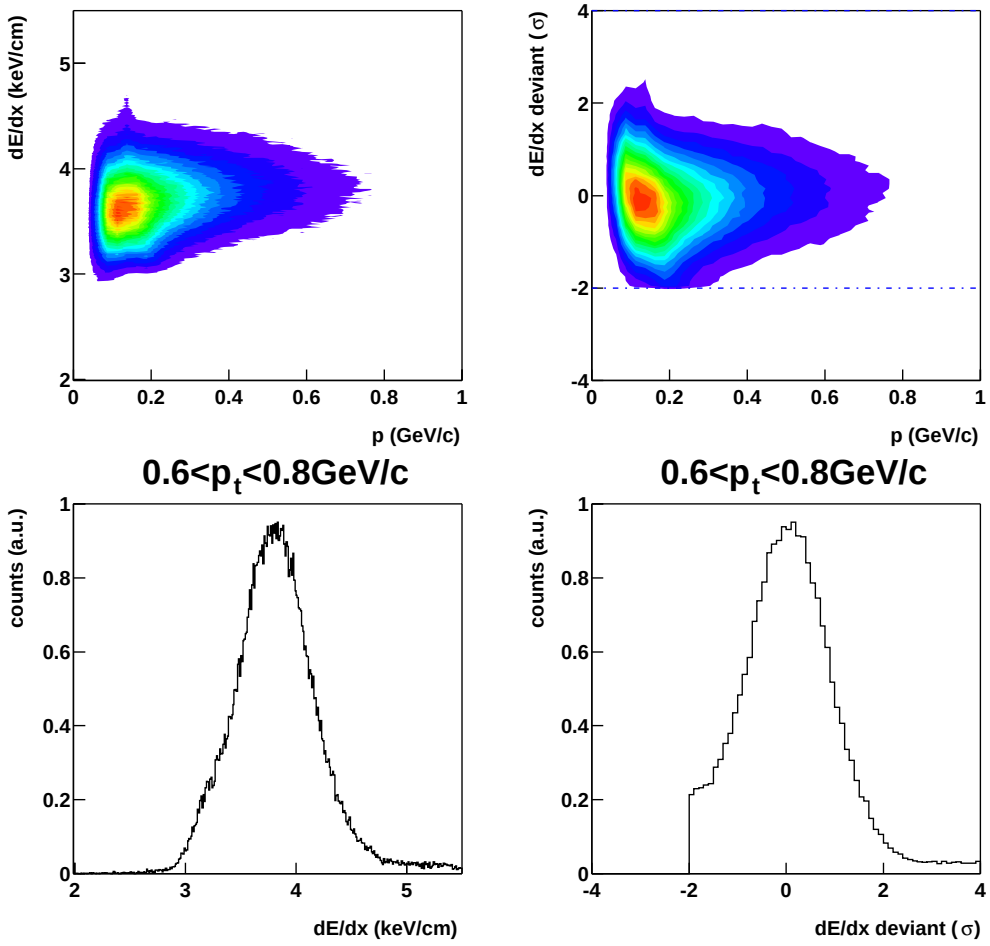

Figure 3.5: Measured dE/dx and dE/dx deviant distributions for daughters of primary photon candidates. The dashed line in the upper right plot indicates the minimum number of sigma cut, -2 σ, on the accepted track sample. The bottom two plots are projections of the dE/dx and deviant distributions.

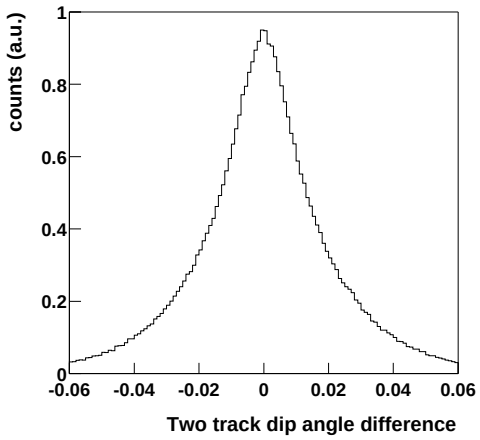

Figure 3.6: Angular difference in the rz-plane between daughters of photon candidates from a minimum bias event sample. The width of the distribution is dominated by the angular resolution of tracks in the rz-plane, $\sim$0.02 radians.

opening angle, 0.06 radians, so only tracks in adjacent bins had to be combined. This reduced the track pair combinations by about a factor of 5 and the computational time of the algorithm.

3.2.3 Photon Candidate Criteria

Photon candidates were selected based on the conversion topology. Pairs of oppositely charged tracks were required to originate from a secondary vertex with a small opening angle. Along with this topological requirement, the invariant mass assuming the electron and positron mass for the two particles was also checked.

The relative location of the track centers and the opening angle in the non-bending plane were the first two checks in the selection process. The first check removed pairs that would have a reconstructed momentum vector which points back towards the primary vertex. The negligible opening angle and finite conversion distance force the cross product of the vector to the positron helix center with the vector to the electron helix center, in the frame of the primary vertex, to line up with the magnetic field. Requiring pairs to have this feature prevented most short–lived decays that have a finite opening angle from entering the photon sample. The most precise measure of the opening angle is the difference between the dip angles of two tracks ($\Delta\lambda$). Two daughters that emerge from a photon conversion have a dip angle difference which is less than a tenth of the dip angle resolution, $\sim$0.02 radians. The dip angle difference between tracks, distribution shown in Figure 3.6, was required to be less than 0.03 radians.

Secondary vertices were found by extrapolating a pair of tracks to a common point in space. The algorithm started by finding the most probable crossing points in the bending plane, xy-plane, assuming that the pair of tracks had a zero opening angle. The zero opening angle assumption placed the crossing point somewhere between the centers of the two track helices. With this assumption, the distance of closest approach in the xy-plane between two tracks was found by calculating the difference between the center of the track helices in the xy-plane and the sum of the track radii. This distance was required to be less than 1.5 cm. The actual crossing point in the xy-plane was

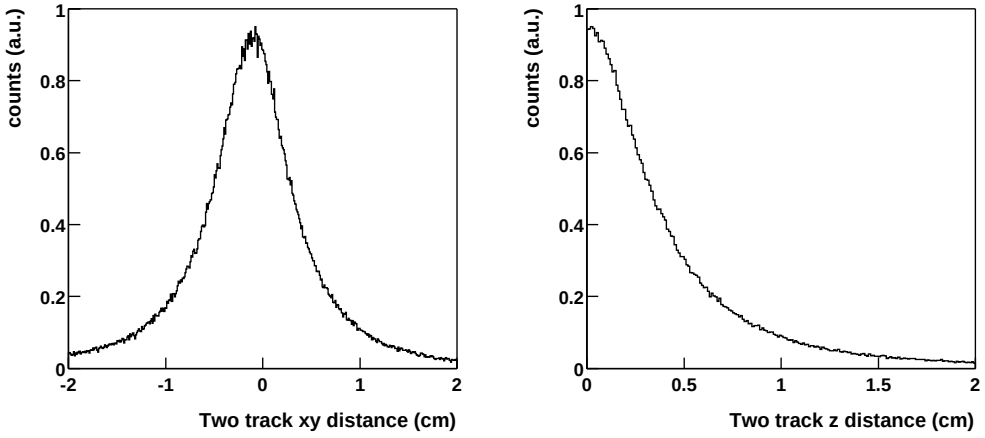

Figure 3.7: Distances between daughters of photon candidates in the xy-plane along the line connecting the helix centers (left) and along the z direction at the found conversion point (right).

found by weighting the position between the centers by the two radii, as give in Equation 3.3. Next, the tracks were extrapolated in z to the xy-plane crossing point. The z distance between the two tracks, at the crossing point, was also required to be less than 1 cm. Distributions of these distances are shown in Figure 3.7.

$$x_{conversion} = \frac{x_{c1}r_2 + x_{c2}r_1}{r_1 + r_2}, \tag{3.3}$$

where $x_{conversion}$ is the x or y coordinate of the conversion point, and x_c denotes the x or y coordinate of the helix center.

An opening angle and invariant mass cut on the electron and positron pair were applied to reduce secondary particle decays that remained in the sample. The maximum opening angle between the two tracks was set to 0.4 radians. It was chosen to compensate for the opening angle resolution in the xy-plane. This cut was aimed at removing low p_t pairs with large opening angles. The invariant mass of the pair assuming the electron and positron mass was also required to be close to zero. The invariant mass distribution has a sharp peak near zero and a broad peak close to 0.012 GeV/c^2, as shown in Figure 3.8. The invariant mass calculation treats the conversion as if it was a two body decay. Thus, the minimum mass returned by the calculation is twice the electron mass, 1.022 MeV/c^2. This causes the absence of zero valued photon masses in the distribution. The sharp lower mass peak is from pairs that do not overlap in the xy-plane and only the angular difference in the rz-plane can be used as the opening angle in the invariant mass calculation. The higher mass peak results from the poorer opening angle resolution in the xy-plane. Since the opening angle resolution in the xy-plane only moves and smears the invariant mass peak, a cut was placed on the invariant mass calculated using only the rz-plane projection of the opening angle. This cut required the invariant mass to be less than 0.012 GeV/c^2. This invariant mass distribution is also shown in Figure 3.8.

Photon conversion points were required to be more than 10 cm from the primary vertex in the xy-plane. This requirement reduced the number of random track pairs in the photon sample, by

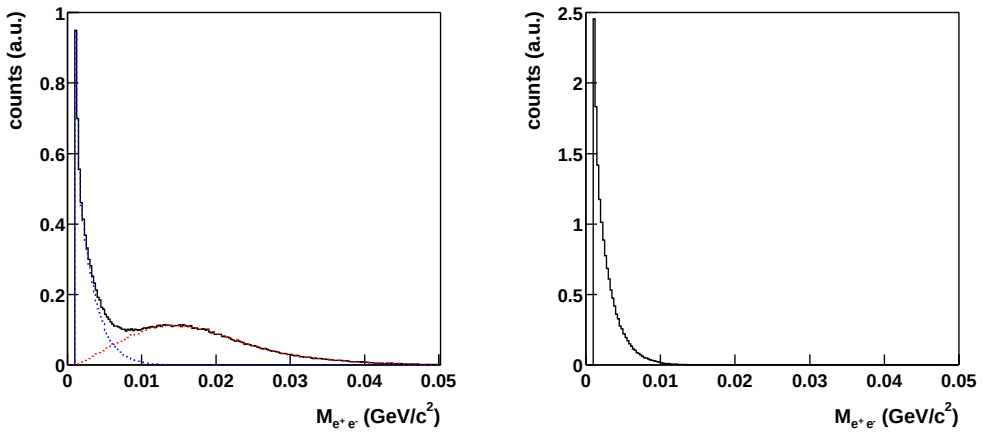

Figure 3.8: Invariant mass distributions of photon candidates assuming the electron and positron mass for the daughters. The distribution on the left can be separated into two contributions: track pairs that are parallel in the xy-plane at the conversion point (blue) and pairs that have a finite opening angle in the xy-plane (red). Thus, the peak near 0.012 GeV/c^2 is an artifact of the opening angle resolution in the xy-plane. In the right figure, the dominating xy-plane opening angle resolution effects were removed by assuming that all track pairs had a zero opening angle in the xy-plane and using only the rz-plane projection of opening angle in the calculation of the invariant mass.

excluding the region where the track density is the greatest.

3.2.4 Parameterization of Photons

The energy and direction of photon candidates were derived from the kinematic and helix variables of the two tracks. The energy of a photon candidate was calculated by summing the electron and positron energies. The angular direction in the xy-plane was obtained by crossing the vector from the helix center of the positron to the helix center of the electron with the magnetic field vector. The direction in the rz-plane was found by taking the average of the electron and positron dip angles. All kinematic parameters of a photon can be derived from these three variables. A compilation of these variables is provided in Appendix A.

3.2.5 Primary Photon Selection

Photons from the primary vertex and from short–lived decays, like the π^0 and η, were selected from the photon candidates by requiring the reconstructed momentum of the photon to point away from the primary vertex. The momentum vector of a primary photon has the same direction as the conversion point vector, the vector from the primary vertex to the location of the conversion. The conversion point vector and the momentum vector are compared in the rz-plane and xy-plane separately, because of differences in the angular resolutions of these measurements. In the rz-plane, a 0.035 radian cut was used to compensate for a directional resolution of $\sim$0.01 radians. A more relaxed cut of 0.05 radian was used in the xy-plane to account for a broader resolution, $\sim$0.015 radian. Both distributions are shown in Figure 3.9.

Cut	Value	Description
Event Cuts		
$\|x_{ver}\|$	<4 cm	primary vertex x
$\|y_{ver}\|$	<4 cm	primary vertex y
$\|z_{ver}\|$	<150 cm	primary vertex z
Electron and Positron Track Cuts		
fit flag	>0	helix fit flag
n_{fit}	>12	number of fit hits
$n_{fit}/n_{possible}$	>55%	split track check
sdca	>0	signed distance of closest approach
$\sigma_{dE/dx}$	-2–4	dE/dx Particle Identification
Pair Cuts		
$\left(\vec{x}^{e^+}_{cent} - \vec{x}_{ver}\right) \times \left(\vec{x}^{e^-}_{cent} - \vec{x}_{ver}\right)$	$\parallel \vec{B}$	relative location of the helix centers
opening angle	<0.4 radians	full opening angle
$\|\lambda_{e^-} - \lambda_{e^+}\|$	<0.03 radians	dip angle difference
d_{xy}	<1.5 cm	two track dca in the xy-plane
d_z	<1 cm	two track distance in z
$M_{e^-e^+}$	<0.012 GeV/c^2	invariant mass assuming xy-plane opening is 0
r_{xy}	>10 cm	radial conversion distance from the primary vertex
Primary Photon Cuts		
$\|\lambda_{conversion\ point} - \lambda_{\vec{p}}\|$	<0.035 radians	photon direction in the rz-plane
$\|\phi_{conversion\ point} - \phi_{\vec{p}}\|$	<0.05 radians	photon direction in the xy-plane

Table 3.2: Event, track, pair and primary photon criteria.

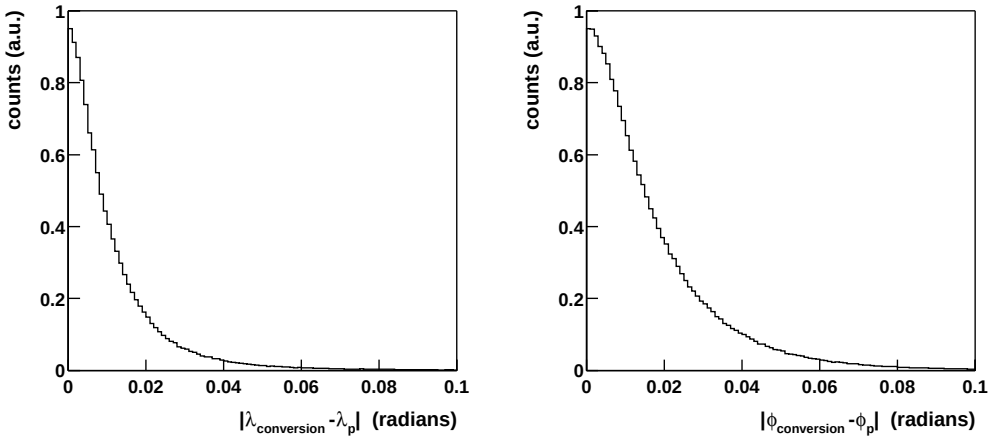

Figure 3.9: Angular differences between the photon conversion vector and momentum vector in the rz-plane and xy-plane, left and right respectively. The conversion vector is the vector from the primary vertex to the conversion point. The widths of these distributions are a consequence of a finite angular resolutions.

3.2.6 Photon Spectra

Photon yields were extracted as a function of p_t and y for a minimum bias data sample (0-85%) and three independent centrality classes (0-11%, 11%-34%, 34%-85%). These classes were chosen to be consistent with the π^0 centrality bins and the reasoning for them is later discussed in Section 3.3.1. Photons were identified under the standard event, track and photon selection criteria (Table 3.2) with a few exceptions. The event z vertex distribution was narrowed to $\pm$100 cm, the r_{xy} cut was varied from 10 cm to 40 cm, the positron dE/dx deviant cut was relaxed to -3<σ<4, and the fraction of energy carried by the positron was required to be less than 75%. The spectra were created for two different r_{xy} conversion distance requirements to reveal systematic trends that might be caused by differences in the material layout of the real detector and that of the simulations which were used to calculate the efficiency corrections. The efficiency corrections for r_{xy}>10 cm, Figure 4.8, include vertex distribution dependent correction factors that compensate for the lack of material in the simulation between 10<r_{xy}<40 cm, refer to Section 4.2.2. The relaxed positron dE/dx deviant was used to calculate the yield of photons in different p_t and y bins. The positron daughter was chosen over the electron to reduce the counting of false photon candidates arising from hard scatterings of particles with electrons in the detector material, δ electrons. The fraction of energy carried by the positive particle was required to be more than 85% to remove contamination that still existed from δ electrons that were knocked out by positive particles (π, K, and p) with momenta in regions where their dE/dx bands cross the positron band. The dE/dx deviant was used instead of the dE/dx, because it is independent of the momentum of the positron and ultimately the p_t of the photon unlike dE/dx. This allowed for positrons of different momenta to be merged into photon p_t bins. The shape of the background in these dE/dx deviant distributions was studied with a sample of photon candidates that pass anti–photon cuts. The anti–photon cuts suppressed positrons from true photons by requiring the photon selection criteria to be loose and on the outskirts of the distributions, like the two track distances of closest approach to be

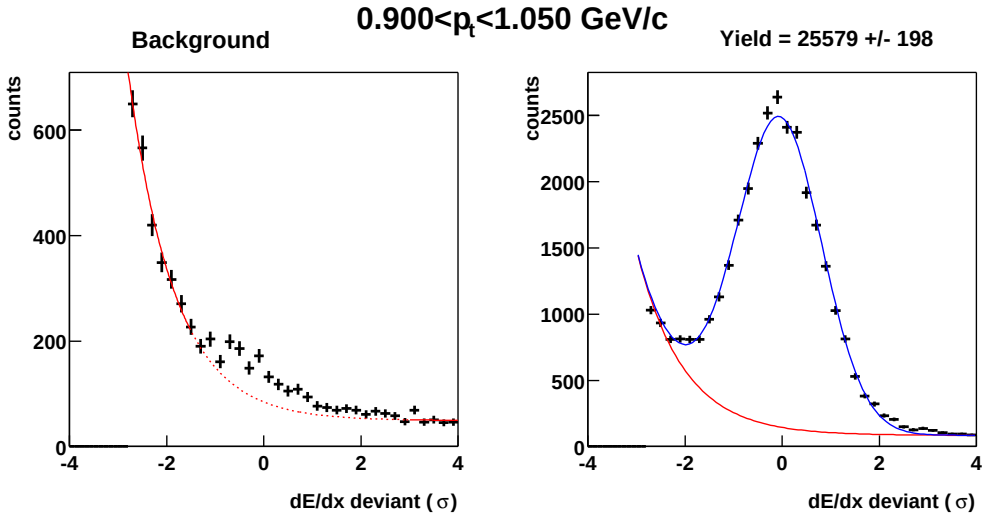

Figure 3.10: dE/dx deviant distributions for positive daughters of photon candidates. Left: The background distribution was mocked with positive tracks from a sample where true photons were suppressed with anti–photon cuts. Right: An example of a fit to the positron signal plus the background.

$1.5<|d_{xy}|<2$ cm and $1<|d_z|<1.5$ cm. A two parameter exponential plus linear function described these background distributions well. The parameters of the background functions were found by fitting these distributions with the region about zero removed, $1.5<\sigma<3$. This was necessary to avoid fitting the small enhancements from real photons that still existed after the anti–photon cuts were applied, as shown for one p_t bin in Figure 3.10. The positron dE/dx deviant distributions of photon candidates were fit with this parameterized background function, which had one free scaling parameter, and a three parameter Gaussian function.

Raw yields were extracted by summing bin contents weighted with the probability that a given entry is a positron. These weights were calculated by dividing the height of the Gaussian function part of the fit by the height of the entire fit at each bin center. For the photon y distributions, raw yields were extracted in a 4x10 array of p_t–y bins to properly account for the varying efficiency as a function of p_t. Three 0.25 GeV/c wide p_t bins were used below p_t=0.75 GeV/c where the efficiency grows rapidly, and one large bin was used where the efficiency is flat, $0.75<p_t<2.5$ GeV/c. Efficiency corrections, Figure 4.8, were applied to each p_t–y bin independently. The corrected y distributions of the various centrality classes, Figure 3.12, are flat around mid–rapidity. A systematic uncertainty of 7% has been assigned to the normalizations of the dN/dy spectra to account for uncertainties in the detection efficiency and potential biases that may arise from differences in the real and Geant material maps. The p_t dependence was measured in 0.15 GeV/c wide p_t bins. It was not necessary to divide into y bins, since both the shapes of the corrected y distributions and the input distributions of the efficiency corrections had the same functional form, flat. The raw yields and corrected p_t spectra for photons with $|y|<0.5$ are shown in Figures 3.11 and 3.12, respectively. The $r_{xy}>40$ cm spectra extend up to p_t=1.8 GeV/c.

The values in the lowest $r_{xy}>10$ cm p_t bins, $0<p_t<0.15$ GeV/c, are systematically 15-25% lower

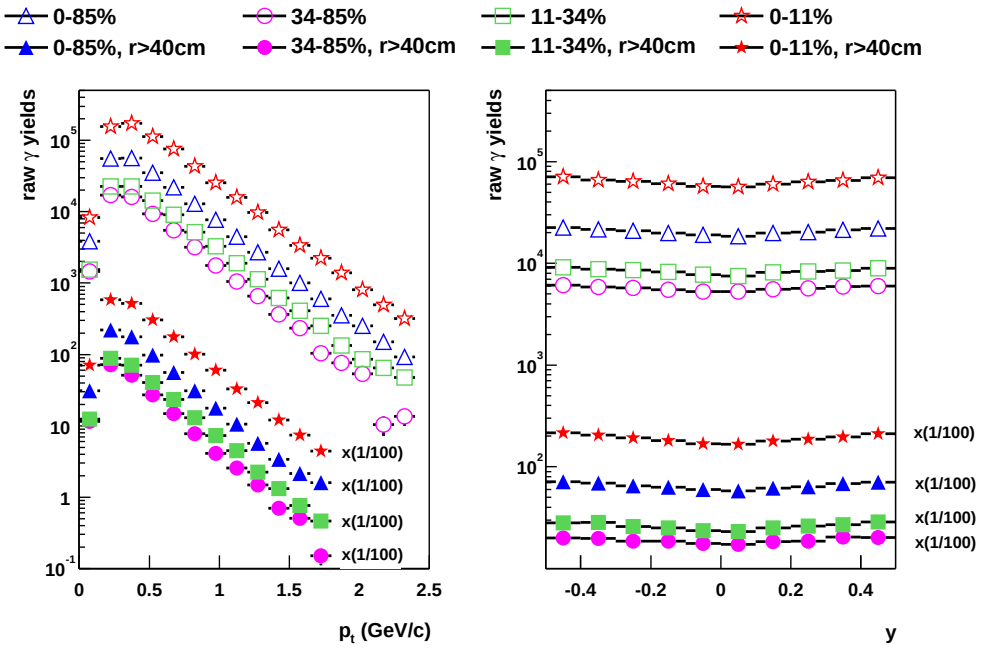

Figure 3.11: Raw yields of photons versus p_t (left) and y (right) for the different centrality bins. The open and closed symbols represent data from photon conversions in material with r_{xy}>10 cm and r_{xy}>40 cm, respectively. Multiplicative factors were applied to the data for r_{xy}>40 cm.

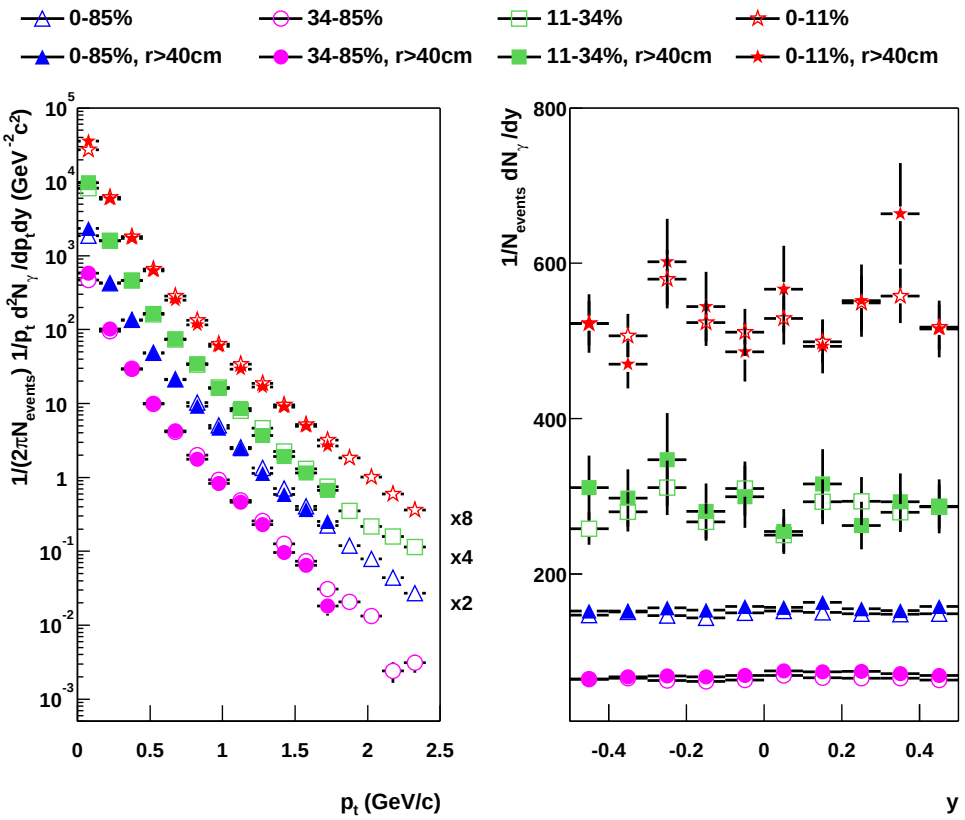

Figure 3.12: Corrected photon p_t (left) and y (right) spectra for ^{197}Au+^{197}Au collisions at $\sqrt{s_{\rm NN}}$ = 130 GeV. The p_t distributions are for mid-rapidity photons, |y|<0.5. The errors shown are only statistical. An additional 7% systematic uncertainty has been estimated on the normalization of the dN/dy spectra and point–to–point in the p_t spectra, as discussed in Section 4.2.4. Data points are provided in Appendix B.

than the corresponding r_{xy}>40 cm bins. This is attributed to the efficiency correction being under estimated in these bins for the r_{xy}>10 cm spectra, because the simulation lacks material between 10<r_{xy}<40 cm. This gives the inner field cage and TPC gas a larger fraction of the total conversion probability in the simulation, and results in a mean r_{xy} conversion point that is closer to the TPC. Relatively more conversions at larger r increase the relative probability that both tracks from a low p_t conversion are reconstructed and results in higher photon reconstruction efficiencies. Therefore, the inverse of these efficiencies, the corrections, will be too small. The material factors that compensate for the material differences only linearly scale the efficiencies, and do not account for the conversion probability as a function of r coupling to the acceptance. A 7% point–to–point systematic uncertainty was estimated for both the r_{xy}<10 cm and r_{xy}<40 cm spectra to account for uncertainties in the detection efficiency, as discussed in Section 4.2.4.

The purity of photon candidates was determined by dividing the integral of the Gaussian function by the integral of the total fit function between a positron dE/dx deviant of -2σ and 4σ. The purity

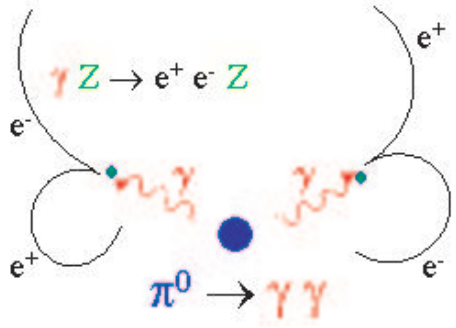

Figure 3.13: Pictorial diagram of $\pi^0 \rightarrow \gamma\gamma$ reconstruction. The invariant mass of photon pairs was used to identify two photon decays. The photons were reconstructed via the pair conversion technique.

below p_t=0.75 GeV/c is above 90% in all centrality bins. In the top 11% most central centrality bin, where the purity is the lowest, it drops linearly from about 90% at 0.75 GeV/c to about 60% at 2.4 GeV/c. The photon sample from conversions in the inner field cage and TPC gas, r_{xy}>40 cm, has a higher purity which is greater than 95% below 1 GeV/c.

3.3 Reconstruction of $\pi^0 \rightarrow \gamma\gamma$ Decays

In heavy ion collisions, the $\pi^0 \rightarrow \gamma\gamma$ decay is the dominant mechanism that produces photons. The π^0 mesons were detected by calculating the invariant mass of photon pairs. Individual decays cannot be uniquely identified, because of the combinatorial background in the two photon invariant mass distribution. The raw yields were extracted by fitting the enhancement in the two photon invariant mass distribution at the π^0 mass. The determination of the background shape and the fit to the invariant mass peak were done in separate steps. The background shape was found by fitting a 2nd order polynomial to the invariant mass distribution of photon pairs which had one of the photon's momentum vector *rotated* by π-radians in xy-plane. The *rotated* invariant mass distribution preserved event characteristics like the vertex position along the beam axis, multiplicity and anisotropic flow. The azimuthal symmetry of the STAR TPC couples with the rotation to maintain a consistent geometric acceptance and tracking efficiency as a function of azimuth. At the same time the rotation moves and smears the invariant mass peak of the pairs that are correlated through two photon decays. Raw yields of π^0s were obtained by fitting invariant mass distributions with a Gaussian function plus a parameterized background function which had a floating normalization, Equation 3.4 and Figure 3.14. The width, ~8 MeV/c^2, is dominated by the photon energy resolution and not the intrinsic mass width of the π^0, ~8 eV/c^2. For this reason a Breit-Wigner function which describes the intrinsic width of resonances was not chosen. Two fit iterations were performed to extract the yield of π^0s as a function of p_t. The first iteration had a total of four free parameters: the yield (N), mass (m) and width (σ) of the Gaussian function and the normalization of the background (B). The second pass of fits assumed that the invariant mass peak has a linearly increasing width with p_t, as seen in simulated data. The widths of the fits used in the second pass were obtained by fitting a linear function of p_t to the widths found in the first pass. The widths of the fits were fixed to the value of the linear function at the center of the p_t bin. This reduced the number of free parameters in the second pass to three and increased the stability of the fits.

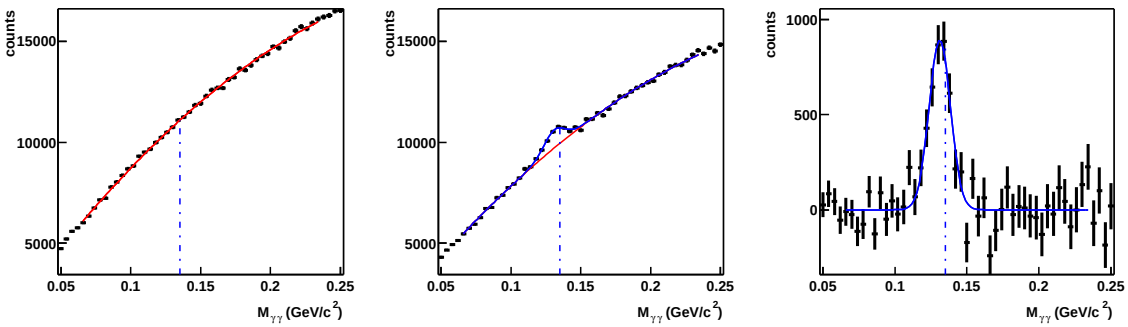

Figure 3.14: Two photon invariant mass distributions in ^{197}Au+^{197}Au collisions at $\sqrt{s_{\rm NN}} = 130$ GeV. Left: The mocked combinatoric background shape of the invariant mass distribution was produced by rotating one photon by π-radians and is well described with a second order polynomial (red line). Middle: The invariant mass distribution of photon pairs is fit with a Gaussian function, to describe the enhancement from the $\pi^0 \rightarrow \gamma\gamma$ decay, plus the parameterized second order polynomial with a floating normalization (blue). Right: The $\pi^0 \rightarrow \gamma\gamma$ peak is most apparent after the predicted combinatoric background has been subtracted. The vertical dashed lines indicate the location of the π^0 mass, 0.135 GeV/c^2 [Gro00]. The few MeV/c^2 deviation from the π^0 mass is attributed to the energy loss experienced by the two electrons and two positrons in the detector material.

$$M_{\gamma\gamma}(x) = \frac{N\delta}{\sigma\sqrt{2\pi}} e^{(x-m)^2/(2\sigma^2)} + B\left(a + bx + cx^2\right), \tag{3.4}$$

where N is the number in the Gassian peak and B is the scale factor of the background function.

Two features of the data are a few MeV/c^2 mass deviation from the expected location of the π^0 invariant mass peak and a narrower peak width in central events when compared to minimum bias. Both of these features are artifacts of energy loss experienced by the electrons and positrons in the detector material. The tracking routine for "global tracks" only compensated for energy lost in the gas and not in other detector material. The reconstructed momentum of electrons and positrons that originate prior to the gas is systematically lower than their original momentum. This small, $\sim$1 MeV/c on average, effect is apparent in the π^0 invariant mass peak, because the sum of the effect on four particles becomes a few MeV/c^2. This conclusion was confirmed with two checks on simulated π^0s. The reconstructed invariant mass peak for simulated π^0s systematically decreased as the distance between the primary vertex and conversion point of the closer photon decreased. This implied that a larger π^0 mass deviation occurred when the amount of detector material increased between the conversion point and TPC. Simulations also showed a systematic shift in the reconstructed photon energy as a function of the radial conversion point, expressing a similar conclusion. The wider width of the π^0 peak in the minimum bias data than in the central sample is attributed to a wider spread in the z vertex position of the minimum bias data. The amount of material that the particles traverse varied more in the minimum bias sample leading to a larger deviation in the amount of energy lost by particles and ultimately a wider invariant mass peak.

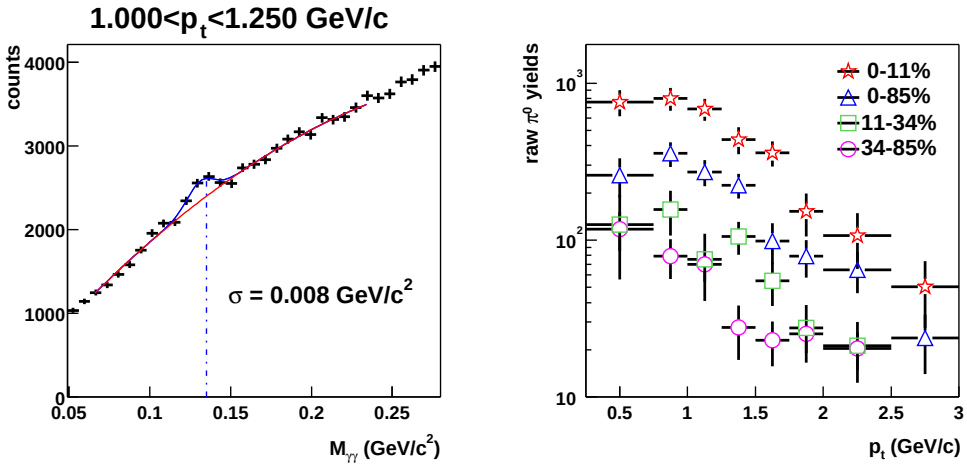

Figure 3.15: Left: Fit to the invariant mass enhancement at the π^0 mass raw for $1<p_t<1.25$ GeV/c in the top 11% centrality bin. Right: The extracted mid-rapidity, $|y|<1$, raw yields for as a function of p_t for 0-85% (blue triangles), 34%-85% (pink circles), 34%-11% (green boxes) and top 11% (red stars) event centrality classes.

3.3.1 π^0 Spectra

The raw yields of π^0s about mid-rapidity, $|y|<1$, were extracted in various p_t bins for four different centrality classes, as shown in Figure 3.15. These centrality classes were chosen based on an ability to extract π^0 yields over a wide range of p_t, $0.25<p_t<3$ GeV/c, in independent regions of centrality. An inclusive minimum bias (0-85%), peripheral (34%-85%), mid central (34%-11%) and central top 11% were the selected centrality classes, as defined in Table 3.1. The minimum bias, peripheral and mid-central centrality classes were composed of data taken with the minimum bias trigger. These classes did not include central triggered data to avoid a bias towards higher multiplicity events. The top 11% centrality class was composed of events from both the minimum bias triggered and central triggered data. Using the central trigger data in this data set causes less than a 4% bias towards the lower multiplicity side, as discussed in Section 2.5. These selected event classes (minimum bias, peripheral, mid-central, top 11% central) contained 328980, 198196, 87484, 449095 events, respectively. The narrow 8 MeV/c^2 width of the enhancement at the π^0 mass, Figure 3.15, compares to a 20 MeV/c^2 sigma of a conventional calorimeter. This narrow width is a result of the good photon energy resolution, 3% at 1 GeV, obtained with the presented method of reconstructing photons. The narrow width improves the signal to background ratio and enables the extraction of raw π^0 yields at low p_t, $p_t<0.75$ GeV/c, where the signal to background ratio is penalized by a large combinatoric background.

Corrected p_t spectra of the π^0s were obtained by applying centrality dependent efficiency corrections, described in Section 4.3.2, to the p_t distributions of the raw yields. These corrected spectra are plotted in Figure 3.18 and the data points are provided in Appendix C. The error bars shown on the yields are purely statistical and combined both the errors in the raw yields and efficiency correction. These errors mainly reflect the low number of real π^0s measured. All track, photon and π^0 cuts were varied to study the systematic uncertainties of the cuts. These studies revealed that the statistical fluctuations dominated over these systematic trends and resulted in the knowledge

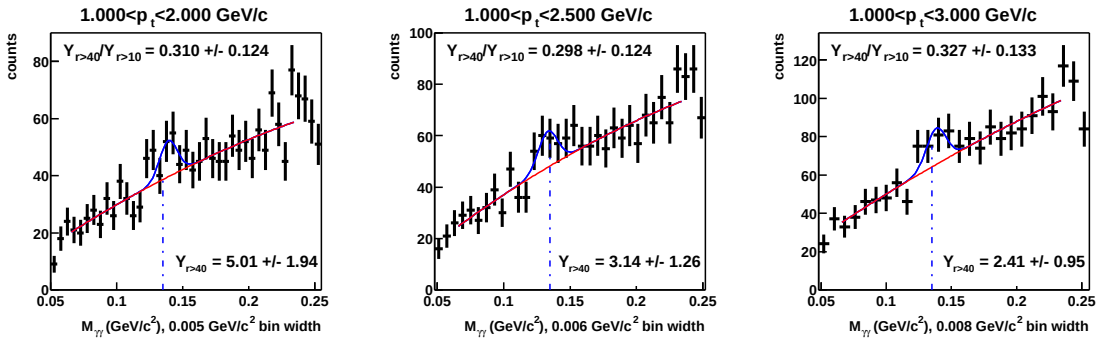

Figure 3.16: Fits to the π^0 peaks in the two photon invariant mass distribution for photons with r_{xy}>40 cm from the 0-85% centrality bin. The three plots correspond to different p_t windows and invariant mass bin widths. The $Y^{min}_{r>40}$ in the plots are the corrected yields for the given p_t ranges, but are not weighted for the efficiency within the bin coupling with exponentially falling shape of the spectrum. The $Y_{r>40}/Y_{r>10}$ ratios are the extracted material correction factors.

that the statistical errors outweigh these systematical uncertainties. Corrections to the normalization were made to compensate for differences between the material map of the physical environment and that in the Geant simulation, as discussed in Section 4.2.2. These corrections were obtained by calculating the corrected yield of π^0s for photons that convert in the inner field cage or TPC gas (r_{xy}>40 cm), where the material maps are consistent with each other. The shape of the efficiency for reconstructing π^0 from photons with r_{xy}> 40 cm was compared to that for photons with r_{xy}>10 cm. Above 1 GeV/c, the ratio of these efficiencies is flat. With a flat ratio, the yields within different selected r_{xy} regions can be divided without compensating for the influence on the yields from interplay between the shape of the efficiency and the exponentially falling spectrum. This ratio is not flat over the full range of p_t, because the acceptance of low p_t tracks does not penalize the photon reconstruction efficiency, when conversions are required to have a r_{xy}>40 cm. A material correction factor, which is independent of centrality and the p_t interval, was obtained by dividing the corrected yield$_{r>40}$ by the yield$_{r>10}$. This material correction factor was cross checked in three different p_t windows, as shown in Figure 3.16. The variation between the p_t window was found to be much (5×) smaller than the uncertainty in the individual ratios. The ability to fit a low number, ∼50 counts, of reconstructed π^0s from photons with r_{xy}>40 cm mainly determined this large uncertainty (∼40%) in the ratios. The stability of the fits was checked by comparing the results for different invariant mass bin widths. This confirmed that the statistical uncertainties in the raw yield$_{r>40}$ dominated. The minimum bias data set was used to extract the material correction factor, 0.310 ±0.124 choosing 1<p_t<2 GeV/c. This factor was applied to the normalization of centrality classes that stemmed from random subsets of the minimum bias triggered data (0-85%, 34%-85%, 34%-11%). The uncertainty in this factor (±0.124 or 40%) is common between the centrality bins, in the sense that all the spectra move together and the uncertainty will cancel in ratios taken between them. This factor could not be used to normalize the top 11% centrality bin, because of differing z vertex distributions between central and minimum bias triggered data.

The corrected yield of the minimum bias centrality class, Y^{min}=5.01±1.94 for 1<p_t<2 GeV/c, was used to calculate a material map factor for $|z_{vertex}|$<75 cm. In this range the vertex distribution of events for the two triggers were similar and the common factor was applied to subsets of one combined data set. The factor was calculated by taking the ratio of Y^{min} to $Y^{min}_{|z_{ver}|<75}$ with the

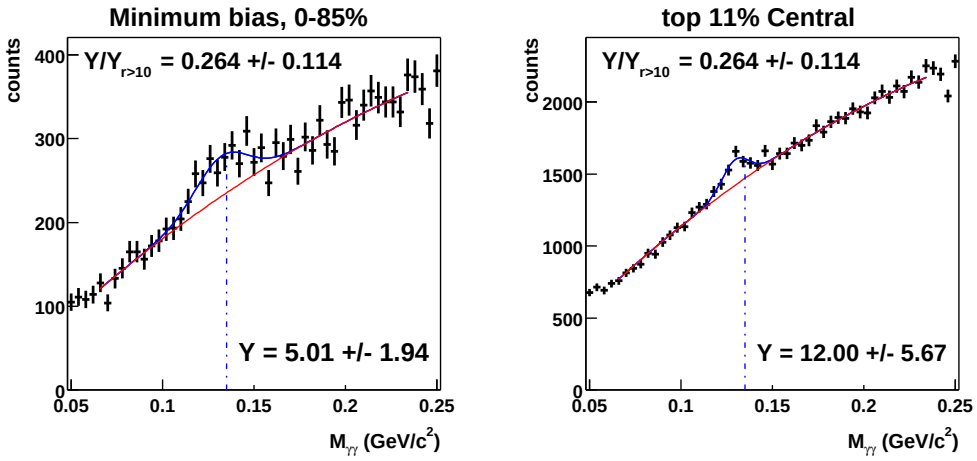

Figure 3.17: Fits to the π^0 peaks in the two photon invariant mass distribution for events with $|z_{vertex}|$<75 cm. The "Y"s are the corrected yields between 1<p_t<2 GeV/c for the indicated centrality bins. The identical $Y/Y_{r>10}$ numbers are independent of centrality and were obtained with the minimum bias centrality bin.

vertex constraint, as shown in Figure 3.17. With this factor, 0.264±0.114, the normalized yield for the top 11% centrality bin was computed by taking the product of the factor and $Y^{cent}_{|z_{ver}|<75}$. This normalized yield, Y^{cent}=12.00±5.67 for 1<p_t<2, is independent of vertex distributions. The final top 11% spectrum was scaled by $Y^{cent}/Y^{cent}_{|z_{ver}|<150}$, 0.274±0.135. In summary, the top 11% central class also has the same common uncertainty of ±40% and an additional uncertainty of ±19%. These two uncertainties can be combined (±49%) for comparisons to other spectra, like the spectrum of negative hadrons.

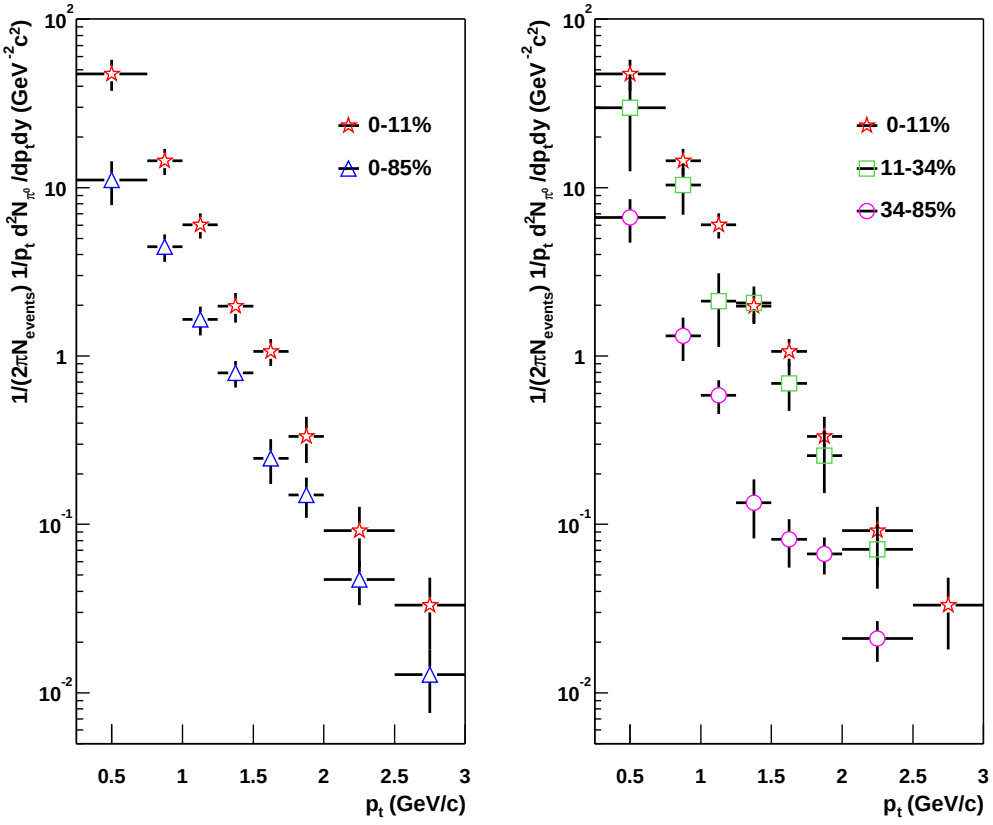

Figure 3.18: π^0 spectra about mid-rapidity, |y|<1, for different centrality bins. The 0-85% (blue triangles) and top 11% (red stars) spectra are shown in the left plot. The 34%-85% (pink circles), 34%-11% (green boxes) and top 11% (red stars) are shown together in the right plot. The error bars shown are purely statistical. Along with the point–to–point statistical errors, all spectra have a common uncertainty in the normalization of ±40%. The central data has an additional uncertainty in the normalization of ±19% arising from a differing distribution of the event vertex positions, or a total uncertainty that sums to ±49%. The centrality definitions are given in Table 3.1 and data points are provided in Appendix C.

Chapter 4

Monte Carlo Studies and Efficiency Corrections

Monte Carlo studies were performed to determine the resolution of kinematic parameters and the reconstruction efficiency of both single photons and π^0s. The simulation software consisted of a particle generator, a particle propagator that incorporated the complete detector geometry, and a detector response simulator that mocked the electron drift and TPC electronics. A realistic event environment was established by embedding the simulated pad signals into real events. These combined events used the same event and track reconstruction code as the real events. Finally, an association process linked reconstructed and simulated particles. Resolution and efficiency studies where then performed on these associated particles.

4.1 Particle Generation and Propagation

Particle distributions were generated uniformly in transverse momentum (p_t) and rapidity (y). Photons were generated with p_t<3.2 GeV/c and $|y|$<2; while the π^0s were generated with a p_t<3.2 GeV/c and $|y|$<1.2. The kinematics of π^0 decays were simulated with Geant 3.21/13 [gea93]. Interactions of the particles with detector material were also simulated using Geant. In order to minimize the effects that arise from embedding too many tracks into one event, a selection within Geant filtered out the daughters from π^0s that could not be detected. This was especially important with such a low detection efficiency ($\sim 10^{-4}$), where an average of 400 other electron and positron tracks are created for every detectable π^0. A $\pi^0 \rightarrow \gamma\gamma$ decay was considered detectable if both photons underwent an interaction that produced at least one daughter within the STAR acceptance. The complete Geant information, like decay kinematics and material interactions, was saved for detectable π^0s and their daughter particles. The three–vector momentum of all generated π^0s was stored in a text file.

4.1.1 TPC Response Simulator

The ionization produced by charged tracks traversing the TPC gas was passed through a TPC Response Simulator (TRS). TRS simulates the TPC response from the drift of the ionization in the TPC gas to the output of the front–end electronics. It includes the drift, diffusion, amplification and response of the electronics for the electrons created by ionization in the TPC gas. Simulated pad signals from TRS could be reconstructed standalone or embedded into real events.

Association Cut	Description
$\left\|E_{rec} - E_{mc}\right\| / E_{mc} < 25\%$	Relative Energy Difference
$\left\|\lambda_{rec} - \lambda_{mc}\right\| < 0.3$	Dip Angle Difference
$\left\|\phi_{rec} - \phi_{mc}\right\| < 0.4$	Phi Angle Difference

Table 4.1: Association cuts between the kinematic parameters of reconstructed and embedded photons.

4.1.2 Embedding, Event Reconstruction and Association

Embedding was accomplished by adding the pad signals of a simulated event to those of a real event, pixel–by–pixel. The hit and track reconstruction software was then used to reconstruct the combined events. After reconstruction, the primary vertex was reset to that of the real event. For both photon and π^0 embedding, simulated photon conversions were found with the photon–finding algorithm that was used on real data. The electron and positron dE/dx cuts were not used, because of known differences and offsets between the real and simulated dE/dx. Corrections for particles lost via dE/dx cuts were included separately into the efficiency calculation. The original event vertex was preserved to remove any potential bias that the simulated tracks might have on its position.

Simulated photons were extracted from the reconstructed photon sample with a set of association criteria that compared the input and reconstructed parameters of photons. Three parallel kinematic cuts were used to match embedded and reconstructed photons. These association cuts were on the relative energy ($\Delta E/E$), dip angle difference ($\Delta\lambda$) and phi angle difference ($\Delta\phi$). The association requirements are given in Table 4.1. The association parameters of all reconstructed photons were compared to those of every simulated photon that experienced an interaction which produced at least one daughter within the TPC acceptance. These association requirements removed photon candidates that preexisted in the real events.

Events with embedded photons and not π^0s were used to determine the values of association cuts and optimize the association efficiency. Photons from $\pi^0 \rightarrow \gamma\gamma$ decays were not used, because decay correlations between the two photons make false associations more probable. The association efficiency of each cut was extracted by fitting distributions of each quantity while the other two constraints were imposed. Examples of fits to the distributions for both minimum bias and central events are shown in Figure 4.1. The sum of two Gaussian functions was chosen to simultaneously describe both the narrow and broad peaks in the distributions. A linear background function was used to describe the shape of the background in the relative energy distribution. A uniform background was assumed in the distributions of the dip angle difference and phi angle difference. An estimate of the fraction of associations retained by each cut was obtained by dividing the integral of two Gaussians over the accepted range by the integral of the two Gaussians over twice the accepted range, $>10\sigma$.

The total association efficiency –the probability of matching a reconstructed photon with the corresponding input Monte Carlo photon– was obtained by taking the product of the three, individually retained fractions. The total association efficiency was found to be greater than 99% for p_t<2.5 GeV/c. The fraction of false associations was estimated by dividing the integral of the background function by the integral of the entire fit over the accepted range. This fraction was found to be less than 2% in a minimum bias event sample and less than 3.5% for photons embedded into the top 11% most central events, in all p_t slices. The association criteria were tuned to maximize association efficiency while minimizing the fraction of false associations. The optimization of the efficiency is especially important for the $\pi^0 \rightarrow \gamma\gamma$ analysis, because the π^0 association efficiency is roughly

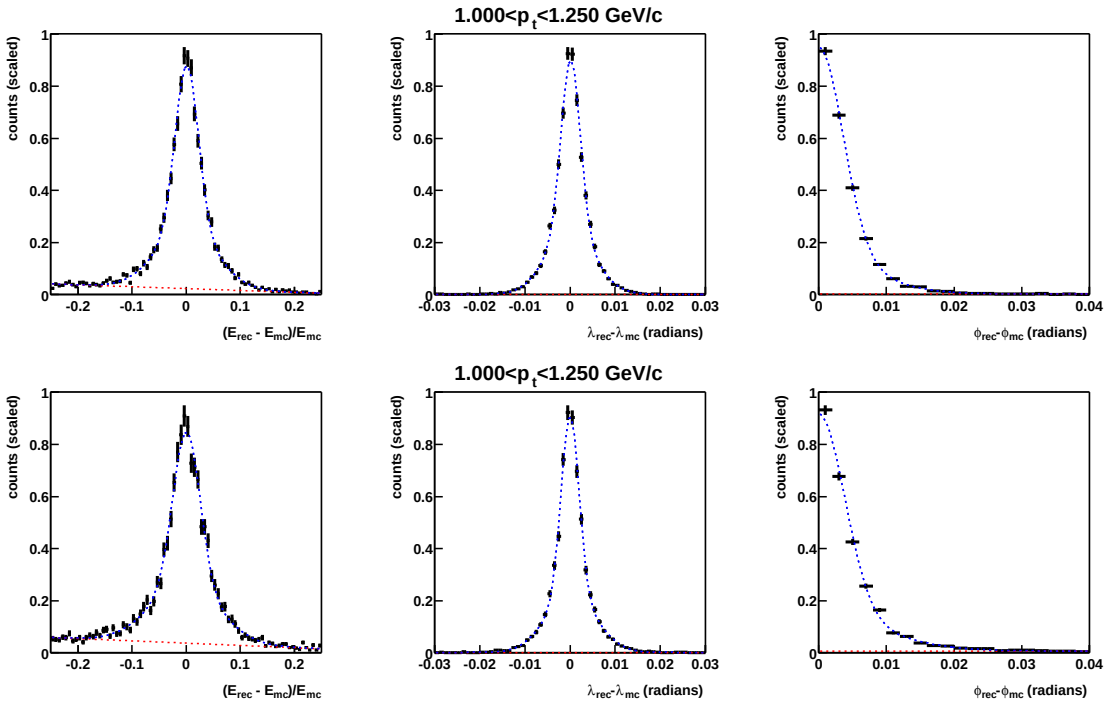

Figure 4.1: Differences between the kinematic parameters of reconstructed and generated photons. The top and bottom set of plots reflect the distributions for simulated photons that were embedded into minimum bias events and events from the top 11% centrality class, respectively. The lines illustrate the fits to the distributions (blue) and the predicted background (red) from false associations.

the square of the single–photon association efficiency. The small fraction of false associations is accounted for in the corrected photon spectra. False associations do not disturb the $\pi^0 \to \gamma\gamma$ analysis, because the invariant mass of a false association combined with a generated photon or another false association is part of a small harmless combinatoric background in the invariant mass distribution. Therefore, this does not add to the measured enhancement at the π^0 mass from generated $\pi^0 \to \gamma\gamma$ decays. The probability that a real $\pi^0 \to \gamma\gamma$ decay enters into the Monte Carlo π^0 sample after association is negligible.

4.2 Photon Embedding Studies

The momentum and angular resolution of photons, and the photon –finding efficiency were calculated using embedded events. Photons in these events also served as a valuable tool for producing essentially background free distributions of the variables used to select photons. 2000 simulated photons were introduced into each real event. Of these, an average of 20 convert, as a consequence of the low conversion probability in detector material ($\sim$1%). As a result, an average of 40 tracks are added to each event. The number of photons generated was chosen so that the original real event environment was not disturbed. Over–embedding would result in an increased probability that clusters overlap and merge, which reduces the tracking efficiency and worsens kinematic resolutions. In the most central events, where over–embedding is the most sensitive, the embedded tracks composed less than 2% of the total number of reconstructed tracks in the embedded phase space. Therefore, the number of photons embedded had a negligible effect on the track reconstruction efficiency.

4.2.1 Photon Kinematic Parameter Resolutions

Resolutions of kinematic parameters were estimated by comparing the input and reconstructed quantities. These estimates were extracted through single Gaussian fits to distributions of percentage differences or absolute differences. As discussed in section 4.1.2, the distributions are better described by the sum of two Gaussians, but for the purpose of quoting a standard resolution in terms of a single Gaussian width, σ, the peaks were fit with single Gaussian functions.

Resolutions were calculated for photons with p_t<2.5 GeV/c and |y|<1. The energy resolution as a function of photon energy was obtained by fitting the percentage difference in 0.25 GeV wide energy slices. A contour plot of the energy resolution as a function of energy and the Gaussian fit to one energy bin are shown in Figure 4.2. The p_t, dip angle and phi angle resolutions were extracted in the same manner, but as a function of p_t. The values of these resolutions are plotted versus energy or p_t in Figure 4.3. The estimated p_t resolution for photons in a minimum bias sample of events rises linearly from $\sim$2% at 0.125 GeV/c to $\sim$5% at 2.5 GeV/c. It is systematically worse, by $\sim$0.25%, for events of the top 11% centrality class. This is attributed to the higher hit and track density of central events that increases the probability that a hit from one track merges with a hit from another track. This ultimately results in poorer position resolution of hits and the loss of hits on tracks.

4.2.2 Real Environment versus the Geant Material map

The conversion probability in material of density (ρ), length (l) and atomic number (Z) is to first order proportional to $\rho l Z^2$. A map of the ρZ^2 distribution of the detector material was produced by plotting the density of photon conversion points. The layout of the TPC and SVT are apparent in the conversion density plots shown in Figure 4.4. The conversion point density in the xy-plane illustrates the location of the inner field cage, the SVT support rods that run between the support

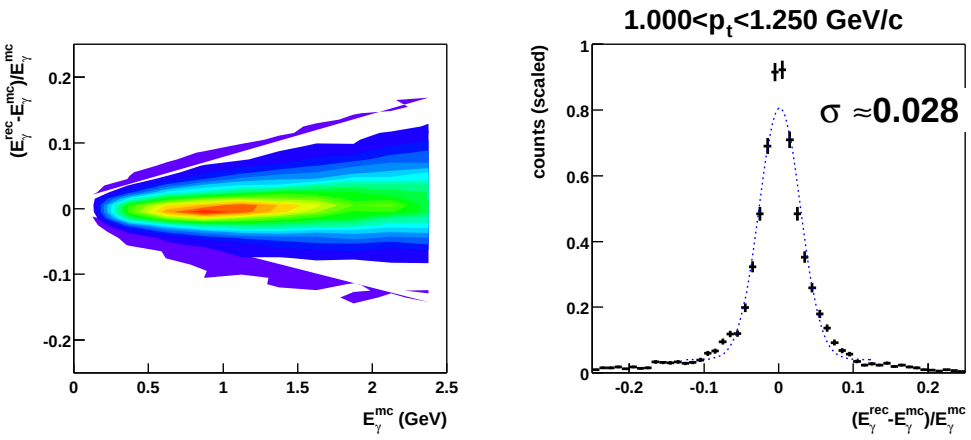

Figure 4.2: Left: reconstructed energy resolution of photons as a function of the generated photon's energy. Right: Projections, 0.25 GeV/c wide, of the distribution were fit with Gaussian functions to obtain a measure of the energy resolution as a function of energy.

cones, and the one silicon ladder that was in place for the year 2000 run. The geometry of the SVT support cones is revealed in the projection onto the rz-plane. The precision of the secondary vertex positions and the purity of the photon sample illuminate fine details of the detector. Among these fine details are the glue joints and foam strip on the inner field cage, and the wire layout on the SVT cones. The locations of the glue joints are not symmetric about z=0, but have a systematic shift of -1.8 cm. Physics results are independent of this observation, though it does display the sensitivity and accuracy of this technique.

The pictures of both the real and Geant environment provided insight on differences between the geometries. The material map in Geant was improved to better describe the true detector geometry, though noticeable differences still exist. Fortunately, the composition and density of the TPC gas are accurately known. The conversion probability in gas was used as a reference point between the real and Geant environments. Conversions in the gas, with $55<r_{xy}<100$ cm, were used to linearly scale the conversion probability in Geant to that of the real environment. After the scaling, the consistency between the real and Geant material map of detector components could be verified. It was found that the inner field cage of the TPC is described well in Geant, but the wiring and support material of the SVT was underestimated by a factor that depends on the z position of the material, as shown in Figure 4.5. On average, this factor was found to be $\approx$0.60. Both the calculated photon and π^0 efficiencies were corrected for this lack of material in Geant with overall scale factors, as discussed in Sections 4.2.3 and 3.3.1 respectively.

4.2.3 Photon Detection Efficiency

The conversion probability, acceptance, tracking efficiency and photon–finding efficiency were combined to form a single–photon detection efficiency. The detection efficiency was calculated by dividing the number of associated photons by the number of photons generated in Geant. The photon reconstruction efficiency –the probability that a photon which converts before or in the TPC gas is detected– was calculated by removing the conversion probability and selecting only photons that pair converted with $r_{xy}<200$ cm. These efficiencies were calculated for photons found with the

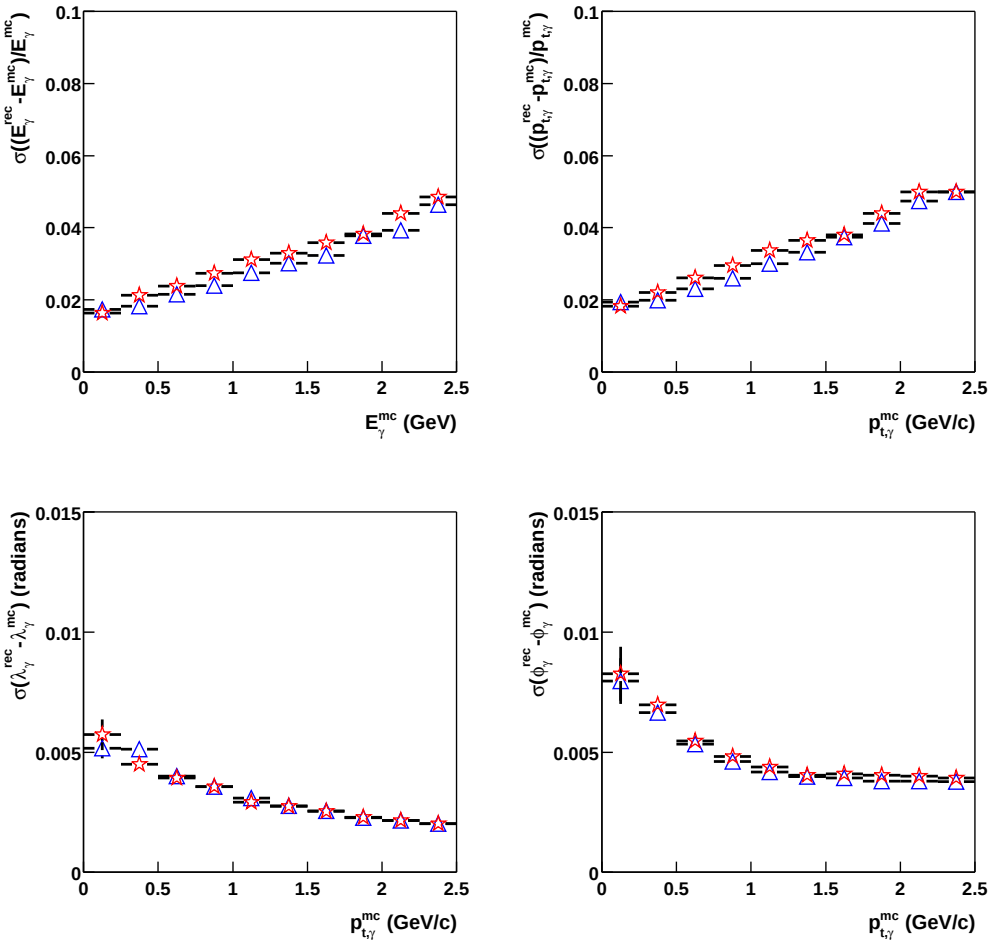

Figure 4.3: Energy, p_t, dip angle and ϕ resolutions of photons estimated with embedded photons. The stars represent resolutions for photons embedded into the central event environment, while the triangles are for minimum bias events.

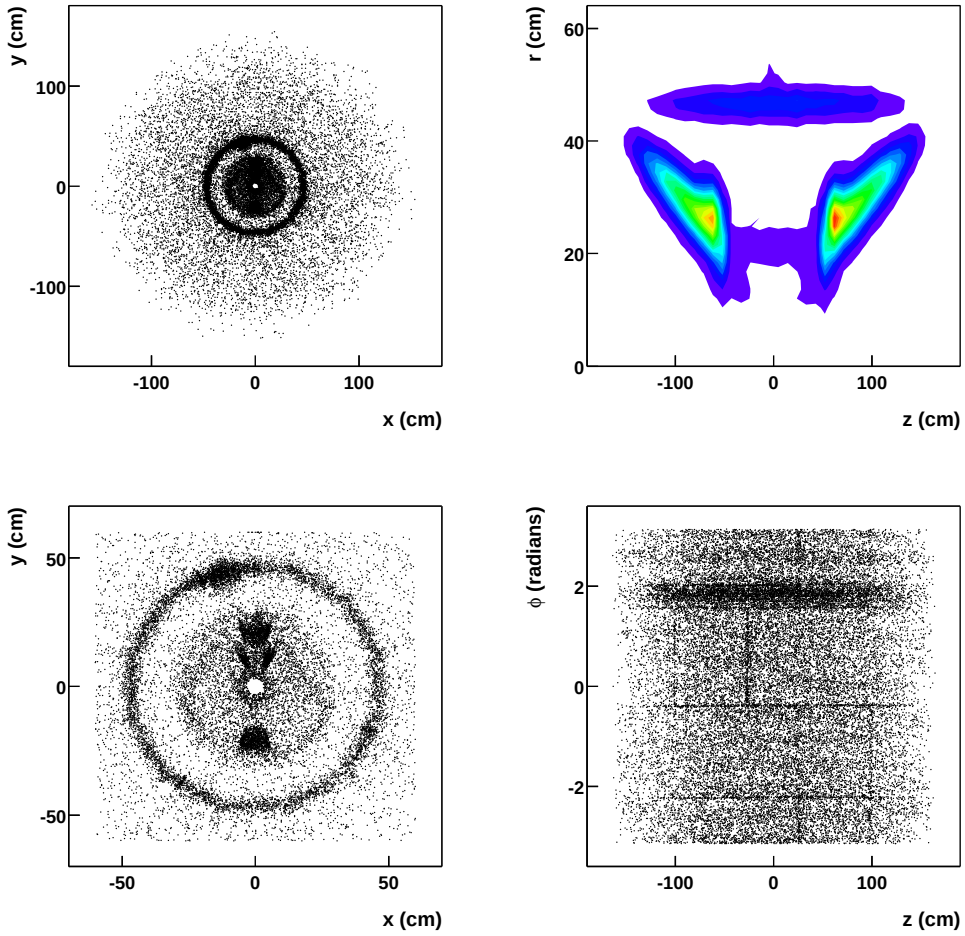

Figure 4.4: Density profiles of photon conversion points. Top figures: Global pictures of the STAR environment which reveal the locations of the inner field cage of the TPC (r_{xy}=46.5 cm) and the SVT material (r_{xy}<40). More details are seen in the bottom two plots where the inner part of the STAR detector is expanded (left) for |z|<15 cm and the inner field cage is unrolled (right). Bottom Left: The location of the support rods, near (x=0,y=±20), between the SVT cones and the material related to the one silicon ladder, near (x=0,y=10), are apparent. Bottom Right: The fine vertical and horizontal lines disclose the glue joints of the inner field cage, while the thick structure along z at ϕ=1.8 radians is the foam structure in which the field cage resisters were inserted.

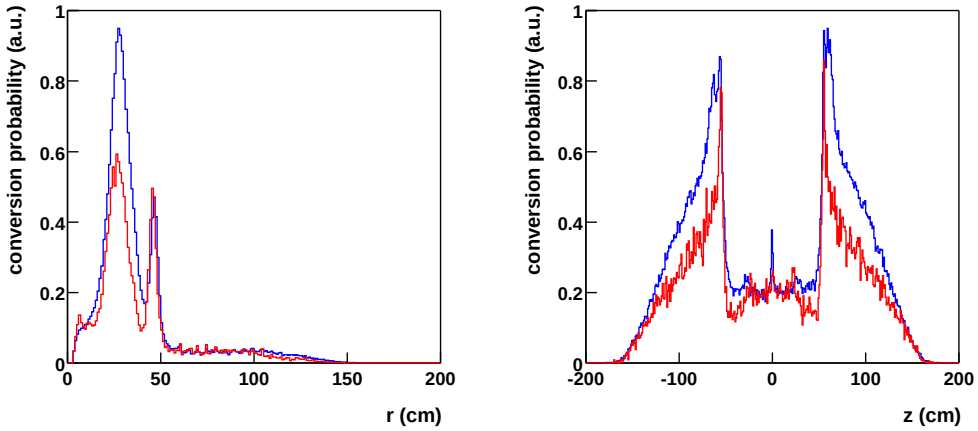

Figure 4.5: Conversion probability versus the radial distance from the beam axis (left) and z (right). A clean photon sample, measured to be >95% pure, was used to compare the conversion probability of the real event environment (blue) with that of the simulated environment in Geant (red). The similar conversion probability of conversions above r_{xy}>40 cm indicates that the material of the inner field cage, near r=46.5 cm, is described well in Geant. The higher conversion probability in the SVT support structure, 15<r_{xy}<40 cm, of the real data than in the Geant simulation suggests that material is missing in the Geant simulation. The right plot shows that the missing material is predominantly in the support structure of the SVT, |z|>25 cm.

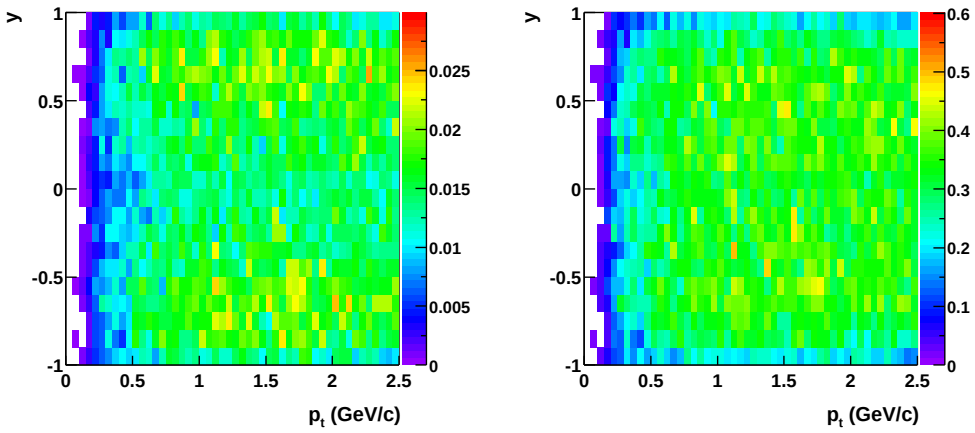

Figure 4.6: Detection (left) and reconstruction (right) efficiencies for photons detected via pair conversion with the STAR TPC. These plots represents the efficiencies for photons reconstructed under the standard photon cuts (Table 3.2) for minimum bias events with a $|z_{vertex}|$<75 cm.

standard photon cuts (see Table 3.2) in events with a $|z_{vertex}|$<75 cm. The p_t and y dependence of these efficiencies are shown in Figure 4.6. A factor of 1.42 was included in the detection efficiency calculation to compensate for differences between the material map used in the simulation and that of the real environment. This factor was obtained for events with a $|z_{vertex}|$<75 cm by scaling the overall conversion probability in the TPC gas of simulated events to that of real events, and then dividing the conversion probability in all material (r_{xy}>10 cm) of the real events by that of the simulated events. Both efficiencies were also scaled by a 95.5% to account for the loss of photons arising from the electron and positron dE/dx cut, -2σ<dE/dx<4σ.

The p_t dependence of the detection and reconstruction efficiencies was derived for an input distribution uniform in y that was integrated between -1<y<1, while the y dependence was extracted by integrating an input distribution uniform in p_t between 0–2.5 GeV/c. These efficiencies are shown for both minimum bias events and central events in Figure 4.7. At low p_t, the efficiencies are penalized by asymmetric conversions that have a daughter with a p_t of less then 0.075 GeV/c. The STAR magnetic field constrains low p_t daughters to tight spirals that in some cases do not reach the tracking volume or do not cross a sufficient number of pad rows to be reconstructed and pass the track–quality cuts. Inefficiencies from these features stabilize above a photon p_t of 1 GeV/c. The values of the detection and reconstruction efficiencies in these plateau regions are ∼1.5% and ∼32%, respectively, for minimum bias events and ∼1.2% and ∼24%, respectively, for central events. The lower efficiency of central events is caused by a lower tracking efficiency in a denser hit environment. The reconstruction efficiency of central events also has a more pronounced depression at mid–rapidity. This depression is attributed to the fact that on average hits from mid–rapidity tracks have a longer drift length and higher probability to merge with hits from other tracks. A larger diffusion results from a longer drift length, causing clusters to be broader. These broader clusters are more likely to overlap with other clusters and be reconstructed as a single hit. This reasoning is consistent with the effect being less for minimum bias events. On average, minimum bias events have a lower hit density, and therefore, are less sensitive to effects that result from cluster broadening. With the addition of the conversion probability in the detection efficiency, the depression is enhanced for both

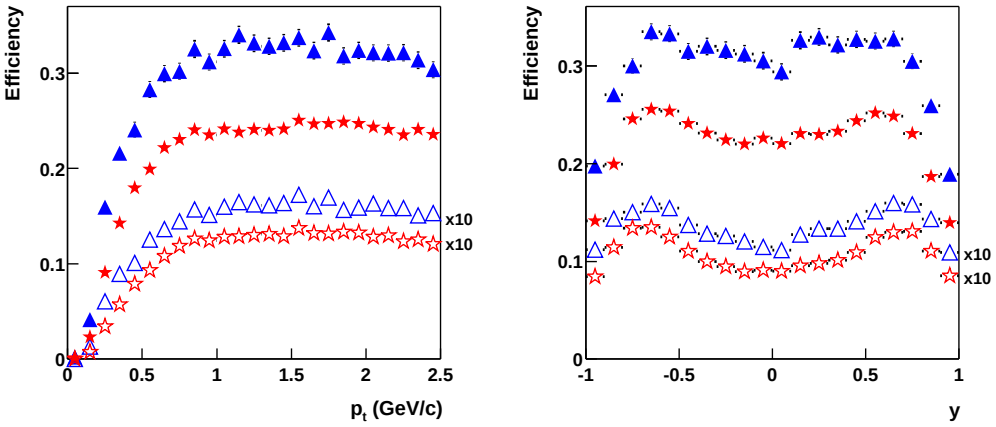

Figure 4.7: Photon detection efficiencies (hollow and scaled by a factor of 10) and reconstruction efficiencies (solid) as a function of p_t (left) and y (right). The triangles correspond to the efficiencies for minimum bias events and stars are for events of in the top 11% centrality class.

central and minimum bias events. This is attributed to the conversion probability itself being on average higher at larger rapidities, because of the longer path length through the detector material that for the most part runs parallel to the beam axis.

Centrality–dependent detection efficiencies, Figure 4.8, were also calculated to correct the raw photon spectra presented in Figure 3.11. These efficiencies were calculated for both photons that convert with r_{xy}>10 cm and r_{xy}>40 cm under the criteria given in Section 3.2.6. The minimum bias, 11–34% and 34%–85% centrality–class efficiencies for r_{xy}>10 cm include a material correction factor of 1.40 to compensate for the reduced conversion probability in the simulation when compared to real events. The differing primary vertex distributions between the minimum bias triggered and central triggered data sets made it necessary to extract a separate correction factor (1.42) for the top 11% centrality class. All these efficiencies have been scaled by 0.977 to account for the loss of electrons due to the dE/dx cut, -2<$\sigma^{e^-}_{deviant}$<4.

4.2.4 Comparisons of Distributions from Embedded Photons and Real Data

The distributions of track parameters used in the photon–finding algorithm were compared between embedded photons and those found in real events. The comparisons were used to check that the differences that exist do not introduce instabilities in the single–photon and π^0 detection efficiencies. At the track level, the following distributions were compared: the sdca, the number of hits included in a track's fit (nhitf) and the fraction of nhitf to the number of possible hits. These distributions were plotted for slices of p_t, as shown for one p_t slice in Figure 4.9. Differences arising from inconsistent rapidity distributions of real and simulated events were suppressed by limiting the photons to a region were both distributions are believed to be flat, |y|<1. The real and Monte Carlo distributions are similar and, more importantly, they do not show substantial differences in regions near or outside of where photon–finding cuts are applied.

Pair–cut distributions of real events and Monte Carlo simulations are compared in photon p_t

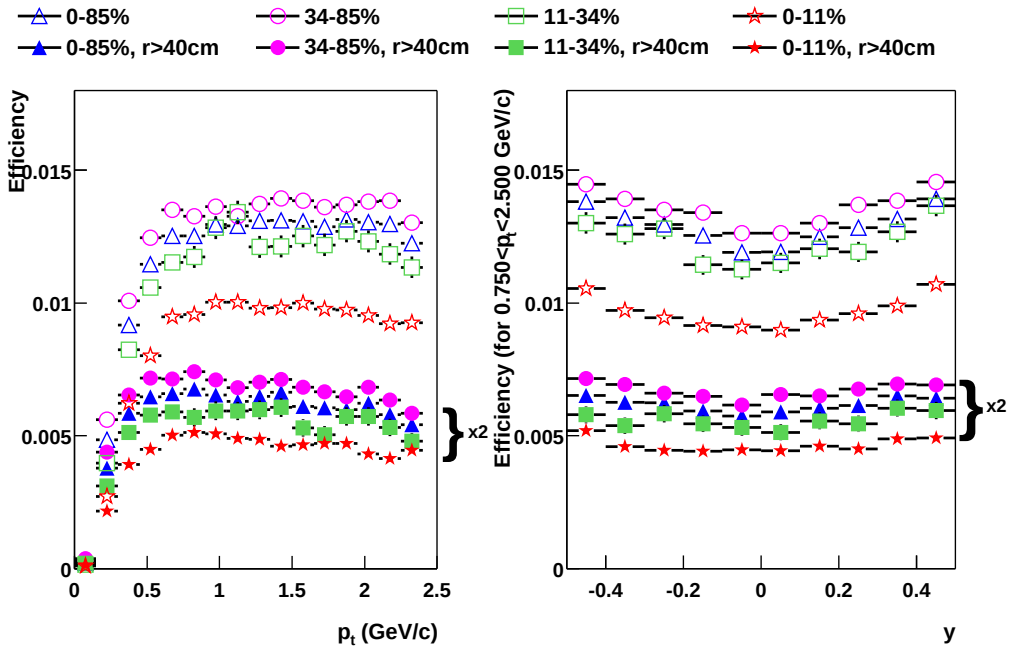

Figure 4.8: Detection efficiencies for four centrality classes as a function of p_t (left) and y (right). Open symbols represent the corrections for conversions that occur in material further than 10 cm from the beam axis, while the filled symbols are for conversions further than 40 cm and are scaled by a factor of 2. These efficiencies were calculated under the criteria given in Section 3.2.6.

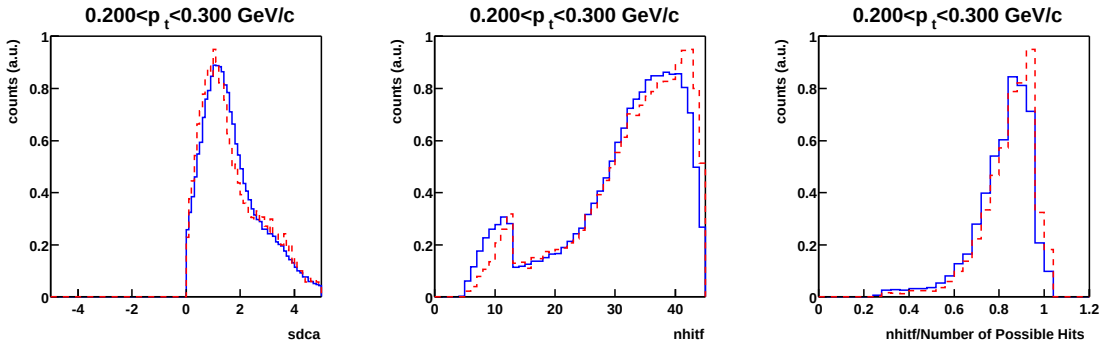

Figure 4.9: Track level distributions are compared between real photon candidates (blue) and simulated photons (red). The sdca, nhitf and ratio of nhitf to possible points are shown in the left, middle and right plots respectively. The plots help justify the stability in the photon reconstruction efficiency under slight variations of the photon–finding cuts, Table 3.2.

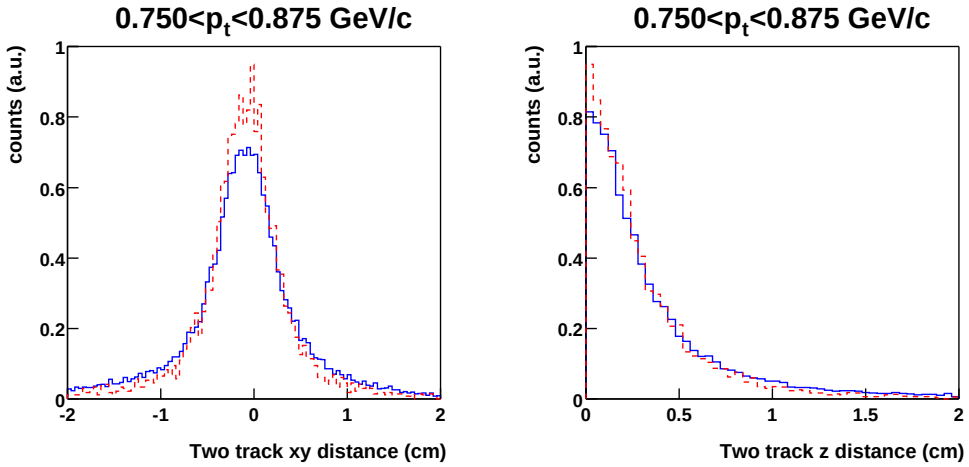

Figure 4.10: Two track distance in the xy-plane (left) and along z (right). The plots compare the distributions of real photon candidates (blue) and simulated photons (red).

slices. The distributions of pair parameters used to find secondary vertices, the two track distance in the xy-plane and along z, are narrower for the simulated photons, as shown in Figure 4.10. Differences in these distributions have a minimal effect on the photon–finding efficiency, since only a small fraction of the photons lie in the regions outside the cuts, 1.5 cm in xy-plane and 1 cm along z. Distributions related to the topology of the conversion, the dip angle difference and electron–positron invariant mass, are also sharper in the simulations, as shown in Figure 4.11. The photon–selection cuts were placed on the tails of these distributions to minimize the effects that arise from the differences.

An estimated systematic uncertainty of 7% was assigned to each p_t bin in the corrected spectrum to cover the uncertainties that arise from differences in these distributions.

4.3 π^0 Embedding Studies

Between seven and twelve simulated π^0s, that decayed into two photons that interacted (see Section 4.1), were embedded into each real event. This corresponds to the addition of less than 48 charged tracks and is less than 2% of the number of reconstructed tracks in the embedded phase space for the highest multiplicity events. As was the case for the embedded single photons, the embedded photons from simulated $\pi^0 \rightarrow \gamma\gamma$ decays were reconstructed with the real event photon–finding algorithm except that the dE/dx requirement was eliminated and the primary vertex of the original event was preserved. The π^0 resolution studies and efficiency calculations used two different methods of π^0 association. For the resolution studies, where comparisons of input and reconstructed parameters were necessary, reconstructed π^0s were directly associated with simulated ones. Reconstructed π^0s were associated with embedded π^0s by finding a reconstructed photon that passed the photon association criteria for each of the two photons in the $\pi^0 \rightarrow \gamma\gamma$ decay. For the efficiency calculation, all reconstructed photons that satisfied the association criteria with at least one simulated photon were retained.

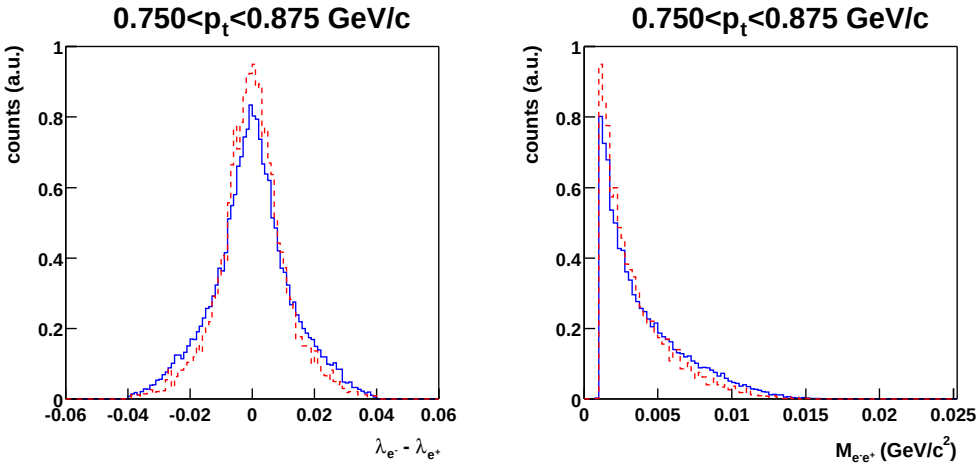

Figure 4.11: Dip angle difference distribution (left) and invariant mass distribution (right). These plots compare the distributions of real photon candidates (blue) and simulated photons (red).

4.3.1 π^0 Kinematic Parameter Resolutions

The π^0 p_t resolution was obtained by fitting a Gaussian function to the distribution of ($p_t{}^{rec}$-$p_t{}^{mc}$)/$p_t{}^{mc}$ in 0.25 GeV/c $p_t{}^{mc}$ slices. The Gaussian widths are shown as a function of p_t and y in Figure 4.12. With a 0.25 T tracking field, the p_t resolution of π^0s for the top 11% most central events is 4% at 2.5 GeV/c. This is better than that of single charged tracks (5%) at the same p_t. Sharing the momentum amongst four tracks enhances the resolution at high p_t, because the single–track resolution deteriorates as a track's sagitta –the longest distance from the line drawn between the endpoints to a point on the curve of the track– becomes comparable to the position resolution of hits in the TPC. The rapidity resolution was estimated by fitting a Gaussian function to the distribution of y^{rec}-y^{mc} in different rapidity slices. The extracted resolution of ∼0.00035 justifies that the resolution is much finer than the y bin width, |y|<1, of the corrected π^0 spectrum.

4.3.2 π^0 Detection Efficiency

The efficiency of detecting $\pi^0 \rightarrow \gamma\gamma$ decays was calculated as a function of p_t for four centrality classes. The calculations were performed on simulated tracks that stemmed from embedded π^0s, as discussed in Section 4.1. All possible pairs of associated photons within each event were constructed and pairs from the same $\pi^0 \rightarrow \gamma\gamma$ decay were not tagged. Two–photon properties, such as invariant mass and p_t, were calculated with the same algorithm that was used on the real data. The reconstructed yields of simulated π^0s in various p_t slices were extracted with the background and fitting procedure that is discussed in Section 3.3. A fit to the invariant mass distribution for one p_t slice is shown in Figure 4.13. The shape of the efficiency was calculated by dividing the reconstructed yields by the input distribution of π^0s. This input distribution was read from the text file that contained the three–vector momentum information of all generated π^0s. The efficiencies for the minimum bias (0–85%), peripheral (34%–85%), mid–central (11%–34%) and central (top 11%) centrality classes are shown as a function of p_t in Figure 4.13.

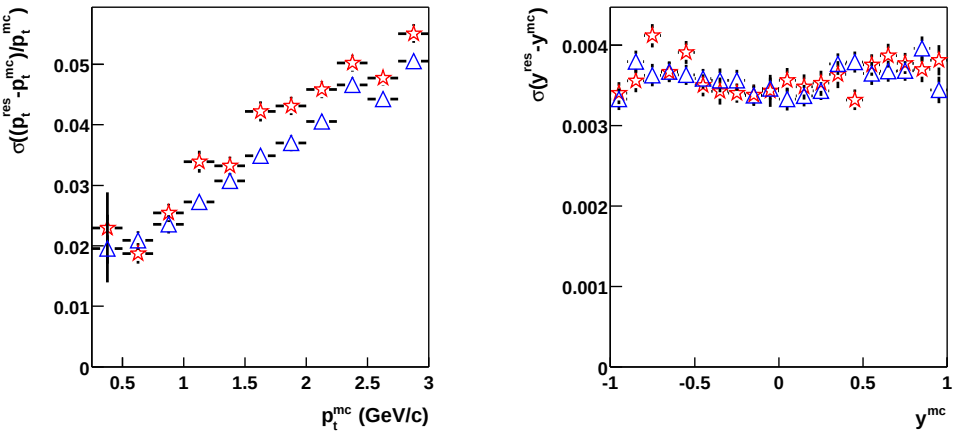

Figure 4.12: p_t (left) and y (right) resolutions of π^0s are shown for both minimum bias events (blue triangles) and events in the top 11% centrality class (red stars).

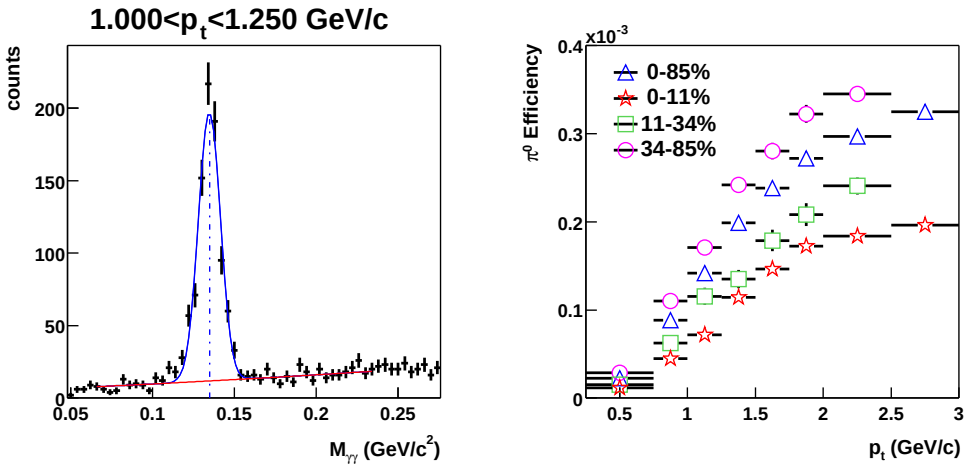

Figure 4.13: Left: Fit to the $\pi^0 \rightarrow \gamma\gamma$ decay invariant mass peak of embedded $\pi^0 \rightarrow \gamma\gamma$ decays. Right: The efficiency calculations for minimum bias 0–85% (blue triangle), peripheral 34%–85% (pink circles), mid–central 34%–11% (green boxes) and central top 11% (red stars) centrality classes. These detection efficiencies include two scale factors. One that corrects for the material map differences, Section 3.3.1. The other factor, 0.912, compensates for tracks lost via the dE/dx cut of -2<$\sigma_{deviant}$<4, note this cut was applied to all four tracks.

Chapter 5

Results

Photon and π^0 per event yields are extracted. The $\pi^0 \rightarrow \gamma\gamma$ decay contributions to the inclusive photon spectra are studied. Comparisons are made between the top 11% most central π^0 spectrum, and published $\pi^{+,0,-}$ and charged hadron spectra.

5.1 Integrated Yields

Integrated yields of photons and π^0s were measured for three centrality classes of events. The yields of photons about mid–rapidity, |y|<0.5, were obtained by fitting the flat dN_γ/dy versus y distributions with a constant, as shown in Figure 5.1. These yields were found to be 525±37, 277±19 and 64±5 per unit of rapidity about mid–rapidity for the 0–11%, 11–34% and 34–85% centrality bins, respectively.

The π^0 yields were obtained by adding the yields in the measured region of p_t to a functional extrapolation in the unmeasured territory. Both Boltzmann and Bose–Einstein functions (Eq. 5.1) were used to interpolate the unmeasured portions of the yields. Fits to the π^0 spectra are shown in Figure 5.2. These two functions treat the system as a thermalized gas. Other functions that incorporate resonances that decay into π^0s and/or radial expansion of the system with additional parameters were not chosen, because the additional parameters tended not to be constrained by the 7 or 8 data points of the spectra.

In both functions, total energy has been replaced by transverse energy, $\sqrt{p_t^2c^2 + m_\pi^2c^4}$, under the assumption that the system is boost invariant near mid–rapidity. This is supported by the flat shape in the particle rapidity distribu-

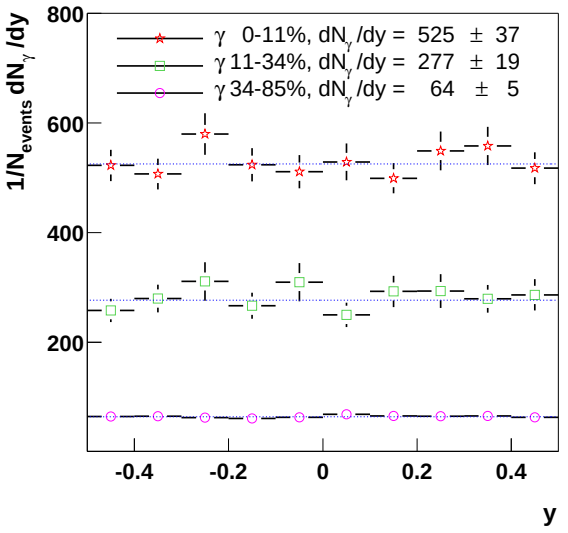

Figure 5.1: Constant fits to the dN/dy of photons for ^{197}Au+^{197}Au collisions at $\sqrt{s_{\rm NN}}$ = 130 GeV. These fits illustrate that dN_γ/dy as a function of y is consistent with a flat line between ±0.5 units of rapidity. Average dN_γ/dy were obtained from the fits and are given in the plot for the 0–11%, 11–34% and 34–85% centrality classes.

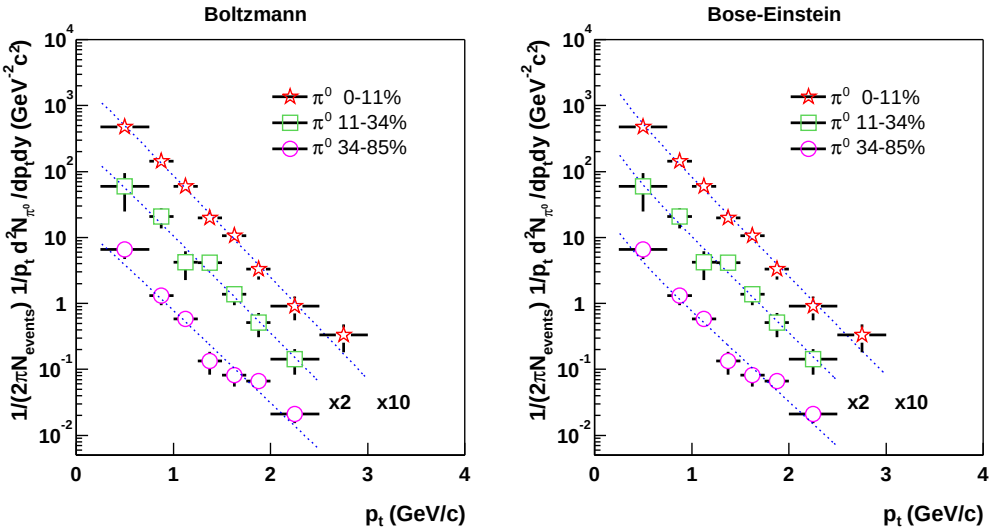

Figure 5.2: Boltzmann (left) and Bose–Einstein (right) fits to the π^0 spectra of three centrality classes. The spectra have been separated by the indicated multiplicative factors.

tions close to mid–rapidity [B$^+$01b]. The local effective temperatures, T_{eff}, for the three centrality classes are given in Table 5.1. The word local emphasizes that the temperatures extracted with these functions are dependent on the p_t interval of the fit. Measurements of the $\pi^{\pm}$ spectra over a wide range of p_t, $0.25<p_t<2$ GeV/c, confirm that the spectral shapes are concave and are not purely exponential [A$^+$01b]. An enhancement at low p_t, $p_t<0.5$ GeV/c, can be explained by the kinematics of 2 and 3 body decays [SKH91]. For p_t between $0.075<p_t<0.725$ GeV/c the $\pi^{\pm}$ spectra have a local Bose–Einstein $T_{eff}\approx 0.205$ GeV which is for the most part independent of centrality [dlBS01]. Whereas, for p_t between $0.25<p_t<3$ GeV/c, the π^0 spectra have higher temperatures near 0.295 GeV. The π^0 temperatures may indicate a decreasing trend, moving towards the $\pi^{\pm}$ temperatures that were measured in a lower p_t interval, with increasing collision centrality. This is consistent with the observation that "with increasing centrality the curvature of the spectra decreases" [A$^+$01b]. This trend is also consistent with results that high p_t π^0s are suppressed in the most central collisions when compared to peripheral collisions [A$^+$01c].

$$1/\left(2\pi N_{events}\right)\ 1/p_t\ d^2N_{\pi^0}/dp_t dy = \frac{n}{b + e^{\sqrt{p_t^2c^2+m_\pi^2c^4}/T_{eff}}}, \tag{5.1}$$

where n is the normalization, T_{eff} is an effective temperature of the system and c is the speed of light. b=0 for the Boltzmann function and b=-1 for the Bose–Einstein function.

The measured and total yields are given in Table 5.2. With the Boltzmann function about 19% of the π^0 yield is in the unmeasured region of p_t, while with the Bose–Einstein function about 28% is unmeasured. If the low p_t $\pi^{\pm}$ temperature of 0.205 GeV is assumed, then the extracted fraction of the yield below p_t=0.25 GeV/c becomes 30% rather than 19% for the Boltzmann function, and 37% rather than 28% for the Bose–Einstein fuction. Asymmetric systematic uncertainties of +11% and +7% were assigned to the total yields to account for the higher local temperatures obtained as

Centrality Bin	p_t (GeV/c)	T_{eff} (Boltzmann) (GeV)	T_{eff} (Bose–Einstein) (GeV)
34 – 85%	0.25 – 2.5	0.308 ± 0.033	0.319 ± 0.035
11 – 34%	0.25 – 2.5	0.293 ± 0.026	0.298 ± 0.027
0 – 11%	0.25 – 3.0	0.281 ± 0.013	0.289 ± 0.014

Table 5.1: Effective temperatures, T_{eff}, for Boltzmann and Bose–Einstein fits to the three different π^0 spectra in the given p_t ranges.

Centrality Bin	p_t (GeV/c)	Measured dN_{π^0}/dy (stat)	Total (Boltzmann) dN_{π^0}/dy (stat) (sys)	Total (Bose–Einstein) dN_{π^0}/dy (stat) (sys)
34 – 85%	0.25 – 2.5	14.1 ± 3.1	16.1 ± 4.1 + 1.8	15.8 ± 3.9 + 1.1
11 – 34%	0.25 – 2.5	72.3 ± 27.7	87.9 ± 34.8 + 9.7	86.4 ± 34.2 + 6.0
0 – 11%	0.25 – 3.0	114.0 ± 16.0	142.7 ± 22.3 + 15.7	138.6 ± 21.5 + 9.7

Table 5.2: Measured and total dN_{π^0}/dy for ^{197}Au+^{197}Au collisions at $\sqrt{s_{NN}}$ = 130 GeV. The total dN_{π^0}/dy is given assuming both Boltzmann and Bose–Einstein functions for the extrapolation. The statistical errors include both the error of the data and of the fit. The additional systematic errors were assigned to account for uncertainties in temperature parameters in regions where the spectra are not fit. Note that additional uncertainties in the normalizations, ±40% (11–34% and 34–85%) and ±49% (top 11%), have not been included.

a consequence of the fit regions, Boltzmann and Bose–Einstein respectively.

5.2 Background in the Photon Spectra

Electromagnetic decays of neutral mesons are the dominant mechanisms that produce photons in heavy ion collisions. Among these, the π^0 and η are the two dominant contributors to the photon spectrum. Signals from photons emitted during the early stages of the collisions are hidden beneath these backgrounds. The $\pi^0 \rightarrow \gamma\gamma$ mechanism alone composes more than 65% of the photon yield. The measured π^0 spectra were used to remove this contribution. Simulated π^0 spectra were generated based on the Boltzmann and Bose–Einstein fits and corresponding per event yields. The π^0 yields were assumed to be flat in rapidity and symmetric in azimuth. The input rapidity distribution of π^0s was limited to $|y|<2$. This rapidity window produces more than 99% of the photons from $\pi^0 \rightarrow \gamma\gamma$ decays within $|y|<0.5$. Comparisons between the π^0 distributions created in the simulation and measured spectra are shown in Figure 5.3.

These π^0 distributions were passed through a Monte Carlo decay simulator that calculated the $\pi^0 \rightarrow \gamma\gamma$ decay kinematics and the boost between the center of mass and lab frame. The output was the three–vector momentum information of the decay photons in the lab frame. Photon p_t spectra were extracted from this information. These spectra are directly compared to the measured photon spectra in Figure 5.4. The similar shapes and amplitudes of the measured and simulated spectra confirm that the $\pi^0 \rightarrow \gamma\gamma$ decay is the dominant production mechanism of photons in heavy ion collisions.

The fraction of photons from $\pi^0 \rightarrow \gamma\gamma$ decays in the inclusive photon spectra were obtained as a function of p_t. They were found by dividing the simulated photon spectra from $\pi^0 \rightarrow \gamma\gamma$ decays by

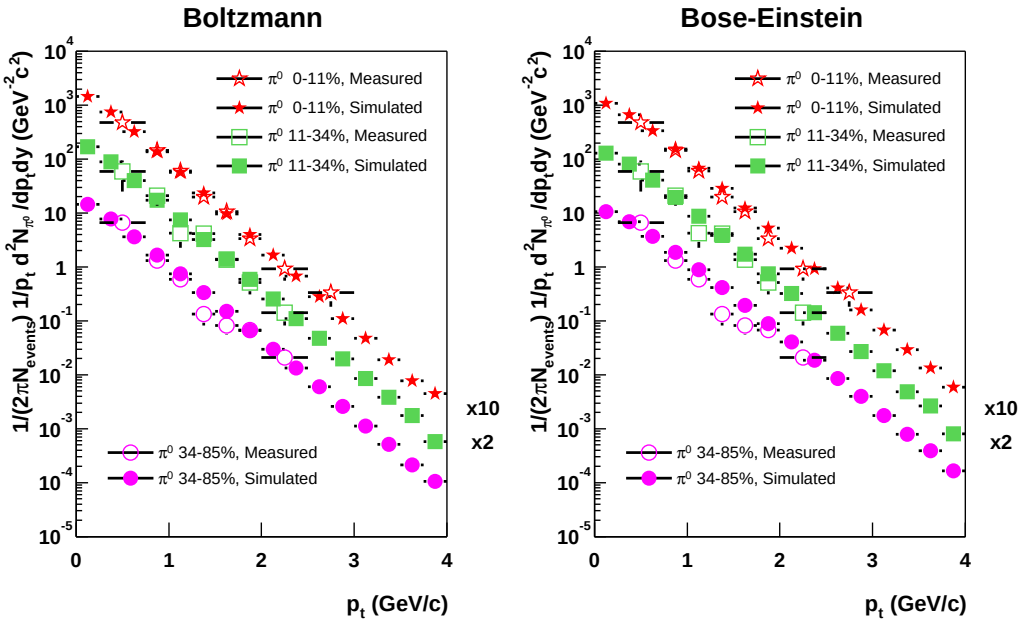

Figure 5.3: Comparisons between the measured π^0 spectra and spectra created with the Boltzmann and Bose–Einstein functions for the p_t dependence of the π^0s.

the measured photon spectra, as shown in Figure 5.5. These ratios are shown for p_t>0.45 GeV/c, where the photon contribution is determined from π^0s in and above the measured p_t interval. The kinematics of the $\pi^0 \rightarrow \gamma\gamma$ decay set an upper limit on the p_t of the daughter photons. A π^0 of p_t<0.435 GeV/c will only produce photons with p_t below 0.45 GeV/c. Thus, the unmeasured portions of the π^0 spectra below p_t=0.25 GeV/c do not contribute to the photon spectra above where the ratios start at 0.45 GeV/c. The shapes of these ratios are independent of uncertainties in the normalizations of the π^0 spectra. The ratio for the top 11% most central data is consistent with a flat line between 0.75 GeV/c<p_t<1.65 GeV/c and above p_t=1.65 GeV/c it starts to decrease. A 20% reduction in the relative contribution from $\pi^0 \rightarrow \gamma\gamma$ decays is observed from p_t=1.65 GeV/c to p_t=2.4 GeV/c. A similar trend was observed by the WA98 collaboration in ^{208}Pb+^{208}Pb collisions at $\sqrt{s_{\rm NN}}$ = 17.2 GeV [A$^+$00]. In the WA98 analysis the background from η decays was also removed. This is estimated to account for less than 15% of the background relative to the π^0 contribution in all p_t bins of this analysis, below 2.4 GeV/c. The mid–central data, 11–34% centrality class, also have a similar feature; though it is absent in the peripheral data (34–85% centrality).

5.3 Comparisons to Published Data

The top 11% central π^0 spectrum presented in this thesis, a STAR measurement, has been compared to published data also from ^{197}Au+^{197}Au collisions at $\sqrt{s_{\rm NN}}$ = 130 GeV. Among these published data are two 10% most central π^0 spectra, the top 5% most central π^- and π^+ spectra, and the top 5% most central negative and positive hadron spectra. The lack of statistics in the number of measured π^0s limited the ability for the measurements to be made in centrality bins that

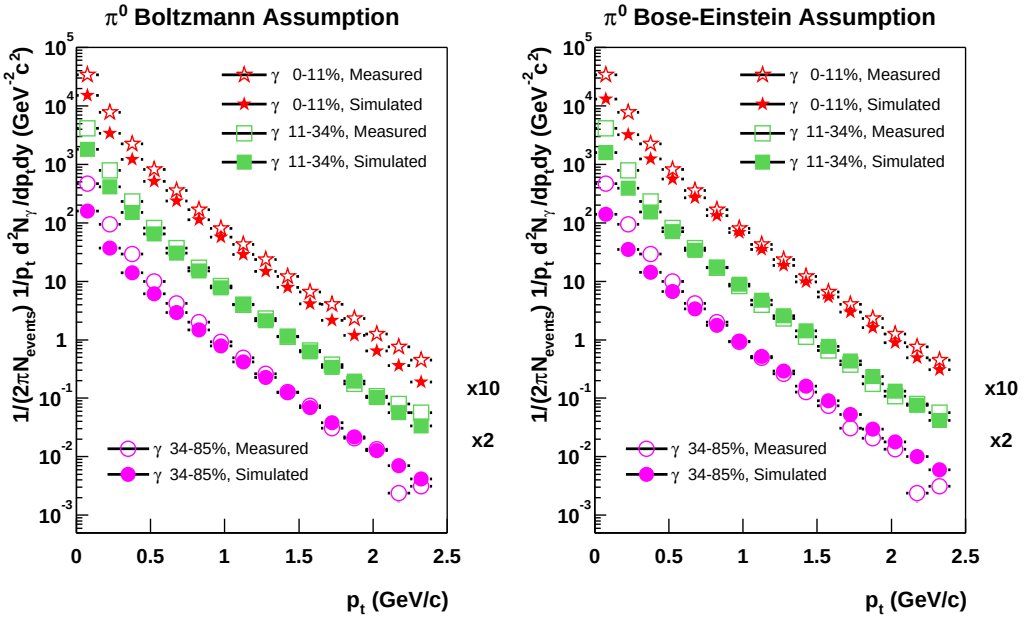

Figure 5.4: Comparisons between the measured photon spectra and spectra generated from simulations of $\pi^0 \rightarrow \gamma\gamma$ decays assuming Boltzmann and Bose–Einstein functions for the p_t dependence of the π^0s.

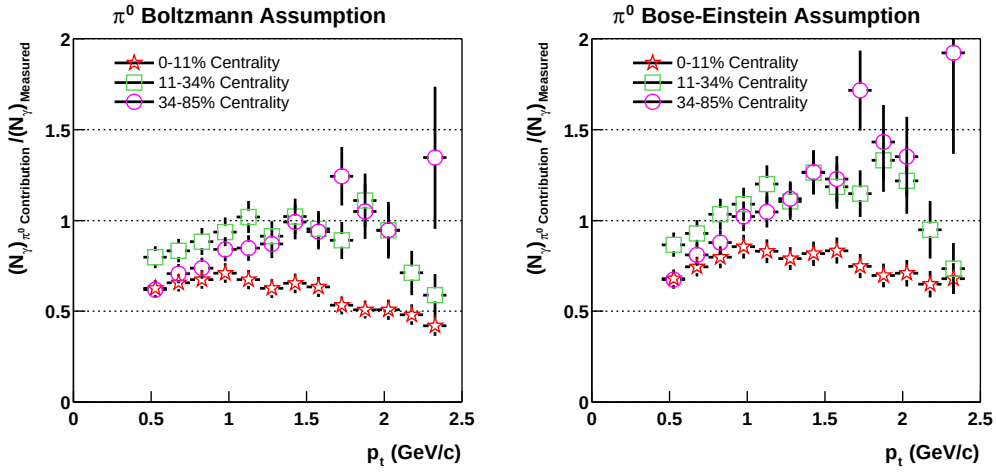

Figure 5.5: Ratios of the simulated photon spectra generated from simulations of $\pi^0 \rightarrow \gamma\gamma$ decays assuming Boltzmann and Bose–Einstein functions for the p_t dependence of the π^0s, to the measured photon spectra. Note that uncertainties in the normalizations of the π^0 spectra, $\pm 40\%$ (11–34% and 34–85%) and $\pm 49\%$ (top 11%), have not been included and do not effect the shapes of the ratios.

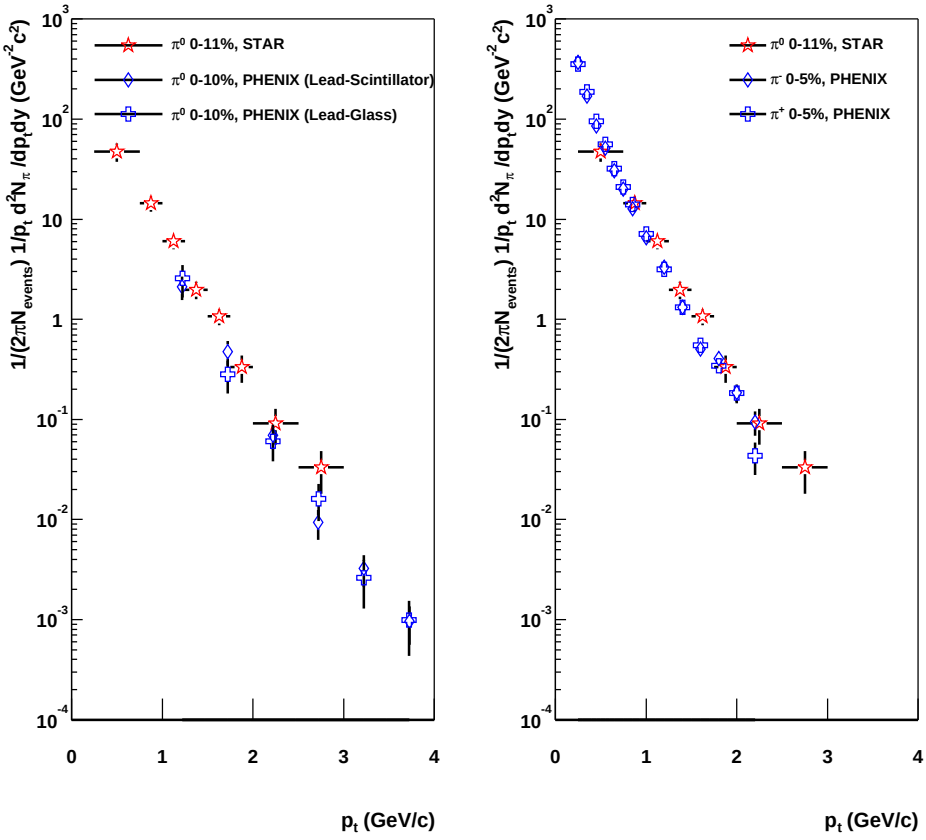

Figure 5.6: Comparisons between the STAR π^0 measurement, and PHENIX π^0 [A$^+$01c] and $\pi^\pm$ [A$^+$01b] data for ^{197}Au+^{197}Au collisions at $\sqrt{s_{\rm NN}} = 130$ GeV.

correspond more closely to those of the other data. PHENIX published two π^0 spectra for the top 10% most central ^{197}Au+^{197}Au collisions at $\sqrt{s_{\rm NN}} = 130$ GeV [A$^+$01c]. One measurement was made with Lead–Scintillator calorimeters and the other with Lead–Glass calorimeters. The p_t coverage of these data extends from 1 GeV/c to 4 GeV/c and overlaps the most central STAR measurement between 1 GeV/c and 3 GeV/c. The general shape of the three spectra are consistent, as shown in Figure 5.6. The PHENIX data is systematically 78% lower than the STAR data, though the data are consistent within 1σ of the systematic errors assigned to the normalizations. Note, part of the offset can be due to the two independent measures of the centrality classes.

Comparisons at lower p_t were made to π^-, π^+, negative hadrons and positive hadrons. These data are presently only available for the top 5% most central collisions. Ignoring slightly differing centrality definitions, the PHENIX π^- and π^+ data compare well with the top 11% STAR π^0 spectrum. These data show a rapid rise in the vicinity of the lowest STAR π^0 data point, $0.25<p_t<0.75$ GeV/c. This same feature is also apparent in a comparison to the inclusive hadron data from STAR, Figure

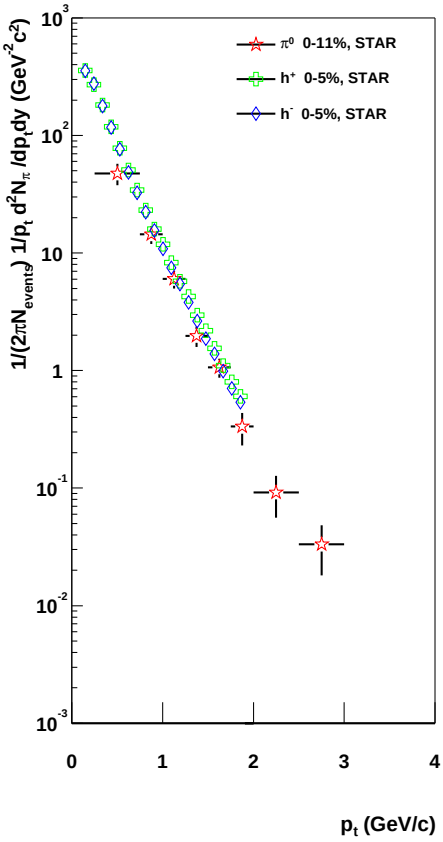

Figure 5.7: Comparisons between the STAR π^0 measurement and STAR inclusive hadron spectra [A$^+$01e] for ^{197}Au+^{197}Au collisions at $\sqrt{s_{\rm NN}} = 130$ GeV.

5.7. The comparisons to the hadron spectra are valid at low p_t were the relative abundance of pions dominates the hadron spectra. Overall the charged hadron spectrum is composed of $\sim$80% πs.

Chapter 6

Conclusion

Photon and π^0 production have been studied for ^{197}Au+^{197}Au collisions at $\sqrt{s_{\rm NN}} = 130$ GeV by reconstructing pair conversions from tracks measured with the STAR TPC. This method of detecting photons in heavy ion collisions has been developed and established. The centrality dependence of the photon and π^0 production about mid–rapidity was presented as a function of p_t. The rapidity dependence of photon production was also presented. Despite the fundamental challenge posed by the design of STAR, since it was optimized "to minimize multiple scattering and photon conversion" [Col92], these results represent the first measurement of photon production and the first step towards addressing direct photons in heavy ion collisions at RHIC energies.

The technique of measuring photons via pair conversions, $\gamma Z \rightarrow e^- e^+ Z$, has been developed based on both the analysis of real data and detailed detector simulations. Corrections for detector acceptance, tracking inefficiency, photon finding inefficiencies and the photon conversion probability were calculated with detailed detector simulations and applied to the data. Real data were used to adjust the conversion probability of the simulations and correct for inconsistencies between the physical and simulated material maps. However, these inconsistencies are responsible for the largest uncertainties in the π^0 measurements and jeopardized the precision in the normalizations. For photons, the dominant background from the $\pi^0 \rightarrow \gamma\gamma$ decay has been estimated with the measured π^0 distributions for three centrality classes. Comparisons between the estimated backgrounds and inclusive spectra have been discussed.

For the most central and mid–central centrality classes, these measured distributions indicate that the $\pi^0 \rightarrow \gamma\gamma$ decay becomes less of a contribution to photon production as p_t increases. It is unlikely that a decrease of the observed magnitude, 20% from p_t=1.65 GeV/c to 2.4 GeV/c in central collisions, can be solely attributed to other π^0 decay channels and other particle decays. This growing enhancement may signify a substantial radiation of photons during the earlier stages of mid to central heavy ion collisions, since the distribution from peripheral collisions does not exhibit this feature.

Boltzmann and Bose–Einstein functions were used to extract temperature parameters for the π^0 distributions. These temperature parameters are near 0.295 GeV and differ from those observed for $\pi^{\pm}$ distributions at lower p_t. Thus, the data indicate a deviation from a purely exponentially falling shape. It has been proposed that such a feature may arise from 2 and 3 body resonance decays [SKH91].

It has been shown, that this method of detecting photons can be used to extend and provide complementary physics results to those obtained through more conventional approaches. With this established method, a larger pool of events from the year 2001 run and a higher conversion probability near z=0 with the installation of the silicon for the SVT; STAR has the capability of

firmly addressing direct photon production over a wide range of p_t. The next step is to measure the η cross section and remove this background source from the inclusive photon spectrum. The increased magnetic field, of more recently taken data, will improve the already excellent energy resolution and will aid this effort. Furthermore, the dominating material dependent uncertainties in the absolute normalizations of the π^0 spectra will decrease with the larger sample of events that has a narrower vertex spread in z.

Appendix A

Kinematic Variables

Symbols	Name (units)	Definition
Track		
$(x_0, y_0, z_0)^\dagger$	coordinate of first point (cm)	
$\psi^\dagger$	xy-plane direction at first point	
$\lambda^\dagger$	dip angle (radians)	$\arctan(\mathrm{p}_z/\mathrm{p}_t)$
$x_c, y_c^\dagger$	coordinate of helix center (cm)	
$\mathrm{r}^\dagger$	helix radius (cm)	
	rigidity	$\frac{.3rB}{\cos(\lambda)}$, units r(m) and B(T)
q^*	charge (relative to the charge of one e^+)	
${\mathrm{p}_t}^*$	transverse momentum, p_{xy}, (GeV/c)	$.3rqB$, units r(m) and B(T)
p_z	momentum along the beam axis (GeV/c)	$\mathrm{p}_t \cdot \tan(\lambda)$
p	total momentum (GeV/c)	$\sqrt{p_t^2 + p_z^2}$
E	Energy assuming particle of mass(m) (GeV)	$\sqrt{p^2 + m^2}$
y	rapidity	$\frac{1}{2}\ln\left(\frac{E+p_z}{E-p_z}\right)$
η	pseudorapidity	$-\ln\tan\left(\frac{\pi-\lambda}{2}\right)$
Photon		
$\mathrm{E}^\ddagger$	energy of the photon (GeV)	$E_{e^-} + E_{e^+}$
$\lambda^\ddagger$	dip angle (radians)	$(\lambda_e^- + \lambda_e^+)/2$
$\phi^\ddagger$	angular direction in xy-plane (radians)	$\left(\vec{x}_c^{\,e^-} - \vec{x}_c^{\,e^+}\right) \times \vec{B}$
p	momentum (GeV/c)	E/c
p_t	transverse momentum (GeV/c)	$\mathrm{p} \cdot \cos(\lambda)$
p_x	momentum along the the x-axis (GeV/c)	$\mathrm{p}_t \cdot \cos(\phi)$
p_y	momentum along the the y-axis (GeV/c)	$\mathrm{p}_t \cdot \sin(\phi)$
p_z	momentum along the beam axis (GeV/c)	$\mathrm{p} \cdot \sin(\lambda)$
y	photon rapidity	$\frac{1}{2}\ln\left(\frac{p+p_z}{p-p_z}\right)$
ν_E	fraction of energy carried by the positron	E_{e^+}/E_γ
Two Photon		
M_{in}	two photon invariant mass (GeV/c^2)	$\sqrt{2\left\|p_1\right\|\left\|p_2\right\|\left(1 - \hat{p_1} \cdot \hat{p_2}\right)}$
p_t	transverse momentum (GeV/c)	$\sqrt{\left(p_{x,1} + p_{x,2}\right)^2 + \left(p_{y,1} + p_{y,2}\right)^2}$
p_z	momentum along the beam axis (GeV/c)	$p_{z,1} + p_{z,2}$
p	total momentum (GeV/c)	$\sqrt{p_t^2 + p_z^2}$
E	total energy (GeV)	$\sqrt{p^2c^2 + M_{in}^2c^4}$
y	rapidity	$\frac{1}{2}\ln\left(\frac{E+p_z}{E-p_z}\right)$

Table A.1: Descriptions of commonly used kinematic variables. The symbols † and ‡ denote variables that are obtained directly from the helix parameters of tracks and the photon finding algorithm, respectively. The $*$ symbol is used to denote that in the tracking algorithm, the magnitude of a particle's charge is assumed to be the charge of a positron. Later, a more accurate assumption of a particle's charge can be made through the combination of dE/dx and rigidity.

Appendix B

Photon Data Points

p_t (GeV/c)	$1/(2\pi N_{events})\ 1/p_t\ d^2N_\gamma/dp_t dy$ (mean)	(stat)	(sys)	$1/(2\pi N_{events})\ 1/p_t\ d^2N_\gamma/dp_t dy$ (>40 cm) (mean)	(stat)	(sys)
Peripheral (34%–85%)						
0.00 – 0.15	470.0	± 39.4	± 32.9	581.0	± 52.0	± 40.7
0.15 – 0.30	94.70	± 1.86	± 6.63	101.53	± 2.77	± 7.11
0.30 – 0.45	29.50	± 0.46	± 2.06	29.20	± 0.72	± 2.04
0.45 – 0.60	9.906	± 0.158	± 0.693	9.997	± 0.272	± 0.700
0.60 – 0.75	4.155	± 0.074	± 0.291	4.247	± 0.138	± 0.297
0.75 – 0.90	2.002	± 0.053	± 0.140	1.766	± 0.085	± 0.124
0.90 – 1.05	0.9248	± 0.0285	± 0.0647	0.8258	± 0.0489	± 0.0578
1.05 – 1.20	0.4906	± 0.0180	± 0.0343	0.4624	± 0.0328	± 0.0324
1.20 – 1.35	0.2594	± 0.0113	± 0.0182	0.2296	± 0.0203	± 0.0161
1.35 – 1.50	0.1267	± 0.0071	± 0.0089	0.0960	± 0.0119	± 0.0067
1.50 – 1.65	0.07392	± 0.00506	± 0.00517	0.06503	± 0.00941	± 0.00455
1.65 – 1.80	0.03071	± 0.00307	± 0.00215	0.01815	± 0.00472	± 0.00127
1.80 – 1.95	0.02059	± 0.00239	± 0.00144			
1.95 – 2.10	0.01333	± 0.00184	± 0.00093			
2.10 – 2.25	0.002398	± 0.000744	± 0.000168			
2.25 – 2.40	0.003116	± 0.000847	± 0.000218			

Table B.1: Corrected photon yields about mid-rapidity, |y|<0.5, for the 34–85% centrality class of ^{197}Au+^{197}Au collisions at $\sqrt{s_{\rm NN}}$ = 130 GeV. The spectrum is discussed in Section 3.2.6 and plotted in Figure 3.12. Note that the uncorrected raw counts of the r_{xy}>40 cm data points are a subset of the uncorrected raw counts of r_{xy}>10 cm. The data sets are correlated and the errors can not be used in comparisons between them.

y	$1/N_{events}\ dN_\gamma/dy$ (mean)	(stat)	$1/N_{events}\ dN_\gamma/dy$ (>40 cm) (mean)	(stat)
Peripheral (34%–85%)				
-0.5 – -0.4	64.68	± 2.93	64.62	± 3.92
-0.4 – -0.3	65.55	± 3.16	67.33	± 4.35
-0.3 – -0.2	62.69	± 2.82	68.23	± 4.30
-0.2 – -0.1	61.52	± 2.81	67.16	± 4.34
-0.1 – 0.0	63.25	± 2.99	68.90	± 4.67
0.0 – 0.1	68.92	± 3.70	74.88	± 5.71
0.1 – 0.2	66.05	± 3.33	74.09	± 5.47
0.2 – 0.3	65.36	± 3.24	74.31	± 5.53
0.3 – 0.4	65.74	± 3.19	71.20	± 4.80
0.4 – 0.5	63.28	± 2.98	68.84	± 4.58

Table B.2: Corrected dN_γ/dy for the 34–85% centrality class of ^{197}Au+^{197}Au collisions at $\sqrt{s_{\rm NN}}$ = 130 GeV. The spectrum is discussed in Section 3.2.6 and plotted in Figure 3.12. An overall 7% systematic error is assigned the normalization. Note that the uncorrected raw counts of the r_{xy}>40 cm data points are a subset of the uncorrected raw counts of r_{xy}>10 cm. The data sets are correlated and the errors can not be used in comparisons between them.

p_t (GeV/c)	$1/(2\pi N_{events})$ $1/p_t\ d^2N_\gamma/dp_t dy$ (mean)	(stat)	(sys)	$1/(2\pi N_{events})$ $1/p_t\ d^2N_\gamma/dp_t dy$ (>40 cm) (mean)	(stat)	(sys)
Mid-central (11%–34%)						
0.00 – 0.15	2066.	± 369.	± 145.	2444.	± 452.	± 171.
0.15 – 0.30	397.0	± 14.2	± 27.8	398.6	± 19.5	± 27.9
0.30 – 0.45	115.8	± 2.9	± 8.1	115.5	± 4.5	± 8.1
0.45 – 0.60	40.54	± 0.94	± 2.84	41.67	± 1.61	± 2.92
0.60 – 0.75	18.34	± 0.43	± 1.28	18.61	± 0.75	± 1.30
0.75 – 0.90	8.458	± 0.317	± 0.592	8.664	± 0.575	± 0.606
0.90 – 1.05	4.114	± 0.155	± 0.288	3.999	± 0.278	± 0.280
1.05 – 1.20	1.988	± 0.079	± 0.139	2.127	± 0.161	± 0.149
1.20 – 1.35	1.157	± 0.052	± 0.081	0.925	± 0.082	± 0.065
1.35 – 1.50	0.5608	± 0.0296	± 0.0393	0.4772	± 0.0501	± 0.0334
1.50 – 1.65	0.3274	± 0.0196	± 0.0229	0.2883	± 0.0376	± 0.0202
1.65 – 1.80	0.1880	± 0.0135	± 0.0132	0.1669	± 0.0268	± 0.0117
1.80 – 1.95	0.08776	± 0.00816	± 0.00614			
1.95 – 2.10	0.05434	± 0.00614	± 0.00380			
2.10 – 2.25	0.03975	± 0.00512	± 0.00278			
2.25 – 2.40	0.02848	± 0.00425	± 0.00199			

Table B.3: Corrected photon yields about mid-rapidity, |y|<0.5, for the 11–34% centrality class of ^{197}Au+^{197}Au collisions at $\sqrt{s_{\rm NN}}$ = 130 GeV. The spectrum is discussed in Section 3.2.6 and plotted in Figure 3.12. Note that the uncorrected raw counts of the r_{xy}>40 cm data points are a subset of the uncorrected raw counts of r_{xy}>10 cm. The data sets are correlated and the errors can not be used in comparisons between them.

y	$1/N_{events}\ dN_\gamma/dy$ (mean)	(stat)	$1/N_{events}\ dN_\gamma/dy$ (>40 cm) (mean)	(stat)
Mid-central (11%–34%)				
-0.5 – -0.4	258.3	± 21.1	311.2	± 41.1
-0.4 – -0.3	280.0	± 25.2	297.5	± 36.9
-0.3 – -0.2	311.0	± 35.0	347.0	± 59.8
-0.2 – -0.1	266.8	± 23.7	280.6	± 35.6
-0.1 – 0.0	309.8	± 34.9	299.4	± 39.9
0.0 – 0.1	250.0	± 22.2	254.5	± 28.8
0.1 – 0.2	292.8	± 28.7	315.6	± 45.2
0.2 – 0.3	293.6	± 30.8	262.2	± 30.4
0.3 – 0.4	279.3	± 25.1	292.9	± 36.1
0.4 – 0.5	286.5	± 28.6	286.7	± 34.7

Table B.4: Corrected dN_γ/dy for the 11–34% centrality class of ^{197}Au+^{197}Au collisions at $\sqrt{s_{\rm NN}}$ = 130 GeV. The spectrum is discussed in Section 3.2.6 and plotted in Figure 3.12. An overall 7% systematic error is assigned the normalization. Note that the uncorrected raw counts of the r_{xy}>40 cm data points are a subset of the uncorrected raw counts of r_{xy}>10 cm. The data sets are correlated and the errors can not be used in comparisons between them.

p_t (GeV/c)	$1/(2\pi N_{events})\ 1/p_t\ d^2N_\gamma/dp_t dy$ (mean)	(stat)	(sys)	$1/(2\pi N_{events})\ 1/p_t\ d^2N_\gamma/dp_t dy$ (>40 cm) (mean)	(stat)	(sys)
Top 11% most centeral						
0.00 – 0.15	3383.	± 398.	± 237.	4442.	± 545.	± 311.
0.15 – 0.30	772.5	± 17.4	± 54.1	725.2	± 22.0	± 50.8
0.30 – 0.45	225.5	± 3.4	± 15.8	214.3	± 4.9	± 15.0
0.45 – 0.60	82.19	± 1.10	± 5.75	78.25	± 1.69	± 5.48
0.60 – 0.75	35.83	± 0.45	± 2.51	31.51	± 0.67	± 2.21
0.75 – 0.90	16.70	± 0.35	± 1.17	14.53	± 0.50	± 1.02
0.90 – 1.05	7.956	± 0.165	± 0.557	7.391	± 0.265	± 0.517
1.05 – 1.20	4.254	± 0.091	± 0.298	3.640	± 0.139	± 0.255
1.20 – 1.35	2.357	± 0.053	± 0.165	2.078	± 0.084	± 0.145
1.35 – 1.50	1.204	± 0.029	± 0.084	1.124	± 0.051	± 0.079
1.50 – 1.65	0.6515	± 0.0171	± 0.0456	0.6131	± 0.0311	± 0.0429
1.65 – 1.80	0.4015	± 0.0117	± 0.0281	0.3314	± 0.0195	± 0.0232
1.80 – 1.95	0.2314	± 0.0078	± 0.0162			
1.95 – 2.10	0.1262	± 0.0051	± 0.0088			
2.10 – 2.25	0.07515	± 0.00371	± 0.00526			
2.25 – 2.40	0.04526	± 0.00270	± 0.00317			

Table B.5: Corrected photon yields about mid-rapidity, |y|<0.5, for the top 11% most central events of ^{197}Au+^{197}Au collisions at $\sqrt{s_{\rm NN}} = 130$ GeV. The spectrum is discussed in Section 3.2.6 and plotted in Figure 3.12. Note that the uncorrected raw counts of the r_{xy}>40 cm data points are a subset of the uncorrected raw counts of r_{xy}>10 cm. The data sets are correlated and the errors can not be used in comparisons between them.

y	$1/N_{events}\ dN_\gamma/dy$ (mean)	(stat)	$1/N_{events}\ dN_\gamma/dy$ (>40 cm) (mean)	(stat)
Top 11% most centeral				
-0.5 – -0.4	522.6	± 28.6	522.4	± 37.7
-0.4 – -0.3	506.8	± 28.2	469.8	± 31.1
-0.3 – -0.2	579.6	± 37.8	601.9	± 55.4
-0.2 – -0.1	523.6	± 30.2	544.3	± 44.8
-0.1 – 0.0	511.0	± 30.4	485.7	± 37.9
0.0 – 0.1	528.9	± 33.7	566.6	± 55.8
0.1 – 0.2	499.2	± 27.5	493.2	± 34.8
0.2 – 0.3	549.0	± 35.2	551.9	± 46.6
0.3 – 0.4	557.9	± 34.9	663.7	± 65.4
0.4 – 0.5	517.5	± 29.1	515.2	± 36.6

Table B.6: Corrected dN_γ/dy for the top 11% most central events of ^{197}Au+^{197}Au collisions at $\sqrt{s_{\rm NN}} = 130$ GeV. The spectrum is discussed in Section 3.2.6 and plotted in Figure 3.12. An overall 7% systematic error is assigned the normalization. Note that the uncorrected raw counts of the r_{xy}>40 cm data points are a subset of the uncorrected raw counts of r_{xy}>10 cm. The data sets are correlated and the errors can not be used in comparisons between them.

p_t (GeV/c)	$1/(2\pi N_{events})$ $1/p_t\ d^2N_\gamma/dp_t dy$ (mean)	(stat)	(sys)	$1/(2\pi N_{events})$ $1/p_t\ d^2N_\gamma/dp_t dy$ (>40 cm) (mean)	(stat)	(sys)
Minimum bias (0%–85%)						
0.00 – 0.15	935.8	± 68.7	± 65.5	1165.6	± 90.8	± 81.6
0.15 – 0.30	211.8	± 3.4	± 14.8	215.2	± 4.8	± 15.1
0.30 – 0.45	67.54	± 0.81	± 4.73	66.51	± 1.24	± 4.66
0.45 – 0.60	24.28	± 0.28	± 1.70	23.88	± 0.46	± 1.67
0.60 – 0.75	10.70	± 0.13	± 0.75	10.43	± 0.22	± 0.73
0.75 – 0.90	5.191	± 0.096	± 0.363	4.620	± 0.149	± 0.323
0.90 – 1.05	2.543	± 0.050	± 0.178	2.312	± 0.084	± 0.162
1.05 – 1.20	1.281	± 0.028	± 0.090	1.226	± 0.051	± 0.086
1.20 – 1.35	0.6682	± 0.0167	± 0.0468	0.5646	± 0.0283	± 0.0395
1.35 – 1.50	0.3525	± 0.0105	± 0.0247	0.2961	± 0.0180	± 0.0207
1.50 – 1.65	0.2036	± 0.0072	± 0.0143	0.1836	± 0.0136	± 0.0128
1.65 – 1.80	0.1114	± 0.0049	± 0.0078	0.1265	± 0.0106	± 0.0089
1.80 – 1.95	0.05961	± 0.00330	± 0.00417			
1.95 – 2.10	0.03960	± 0.00257	± 0.00277			
2.10 – 2.25	0.02215	± 0.00184	± 0.00155			
2.25 – 2.40	0.01347	± 0.00142	± 0.00094			

Table B.7: Corrected photon yields about mid-rapidity, |y|<0.5, for minimum bias events of ^{197}Au+^{197}Au collisions at $\sqrt{s_{\rm NN}}$ = 130 GeV. The spectrum is discussed in Section 3.2.6 and plotted in Figure 3.12. Note that the uncorrected raw counts of the r_{xy}>40 cm data points are a subset of the uncorrected raw counts of r_{xy}>10 cm. The data sets are correlated and the errors can not be used in comparisons between them.

y	$1/N_{events}\ dN_\gamma/dy$ (mean)	(stat)	$1/N_{events}\ dN_\gamma/dy$ (>40 cm) (mean)	(stat)
Minimum bias (0%–85%)				
-0.5 – -0.4	146.8	± 5.2	151.8	± 7.4
-0.4 – -0.3	151.2	± 5.7	152.0	± 7.7
-0.3 – -0.2	146.5	± 5.4	156.4	± 8.2
-0.2 – -0.1	143.4	± 5.3	153.4	± 8.2
-0.1 – 0.0	149.6	± 6.0	158.2	± 8.9
0.0 – 0.1	152.2	± 6.5	156.6	± 9.1
0.1 – 0.2	150.6	± 6.1	163.1	± 9.7
0.2 – 0.3	148.8	± 6.0	155.3	± 8.8
0.3 – 0.4	147.9	± 5.5	152.7	± 7.9
0.4 – 0.5	148.7	± 5.8	158.0	± 8.4

Table B.8: Corrected dN_γ/dy for minimum bias events of ^{197}Au+^{197}Au collisions at $\sqrt{s_{\rm NN}}$ = 130 GeV. The spectrum is discussed in Section 3.2.6 and plotted in Figure 3.12. An overall 7% systematic error is assigned the normalization. Note that the uncorrected raw counts of the r_{xy}>40 cm data points are a subset of the uncorrected raw counts of r_{xy}>10 cm. The data sets are correlated and the errors can not be used in comparisons between them.

Appendix C

π^0 Data Points and Fits

p_t (GeV/c)	$1/(2\pi N_{events})\ 1/p_t\ d^2N_{\pi^0}/dp_t dy$ (mean)	(stat)
	Peripheral (34%-85%)	
0.25 – 0.75	6.64	± 1.93
0.75 – 1.00	1.31	± 0.38
1.00 – 1.25	0.585	± 0.133
1.25 – 1.50	0.134	± 0.051
1.50 – 1.75	0.0813	± 0.0260
1.75 – 2.00	0.0669	± 0.0165
2.00 – 2.50	0.0210	± 0.0057
	Mid-central (11%-34%)	
0.25 – 0.75	29.8	± 17.3
0.75 – 1.00	10.4	± 3.5
1.00 – 1.25	2.11	± 0.98
1.25 – 1.50	2.07	± 0.52
1.50 – 1.75	0.689	± 0.217
1.75 – 2.00	0.257	± 0.103
2.00 – 2.50	0.0713	± 0.0299
	Top 11% most central	
0.25 – 0.75	47.5	± 9.9
0.75 – 1.00	14.5	± 2.55
1.00 – 1.25	6.02	± 1.02
1.25 – 1.50	1.98	± 0.39
1.50 – 1.75	1.07	± 0.20
1.75 – 2.00	0.334	± 0.103
2.00 – 2.50	0.0917	± 0.0358
2.50 – 3.00	0.0332	± 0.0151
	Minimum bias (0-85%)	
0.25 – 0.75	11.1	± 3.2
0.75 – 1.00	4.46	± 0.83
1.00 – 1.25	1.65	± 0.32
1.25 – 1.50	0.792	± 0.142
1.50 – 1.75	0.247	± 0.073
1.75 – 2.00	0.150	± 0.040
2.00 – 2.50	0.0469	± 0.0138
2.50 – 3.00	0.0129	± 0.0053

Table C.1: Corrected yields of π^0s about mid-rapidity (|y|<1) for ^{197}Au+^{197}Au collisions at $\sqrt{s_{\rm NN}}$ = 130 GeV. Data points in the various central bins have a common uncertainty in the normalization of 40%. The top 11% most central data points have an additional uncertainty on the normalization of 19% with respect to the other centrality bins, or a total uncertainty of 49%.

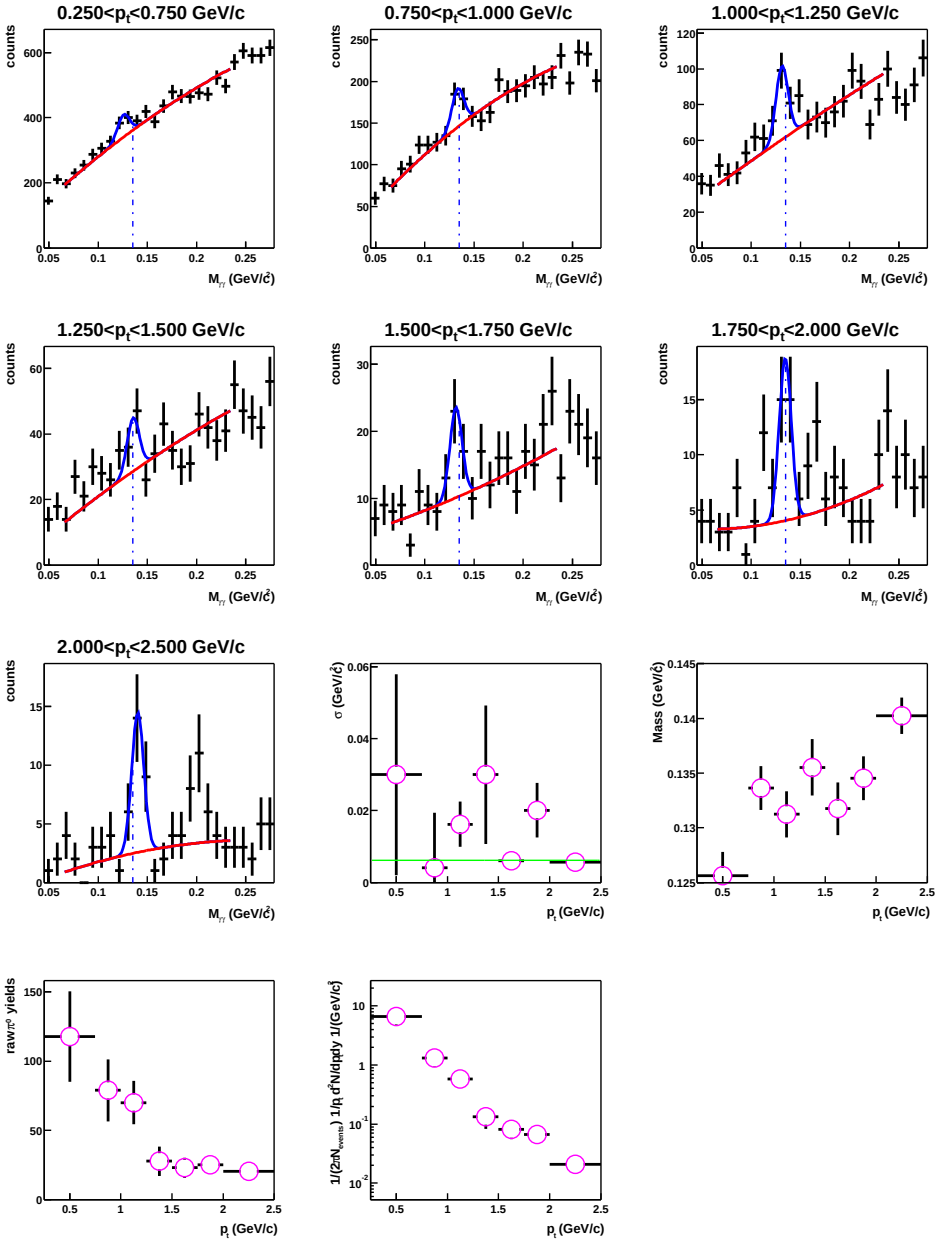

Figure C.1: Gaussian plus background function (Eq. 3.4) fits to the enhancement at the π^0 mass in the two photon invariant mass distributions for the peripheral (34%-85%) centrality bin. The fit parameters are plotted in the lower plots. The statistically significant peaks near 0.2 GeV/c^2 in the invariant mass distribution for the higher p$_t$ bins, especially 2.0<p$_t$<2.5 GeV/c, is not understood at this time.

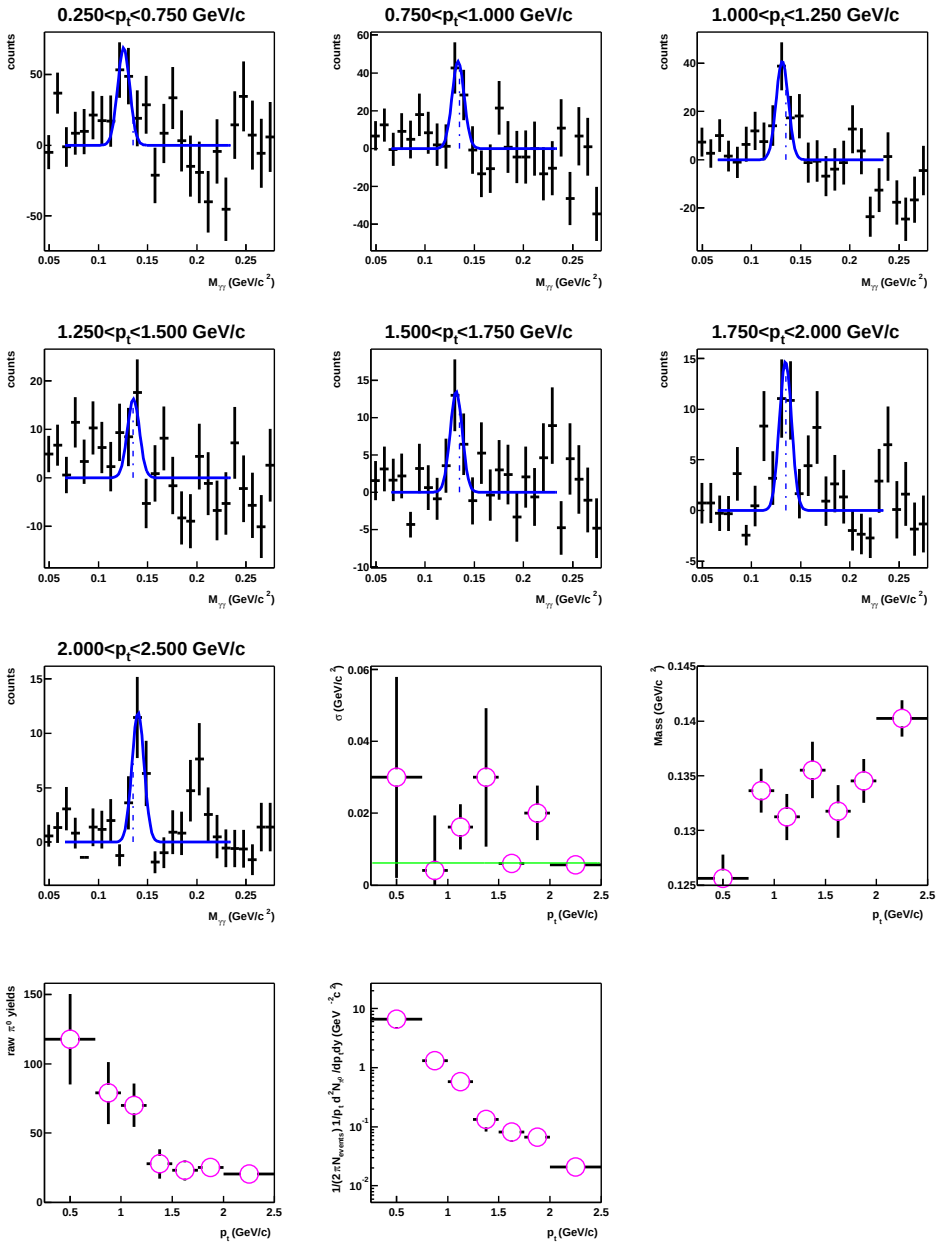

Figure C.2: Gaussian fits to the enhancement at the π^0 mass in the two photon invariant mass distributions after the second order polynomial background function has been subtracted off for the peripheral (34%-85%) centrality bin. The fit parameters are plotted in the lower plots. The statistically significant peaks near 0.2 GeV/c^2 in the invariant mass distribution for the higher p_t bins, especially 2.0<p_t<2.5 GeV/c, is not understood at this time.

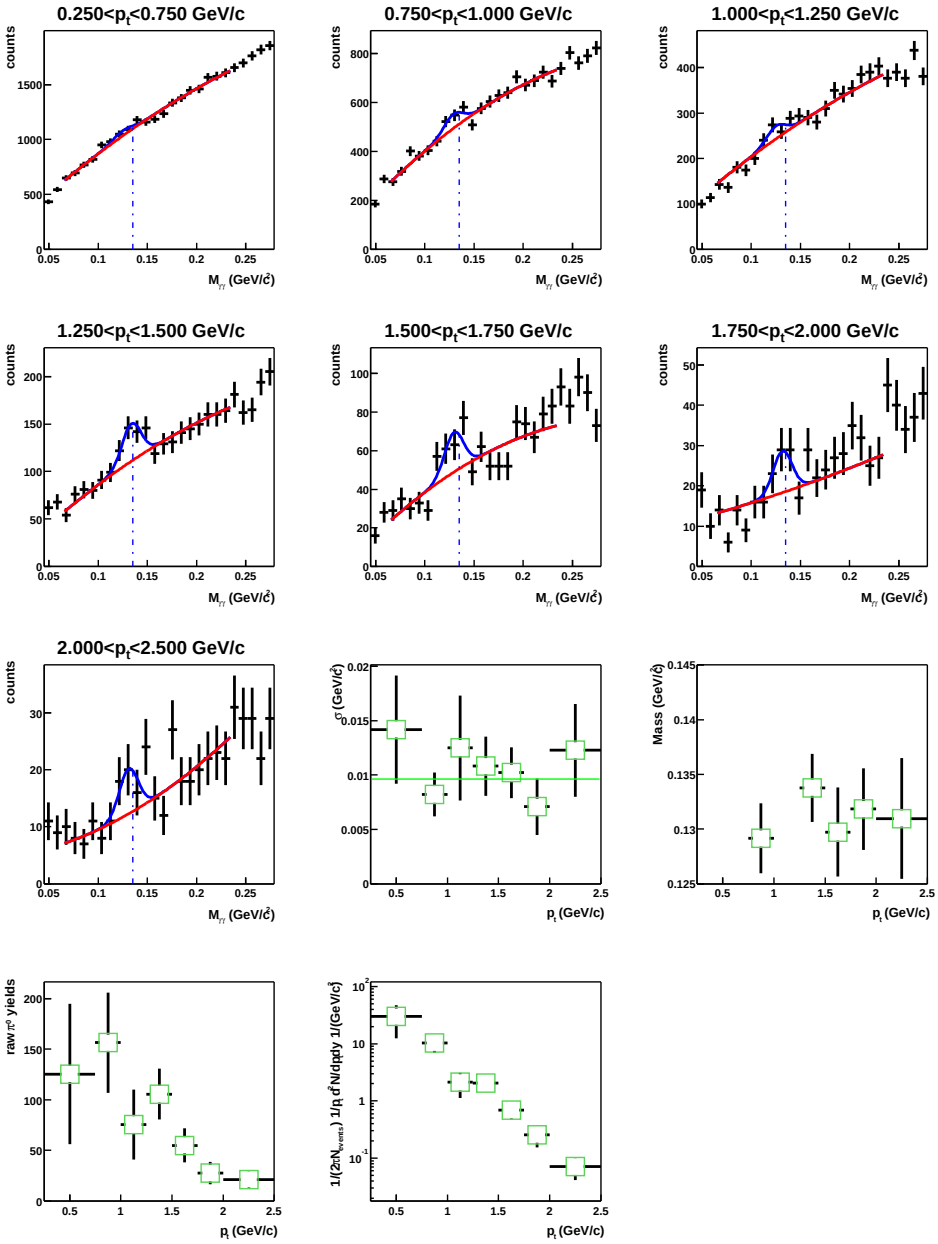

Figure C.3: Gaussian plus background function (Eq. 3.4) fits to the enhancement at the π^0 mass in the two photon invariant mass distributions for the mid-central (11%-34%) centrality bin. The fit parameters are plotted in the lower plots.

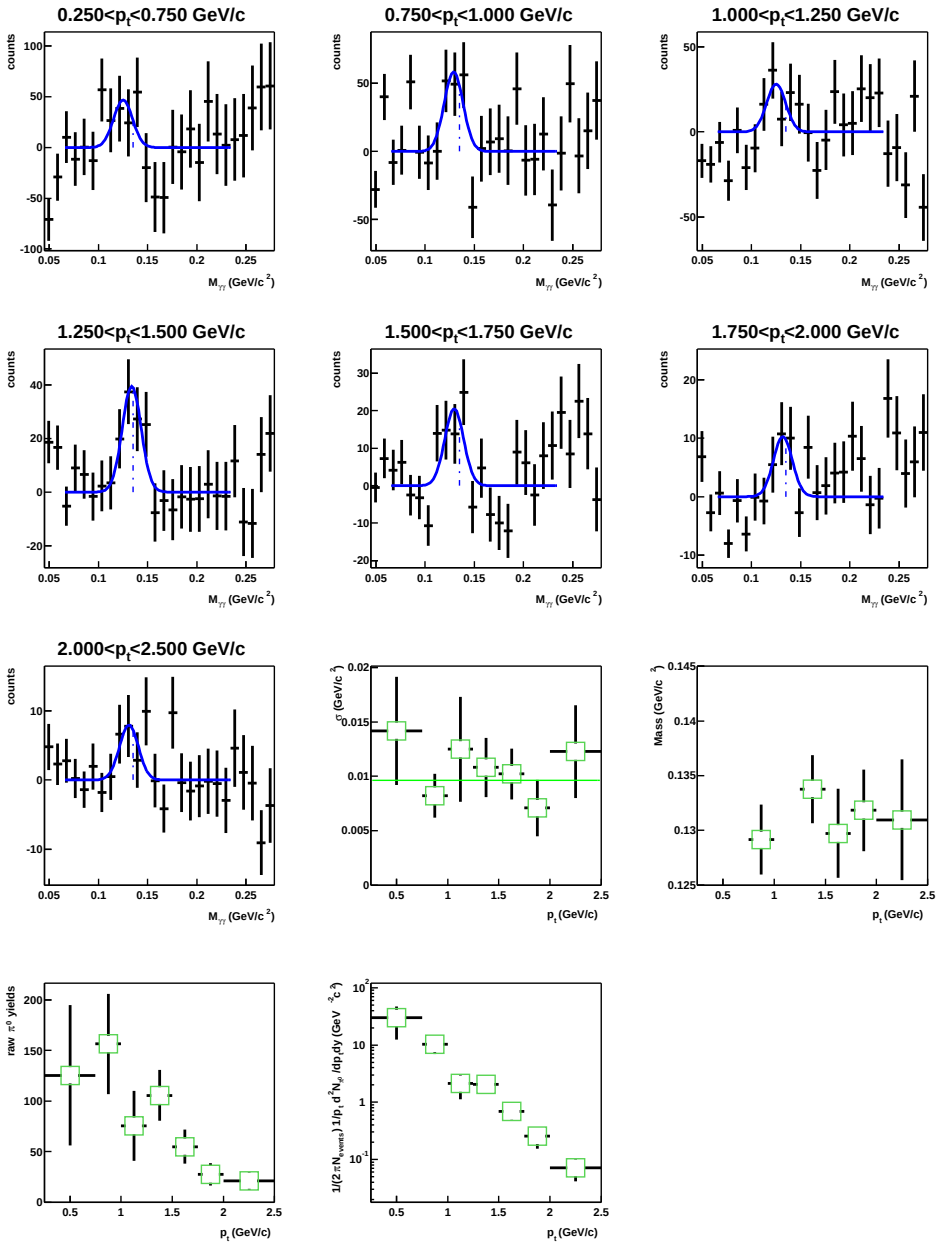

Figure C.4: Gaussian fits to the enhancement at the π^0 mass in the two photon invariant mass distributions after the second order polynomial background function has been subtracted off for the mid-central (11%-34%) centrality bin. The fit parameters are plotted in the lower plots.

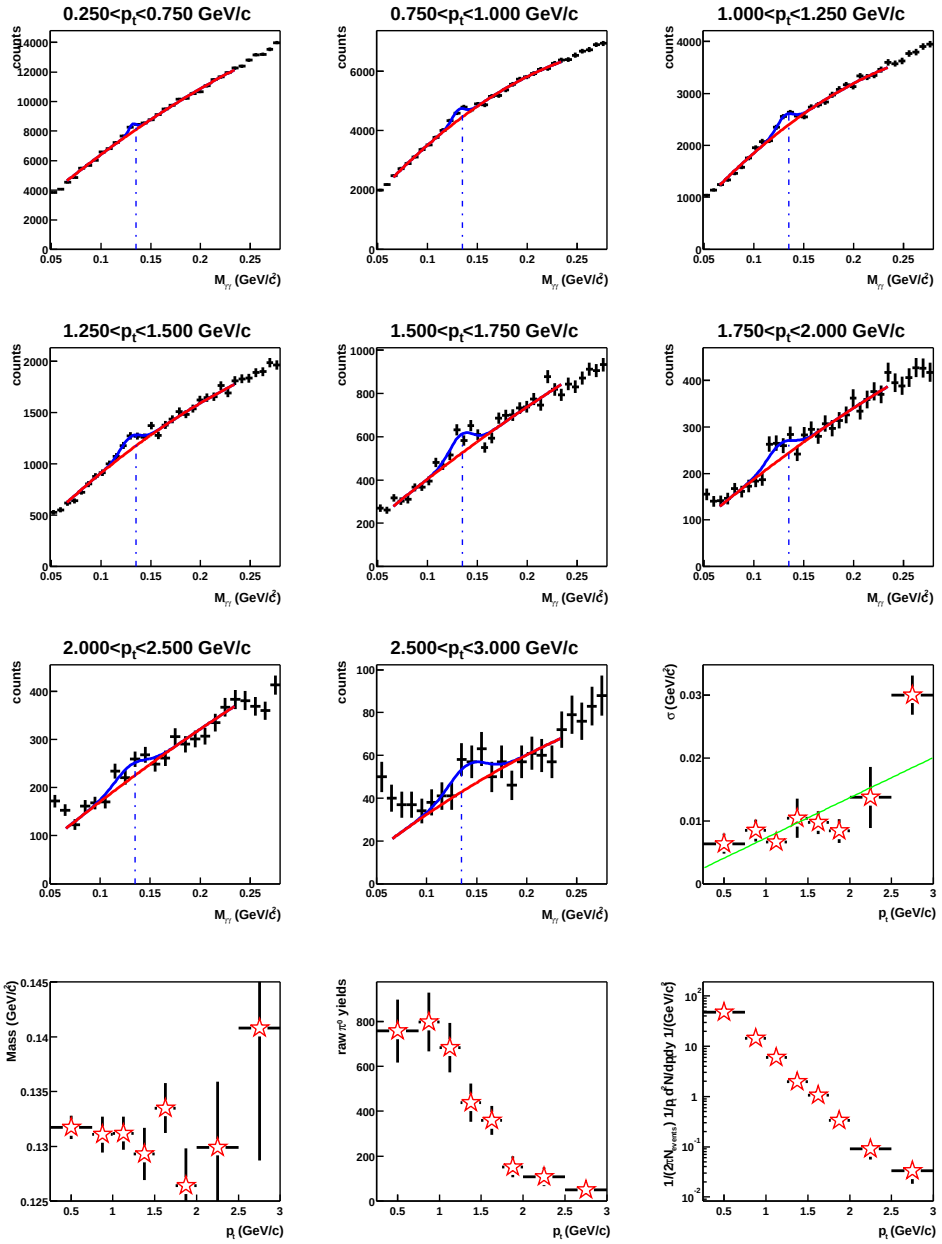

Figure C.5: Gaussian plus background function (Eq. 3.4) fits to the enhancement at the π^0 mass in the two photon invariant mass distributions for the top 11% centrality bin. The fit parameters are plotted in the lower plots.

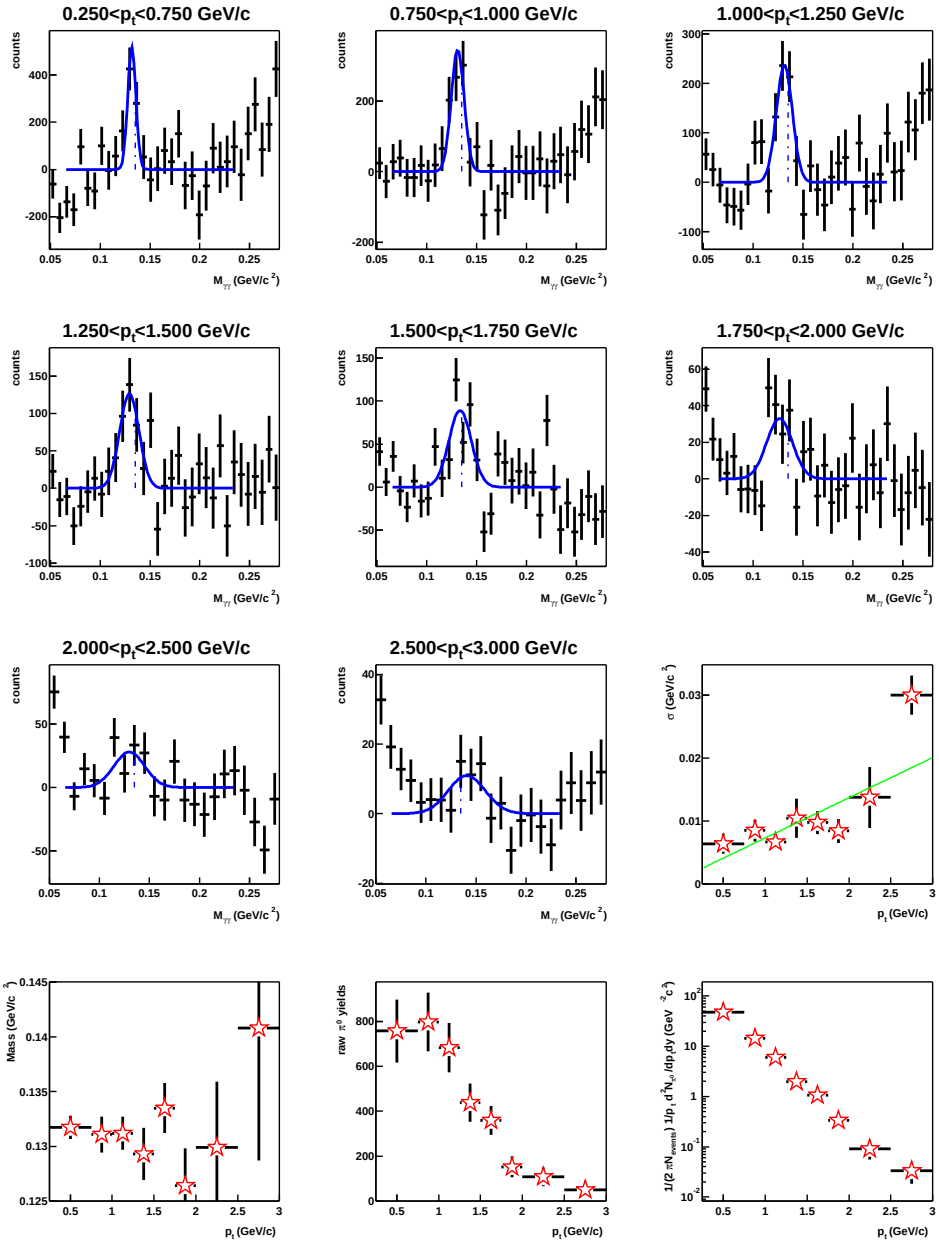

Figure C.6: Gaussian fits to the enhancement at the π^0 mass in the two photon invariant mass distributions after the second order polynomial background function has been subtracted off for the top 11% centrality bin. The fit parameters are plotted in the lower plots.

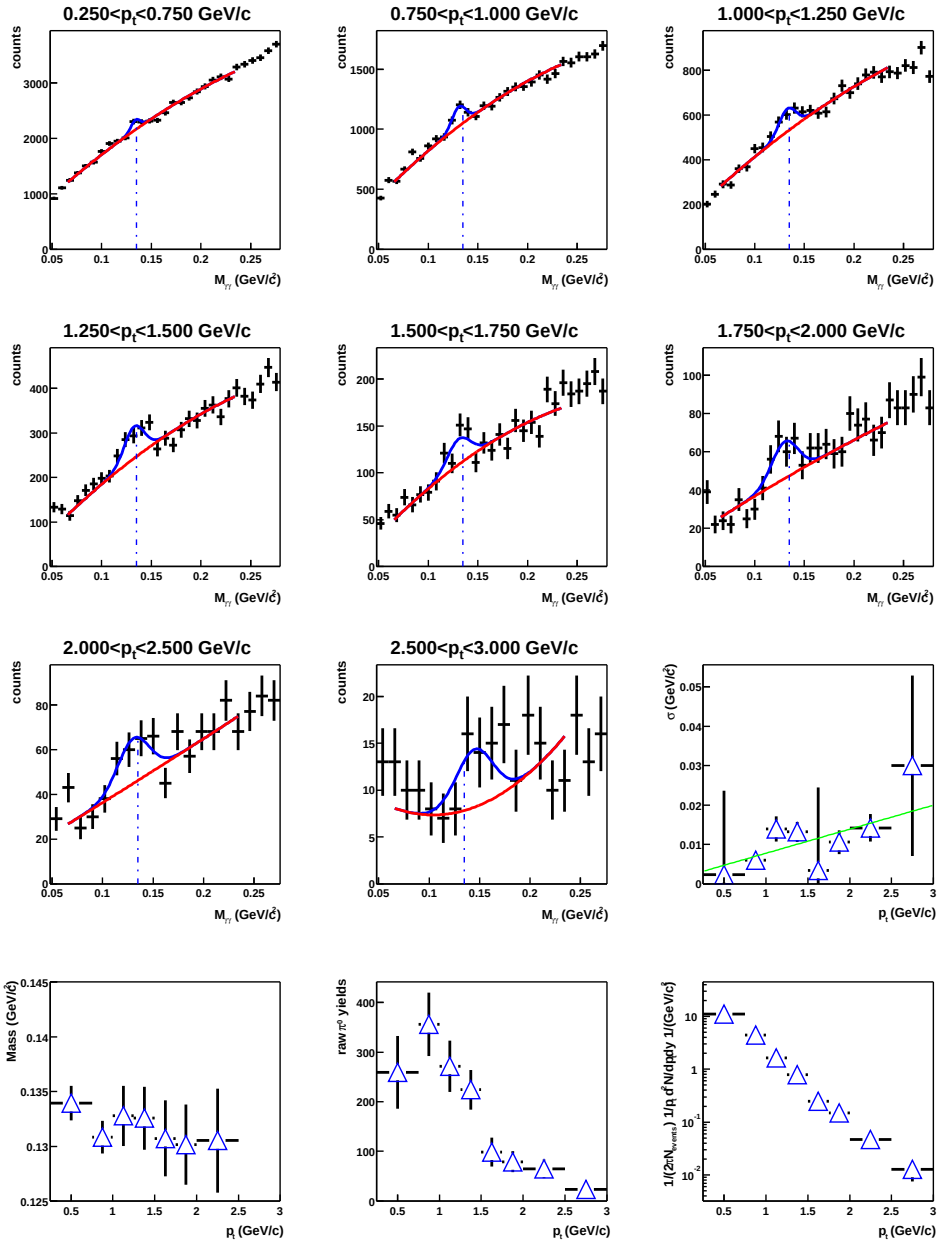

Figure C.7: Gaussian plus background function (Eq. 3.4) fits to the enhancement at the π^0 mass in the two photon invariant mass distributions for the minimum bias (0%-85%) centrality bin. The fit parameters are plotted in the lower plots.

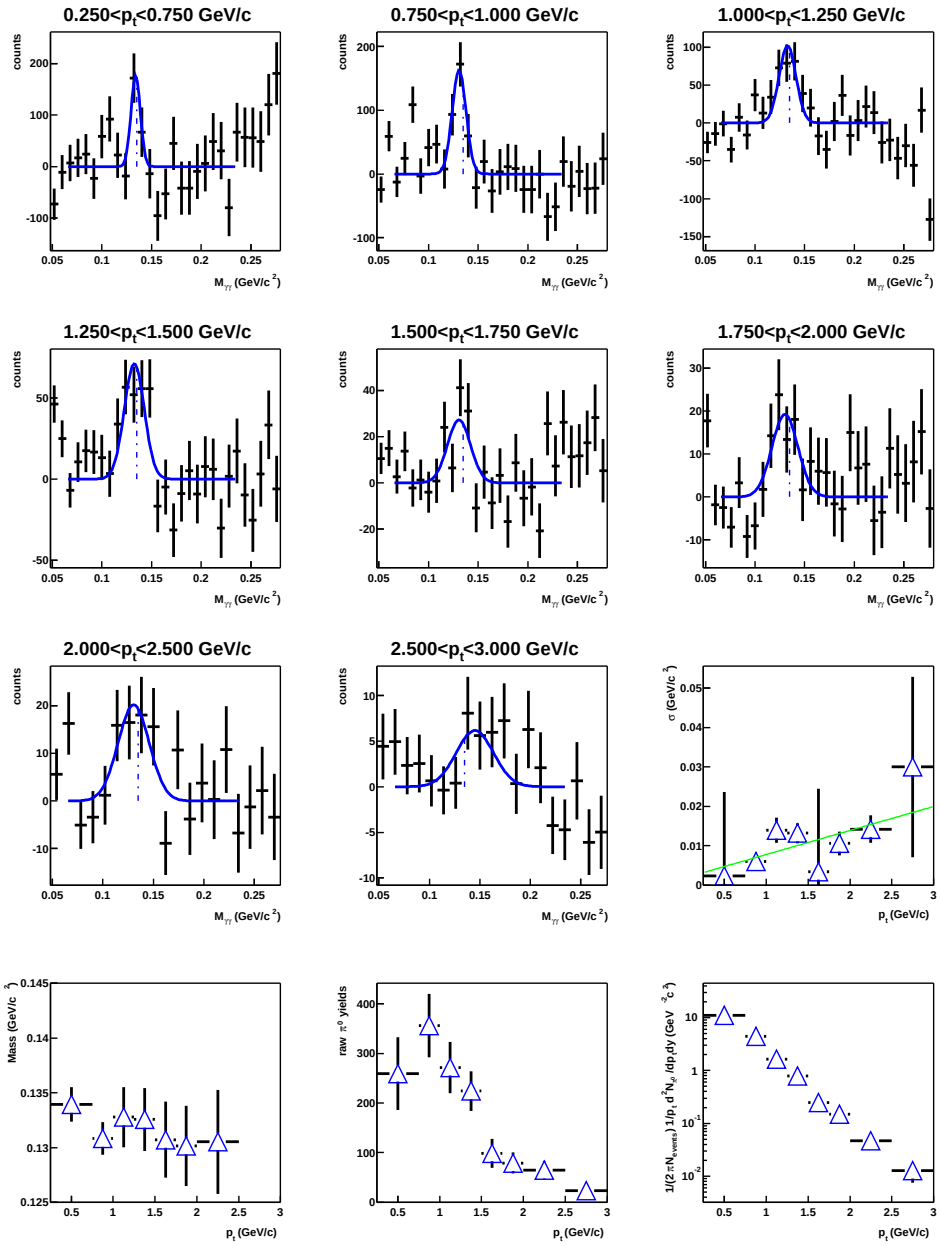

Figure C.8: Gaussian fits to the enhancement at the π^0 mass in the two photon invariant mass distributions after the second order polynomial background function has been subtracted off for the minimum bias (0%-85%) centrality bin. The fit parameters are plotted in the lower plots.

Bibliography

[A$^+$] M. Anderson et al. The STAR Time Projection Chamber: A Unique Tool for Studying High Multiplicity Events at RHIC. *to be published in Nuclear Instruments and Methods A*. URL: http://www.star.bnl.gov/ jhthomas/NimWeb/tpc/tpc_nim.ps.

[A$^+$00] M.M. Aggarwal et al. *Phys. Rev. Lett.*, 85:3595–3599, 2000.

[A$^+$01a] K.H. Ackermann et al. *Phys. Rev. Lett.*, 86:402, 2001.

[A$^+$01b] K. Adcox et al. *Phys. Rev. Lett.*, 86:3500, 2001.

[A$^+$01c] K. Adcox et al. *Phys. Rev. Lett.*, 88:022301, 2001.

[A$^+$01d] C. Adler et al. *Phys. Rev. Lett.*, 86:4778, 2001.

[A$^+$01e] C. Adler et al. *Phys. Rev. Lett.*, 87:112303, 2001.

[A$^+$01f] M.M. Aggarwal et al. *nucl-ex/0006007, submitted to Phys. Rev. C*, 2001.

[AGZ98] P. Aurenche, F. Gelis, and H. Zaraket. *Phys. Rev. D*, 58:085003, 1998.

[B$^+$01a] B.B. Back et al. *Phys. Rev. Lett.*, 87:102301, 2001.

[B$^+$01b] B.B. Back et al. *Phys. Rev. Lett.*, 87:102303, 2001.

[Col92] The STAR Collaboration. Conceptual Design Report for the Solenoidal Tracker At RHIC. Technical report, 1992. LBL PUB-5347.

[dlBS01] M. Calderón de la Barca Sánchez. Charged Hadron Spectra in Au+Au Collisions at $\sqrt{s_{\rm NN}}$ = 130 GeV, Ph.D. thesis, Yale University. 2001.

[gea93] Geant, Detector Description and Simulation Tool. Technical report, 1993. CERN Program Library Long Writeup W5013.

[Gro00] Particle Data Group. *Eur. Phys. J.*, C15:1, 2000.

[HS99] E. Hjort and A. Saulys. Mechanical Drawings. Technical report, 1999. URL: http://www.star.bnl.gov/STAR/html/tpc_l/tpc.html.

[I$^+$01] I.G.Bearden et al. *Phys. Rev. Lett.*, 87:112305, 2001.

[Kar02] F. Karsch. *Nuc. Phys. A*, 698:199c, 2002.

[KLS91] J. Kapusta, P. Lichard, and D. Seibert. *Phys. Rev. D*, 44:2775, 1991.

[KW99] J.I. Kapusta and S.M.H. Wong. Probing the Space-Time Evolution of Heavy Ion Collisions with Bremsstrahlung. *hep-ph/9909573, Proceedings of the XXIX ISMD'99(World Scientific) p.346*, 1999.

[MS94] Jeffery T. Mitchell and Iwona M. Sakrejda. Tracking for the STAR TPC: Documentation and User's Guide. Technical report, Lawrence Berkeley National Laboratory, 1994. STAR Note: SN0190.

[NU02] J.L. Nagle and T. Ullrich. *nucl-ex/0203007*, 1, 2002.

[Per86] D.H. Perkins. Introduction to High Energy Physics. Addison Wesley, Massachusetts, USA, Third edition, 1986.

[Pro94] RHIC Project. RHIC Design Manual. Technical report, Brookhaven National Laboratory, 1994. URL: http://www.agsrhichome.bnl.gov/NT-share/rhicdm/.

[PT02] T. Peitzmann and M.H. Thoma. *Phys. Rept.*, 364:175, 2002.

[SG98] D.K. Srivastava and K. Gieger. *Phys. Rev. C*, 58:1734, 1998.

[Shu78] E.V. Shuryak. *Sov. J Nucl. Phys.*, 28(3):408, 1978.

[SKH91] J. Sollfrank, P. Koch, and U. Heinz. *Z. Phys. C*, 52:593, 1991.

[Sri99] D.K. Srivastava. *Eur. Phys. J. C*, 10:487, 1999.

[VW97] W. Vogelsang and M.R. Whalley. *J. Phys. G: Nucl. Part. Phys.*, 23:A1, 1997.

[XSB92] L. Xiong, E. Shuryak, and G.E. Brown. *Phys. Rev. D*, 46:3798, 1992.